



APPLICATION OF THE PHOTOACOUSTIC AND PHOTOTHERMAL EFFECTS TO COMBUSTION DIAGNOSTICS

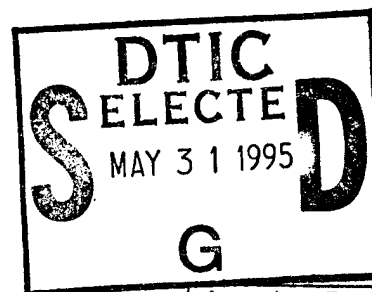
R. GUPTA AND G. J. SALAMO
UNIVERSITY OF ARKANSAS
FAYETTEVILLE, AR 72701

OCTOBER 1986

FINAL REPORT FOR JUNE 1980 TO JUNE 1986

APPROVED FOR PUBLIC RELEASE; DISTRIBUTION IS UNLIMITED

Aero Propulsion and Power Directorate
Wright Laboratory
Air Force System Command
Wright-Patterson Air Force Base, Ohio 45433-6563



Accession For	
NTIS	CRA&I <input checked="" type="checkbox"/>
DTIC	TAB <input checked="" type="checkbox"/>
Unannounced	<input type="checkbox"/>
Justification _____	
By _____	
Distribution /	
Availability Codes	
Dist	Avail and/or Special
A-1	

19950530 040

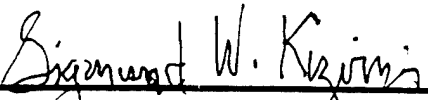
THIS DOCUMENT CONTAINS UNCLASSIFIED INFORMATION

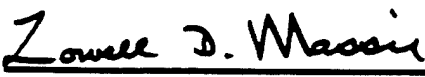
NOTICE

WHEN GOVERNMENT DRAWINGS, SPECIFICATIONS, OR OTHER DATA ARE USED FOR ANY PURPOSE OTHER THAN IN CONNECTION WITH A DEFINITELY GOVERNMENT-RELATED PROCUREMENT, THE UNITED STATES GOVERNMENT INCURS NO RESPONSIBILITY OR ANY OBLIGATION WHATSOEVER. THE FACT THAT THE GOVERNMENT MAY HAVE FORMULATED OR IN ANY WAY SUPPLIED THE SAID DRAWINGS, SPECIFICATIONS, OR OTHER DATA, IS NOT TO BE REGARDED BY IMPLICATION, OR OTHERWISE IN ANY MANNER CONSTRUED, AS LICENSING THE HOLDER, OR ANY OTHER PERSON OR CORPORATION; OR AS CONVEYING ANY RIGHTS OR PERMISSION TO MANUFACTURE, USE, OR SELL ANY PATENTED INVENTION THAT MAY IN ANY WAY BE RELATED THERETO.


THIS REPORT HAS BEEN REVIEWED BY THE OFFICE OF PUBLIC AFFAIRS (ASD/PA) AND IS RELEASABLE TO THE NATIONAL TECHNICAL INFORMATION SERVICE (NTIS). AT NTIS IT WILL BE AVAILABLE TO THE GENERAL PUBLIC INCLUDING FOREIGN NATIONS.

THIS TECHNICAL REPORT HAS BEEN REVIEWED AND IS APPROVED FOR PUBLICATION.


SIGMUND W. KIZIRNIS
Power Components Branch
Aerospace Power Division
Aero Propulsion Directorate


LOWELL D. MASSIE
Chief, Power Component Branch
Aerospace Power Division
Aero Propulsion and Power Directorate

FOR THE COMMANDER


MICHAEL D. BRAYDICH, Lt Col, USAF
Deputy Director
Aerospace Power Division
Aero Propulsion & Power Directorate

IF YOUR ADDRESS HAS CHANGED, IF YOU WISH TO BE REMOVED FROM OUR MAILING LIST, OR IF THE ADDRESSEE IS NO LONGER EMPLOYED BY YOUR ORGANIZATION PLEASE NOTIFY WL/POOC-3, WRIGHT-PATTERSON AFB, OH 45433-6563 TO HELP MAINTAIN A CURRENT MAILING LIST.

COPIES OF THIS REPORT SHOULD NOT BE RETURNED UNLESS RETURN IS REQUIRED BY SECURITY CONSIDERATIONS, CONTRACTUAL OBLIGATIONS, OR NOTICE ON A SPECIFIC DOCUMENT.

REPORT DOCUMENTATION PAGE			Form Approved OMB No. 0704-0188	
Public reporting burden for this collection of information is estimated to average 1 hour per response, including the time for reviewing instructions, searching existing data sources, gathering and maintaining the data needed, and completing and reviewing the collection of information. Send comments regarding this burden estimate or any other aspect of this collection of information, including suggestions for reducing this burden, to Washington Headquarters Services, Directorate for Information Operations and Reports, 1215 Jefferson Davis Highway, Suite 1204, Arlington, VA 22202-4302, and to the Office of Management and Budget, Paperwork Reduction Project (0704-0188), Washington, DC 20503.				
1. AGENCY USE ONLY (Leave blank)	2. REPORT DATE Oct 86	3. REPORT TYPE AND DATES COVERED Final Report 6/80 - 6/86		
4. TITLE AND SUBTITLE Application of the Photoacoustic and Photothermal Effects to Combustion Diagnostics		5. FUNDING NUMBERS C F33615-80-K-2035 PE 61102F PR 2301 TA S1 WU 19		
6. AUTHOR(S) Rajendra Gupta Gregory J. Salmo				
7. PERFORMING ORGANIZATION NAME(S) AND ADDRESS(ES) University of Arkansas Research and Sponsored Programs Fayetteville, AR 72701		8. PERFORMING ORGANIZATION REPORT NUMBER		
9. SPONSORING / MONITORING AGENCY NAME(S) AND ADDRESS(ES) Aero Propulsion and Power Directorate Wright Laboratory Air Force Systems Command Wright-Patterson AFB, OH 45433-7919		10. SPONSORING / MONITORING AGENCY REPORT NUMBER WL-TR-95-2055		
11. SUPPLEMENTARY NOTES				
12a. DISTRIBUTION / AVAILABILITY STATEMENT Approved for public release; distribution is unlimited.		12b. DISTRIBUTION CODE		
13. ABSTRACT (Maximum 200 words) There is presently a need for the development of combustion diagnostic techniques to measure such parameters as gas concentrations and local temperatures in practical flames. These techniques should (i) be non-perturbing to permit <u>in situ</u> measurements, (ii) have spatial resolution, and (iii) have temporal resolution. Optical techniques are best suited for this purpose since they easily satisfy all three criteria. In fact, several optical techniques have already been successfully used for specie concentration measurements, e.g., coherent anti-Stokes Raman scattering, spontaneous Raman scattering, and saturated fluorescence. However, there is currently no single technique which is suitable under all circumstances and all of the above techniques can be seen to have relative advantages and disadvantages over each other. Under the sponsorship of the United States Air Force, we have investigated the potential of the photoacoustic technique as a combustion diagnostic technique for measurement of minority species concentrations. In this report we discuss the results of this investigation.				
14. SUBJECT TERMS Photoacoustic combustion diagnostics, photothermal combustion diagnostics, photoacoustic deflection, photothermal deflection.		15. NUMBER OF PAGES 98		
		16. PRICE CODE		
17. SECURITY CLASSIFICATION OF REPORT Unclassified	18. SECURITY CLASSIFICATION OF THIS PAGE Unclassified	19. SECURITY CLASSIFICATION OF ABSTRACT Unclassified	20. LIMITATION OF ABSTRACT Unlimited	

Contents

Part I: Application of the Photoacoustic Effect to Combustion Diagnostics	
A. Introduction	1
B. Theory	4
(i) Single photon photoacoustic effect	4
(ii) Two-photon photoacoustic effect	7
C. Apparatus.	9
D. Results and Discussion	13
(i) Experiments with sodium seeded flame	13
(ii) Experiments with NO_2	13
(iii) Experiments with OH.	37
(iv) Two-photon experiments	52
E. Conclusion	54
F. References	58
Appendix I	60
Appendix II.	61
Appendix III	62
Appendix IV.	63
Part II: Application of the Photothermal Effect to Combustion Diagnostics.	70
A. Introduction	70
B. Discussion of the Photothermal Deflection Technique.	70
(i) Overlapping Pump and Probe Beams	71
(ii) Spatially Separated Pump and Probe Beams	76
(iii) Photoacoustic Deflection Technique	79
C. Apparatus.	82

D. Results and Conclusions.82
E. References84
F. Figure Captions and Figures.85

Part I
Application of the Photoacoustic Effect
to Combustion Diagnostics

A. Introduction

There is presently a need for the development of combustion diagnostic techniques to measure such parameters as gas concentrations and local temperatures in practical flames.^{1,2,3} These techniques should (i) be non-perturbing to permit in situ measurements, (ii) have spatial resolution, and (iii) have temporal resolution. Optical techniques are best suited for this purpose since they easily satisfy all three criteria. In fact, several optical techniques have already been successfully used for specie concentration measurements, e.g., coherent anti-Stokes Raman scattering, spontaneous Raman scattering, and saturated fluorescence. However, there is currently no single technique which is suitable under all circumstances and all of the above techniques can be seen to have relative advantages and disadvantages over each other. Under the sponsorship of the United States Air Force, we have investigated the potential of the photoacoustic technique as a combustion diagnostic technique for measurement of minority species concentrations. In this report we discuss the results of this investigation.

The photoacoustic effect was discovered by Alexander Graham Bell in 1880,⁴ however, it was largely ignored until recently. With the advent of lasers there has been a resurgence of interest in this technique.⁵ Stated very simply, the photoacoustic effect consists of the following: A sample (let us say, a molecular gas) is illuminated by light of such a wavelength that it is absorbed by the gas molecules. The excited molecules can either radiatively decay or lose their energy via collisions. The energy lost in collisions may subsequently appear as translational energy of the gas molecules. The temperature

of the gas rises, or equivalently, for constant volume, the pressure rises. If the light beam is amplitude modulated at acoustic frequencies, the pressure goes through periodic changes at acoustic frequencies and may be detected by a microphone. If the light source is pulsed, a pressure pulse may be detected. The technique is specie selective since the laser radiation may be tuned to excite a specific molecular or atomic species. The real advantage of this technique lies in the fact that small concentrations of the gases of interest can be detected in the presence of foreign gases at atmospheric pressure. Fluorescence spectroscopy in such circumstances is generally inappropriate since most of the excited molecules decay nonradiatively due to quenching collisions with foreign gas molecules. On the other hand, it is precisely under such circumstances that the photoacoustic effect is most effective.

The potential of the application of photoacoustic spectroscopy to flame studies was recently demonstrated by Crosley and collaborators.⁶ These authors found that in a flame seeded with Na, if a pulsed dye laser was tuned to the resonance lines of Na, the sound produced by the photoacoustic effect was easily audible to an observer standing within a meter of the burner. They have investigated this effect in some detail and have measured the speed of sound (and thus the temperature) and some quenching rates in the flame.

We started our investigation by repeating Crosley's experiment in Na, and we have confirmed his findings. In order to investigate the photoacoustic technique further, we applied it to measure low concentrations of NO_2 molecules produced in the combustion of methane and air.⁷ These investigations gave us valuable insights into the application of photoacoustic technique to combustion diagnostics and gave a detectivity limit of about $4 \times 10^{13} \text{ NO}_2 \text{ molecules/cm}^3$ ($\sim 10 \text{ ppm}$) with excellent temporal resolution. Although this investigation was

very successful in proving the excellent potential of this new application of photoacoustic technique, quantitative work proved to be difficult due to the following reasons: (i) NO_2 has a very complex spectrum in the visible region (almost a quasi-continuum). (ii) The optical absorption coefficient of NO_2 molecules is small and the NO_2 density in a methane-air flame is very low. (iii) The absorption coefficient of NO_2 at flame temperature is not known and it cannot easily be computed or measured. Therefore, in the second phase of this work, we have applied photoacoustic technique to OH molecules produced in the combustion of methane and air. OH molecules have a high concentration in this flame, and their spectrum is well resolved (discrete) and well understood. This has allowed a quantitative investigation of the photoacoustic effect in a flame. Our investigations on several isolated lines of the $A^2\Sigma^+ - X^2\Pi$ band of OH in the vicinity of 3100 \AA have proved the validity of the theoretical model.

In order to achieve spatial resolution using the photoacoustic technique, we have attempted to observe two-photon photoacoustic signal in OH molecules. In two-photon photoacoustic spectroscopy, each OH molecule is excited not by a single UV photon of frequency ν , but by two visible photons of frequencies ν_1 and ν_2 such that $\nu = \nu_1 + \nu_2$. If two laser beams are used to supply photons at ν_1 and ν_2 , then the excitation of OH molecules, and consequently the generation of the photoacoustic signal, occurs only at the crossing point of the two laser beams. Spatial resolution is thus achieved. We did not succeed in observing the two-photon signal. Apparently, the signal is smaller than that predicted by our crude theoretical model. A better theoretical model is required. We did not pursue these investigations further, since a better way to obtain spatial resolution appears to be by an optical detection of these signals--as described in Part II of this report.

B. Theory

(i) Single-photon photoacoustic effect

We assume a two-level model of the molecules. If the molecules are excited by light of intensity I_ν per unit frequency (Watts/m²·Hz), the number density N_2 of the excited molecules in the irradiated region is given by

$$N_2 = N_0 \frac{\gamma B_{12} I_\nu}{A_{21} + Q_2 + \gamma (B_{12} + B_{21}) I_\nu} \quad (1)$$

assuming a steady state has been reached. Here N_0 is the total number density of OH or NO₂ molecules (ground state plus excited state), and A_{21} , B_{12} , and B_{21} are the Einstein coefficients of spontaneous emission, absorption, and stimulated emission, respectively. γ is a factor which depends on the laser bandwidth and on the absorption linewidth of the molecules (see Appendix I). Q_2 is the total quenching rate of the excited state due to collisions with other molecules. If the quenching rate Q_2 is much larger than $[A_{21} + (B_{12} + B_{21}) I_\nu]$ (see Appendix II), the heat produced by the absorption of a laser pulse of duration τ_p is given by

$$H = N_0 V \gamma B_{12} I_\nu h\nu \tau_p \quad (2)$$

where $h\nu$ is the laser photon energy and V is the volume of the irradiated region. Here we have assumed that all the energy lost by the molecules in quenching collisions goes into heating the flame gases. We have also made the adiabatic approximation, i.e., we have neglected the diffusion of heat from the irradiated volume during the laser pulse duration. Moreover, implicit in Eq(2) is the assumption that the medium is weakly absorbing, i.e., I_ν is not significantly modified as the laser propagates in the medium. We further assume that the laser pulse is long compared to the acoustic transit time across the cylindrical optical beam in the flame ($\tau_p > r/v_a$, v_a being the acoustic

velocity), so that the local temperature equilibrium is maintained. The rise in the temperature of the irradiated gases is given by

$$\Delta T = \frac{N_o V \gamma B_{12} I_v h \nu \tau_p}{C_p} \quad (3)$$

where C_p is the heat capacity at constant pressure of the irradiated volume V . If we assume that most of the flame gases are diatomic, C_p is simply $(9/2) Nk$ where N is the number of molecules of the flame gases in irradiated volume, and k is the Boltzman constant.

One simple way to estimate the photoacoustic signal is to calculate the pressure change p due to rise in temperature ΔT :

$$p = (2/9) N_o \gamma B_{12} I_v h \nu \tau_p \quad (4)$$

For a cylindrical pressure wave, the pressure change $P_o(R)$ observed at the microphone, a distance R away from the irradiated region, is

$$P_o(R) = (2/9) N_o \gamma B_{12} I_v h \nu \tau_p \left(\frac{r}{R}\right)^{1/2} \quad (5)$$

where r is the radius of the irradiated region. This result is equivalent to that of Tennal et al.⁷

Another way of approaching the problem, followed by Patel and Tam,⁸ is to calculate the volumetric expansion of the irradiated region due to the rise in temperature:

$$\pi(r + \Delta r)^2 \ell - \pi r^2 \ell = \beta V \Delta T = \frac{\beta N_o V^2 \gamma B_{12} I_v h \nu \tau_p}{C_p} \quad (6)$$

Here β is the volume expansion coefficient of the flame gases and Δr is the increase in the radius of the irradiated cylindrical volume of length ℓ due to the expansion. From Eq(6), Δr may be given approximately by

$$\Delta r = \frac{\beta N_o V \gamma B_{12} I_v h \nu \tau_p r}{2 C_p} \quad (7)$$

In this model, the increase Δr of the radius results in a cylindrical compression around the irradiated volume, which travels radially outward with sound velocity. The compressor wave is followed by a rarefaction wave. The magnitude of the signal observed by the microphone is proportional to Δr .

In this model we want to predict the size as well as the shape (in time) of the signal. Therefore we must write $\Delta r(t')$ explicitly as a function of time. To this end, we assume the shape of the laser pulse to be a Gaussian, centered around $t' = 0$, with width $\tau_p = 2\tau$, and total energy E_0 :

$$I(t') = \int I_v(t') dv = \frac{E_0}{\pi^{3/2} r^2 \tau} e^{-(t'/\tau)^2} \quad (8)$$

To solve the problem of sound generated by a cylindrical line source, Patel and Tam follow the treatment given by Landau and Lifshitz.⁹ The velocity v and the pressure p in excess of the unperturbed value are derivable from a potential ϕ by

$$\vec{v} = \vec{\nabla} \phi \quad (9)$$

and

$$p = -\rho \frac{\partial \phi}{\partial t} \quad (10)$$

where ρ is the density of the flame gases. For a problem with cylindrical symmetry,

$$\phi(R, t) = -\frac{v_a}{2\pi} \int_{-\infty}^{(t - R/v_a)} \frac{\dot{S}(t') dt'}{[v_a^2 (t - t')^2 - R^2]^{1/2}}. \quad (11)$$

Here $\dot{S}(t')$ is the time derivative of the cross sectional area $S(t')$ of the cylindrical source,

$$S(t') = \pi[r + \Delta r(t')]^2, \quad (12)$$

and may be calculated from Eqs (7) and (8). If the observation point is sufficiently far away from the irradiated region, the solution of (11) may be

written as⁸

$$p(R, t) = \frac{2BN_o V \gamma B_{12} I_v h \nu r^2 V_a \rho}{(2\pi R)^{1/2} \tau^2 C_p} \int_{-\infty}^{(t - R/V_a)} \frac{t' e^{-(t'/\tau)^2} dt'}{[V_a(t - t') - R]^{1/2}} \quad (13)$$

Eq(13) predicts that $p(R, t)$ has its largest magnitude at times

$$t_{\pm} = (R/V_a) \pm 0.7\tau \quad (14)$$

The approximate magnitude of the signal at the peaks is given by

$$P_o(R) \equiv p(R, t_{\pm}) = \pm \frac{2BN_o V \gamma B_{12} I_v h \nu r^2 \rho}{C_p \tau} \left(\frac{V_a \tau}{2\pi R} \right)^{1/2} \quad (15)$$

Eq(13) predicts that a compression wave of amplitude given by Eq(15) is followed by a rarefaction wave of nearly equal amplitude, the two waves being nearly 1.4τ apart in time.

(ii) Two-photon photoacoustic spectroscopy

The two-photon transition probability may be calculated using the second order perturbation theory (see Grynberg and Cagnac¹⁰). The probability of excitation of an atom from the ground state g to an excited state e is given by¹⁰

$$P_{ge}(\delta\omega) = \left| \sum_i \frac{\langle e | \mathcal{H}_1 | i \rangle \langle i | \mathcal{H}_2 | g \rangle + \langle e | \mathcal{H}_2 | i \rangle \langle i | \mathcal{H}_1 | g \rangle}{\Delta\omega_i} \right|^2 \times \frac{\Gamma_e}{4\delta\omega^2 + (1/4)\Gamma_e^2} \quad (16)$$

Here the following notation is used: Γ_e is the homogeneous linewidth of the excited state. $\delta\omega = \omega - \omega_o$ is the difference between the laser angular frequency ω and the resonance frequency $\omega_o = (E_e - E_g)/2\hbar$. \mathcal{H}_1 and \mathcal{H}_2 are the electric dipole interaction Hamiltonians (divided by \hbar) of the atom for interaction with the two laser beams. $\hbar\Delta\omega_i = \hbar\omega - (E_i - E_g)$ is the energy defect of the one photon transition for each intermediate state i . The Lorentzian lineshape function represents the homogeneous width of the line. Note that the parity of g and e states should be the same while that of the i state should be opposite.

Grynberg and Cagnac¹⁰ have derived an explicit expression for the transition probability P_{ge} for an atom under the following conditions: The two laser beams are identical, i.e., they have the same frequency, intensity, and polarization, and there is only one intermediate level r , which contributes significantly to the transition probability. In other words, the energy defect $\hbar\Delta\omega_r \ll \hbar\Delta\omega_i$ ($i \neq r$), and the oscillator strengths for this intermediate level f_{gr} and f_{re} are not too small. Under these conditions, one gets, if the lasers are tuned on resonance ($\delta\omega = 0$),

$$P_{ge}(0) = \frac{1}{\Gamma_e} \left(\frac{3}{\pi} \frac{r_o \lambda_{gr} \lambda_{re}}{\hbar c} \right)^2 I_o^2 \frac{\omega_{gr} \omega_{re}}{\Delta\omega_r^2} f_{gr} f_{re} C_1^2 C_2^2 \quad (17)$$

Here $r_o = 2.8 \times 10^{-15}$ m is the classical radius of the electron, and λ_{gr} and λ_{re} are the wave lengths and f_{gr} and f_{re} the oscillator strengths of the one-photon transitions involved. C_1 and C_2 are the appropriate Clebsch-Gordan coefficients which depend on the polarization of the light and the angular momentum quantum numbers of the ground, intermediate, and the excited states. I_o is the intensity (watts/m²) of the laser beam.

Eq(17), although derived for the case of atoms, can be used for OH molecules to obtain order of magnitude estimates. Appropriate modification to Eq(17) must, however, be made. For excitation of the $x^2\Pi \rightarrow A^2\Sigma$ band, there is no single intermediate state for which the energy defect $\Delta\omega_r$ is small. As a matter of fact, the most favorable oscillator strength is provided by states which lie higher than $A^2\Sigma$, and have parity opposite to that of the $A^2\Sigma$ state. There are very many such states, and a summation over all the intermediate states r is necessary:

$$P_{ge}(0) = \frac{1}{\Gamma_e} \sum_r \left(\frac{3}{\pi} \frac{r_o \lambda_{gr} \lambda_{re}}{\hbar c} \right)^2 I_o^2 \frac{\omega_{gr} \omega_{re}}{\Delta\omega_r^2} f_{gr} f_{re} C_1^2 C_2^2 \quad (18)$$

We note that Eq(18) is not quite accurate, because implicit in Eq(18) is the assumption that the sum of the cross terms of the matrix elements in Eq(16) is zero. This is not necessarily a good assumption, however, for order of magnitude estimates Eq(18) is useful. Evaluation of Eq(18) presents a two-fold problem. First, summation over a large number of intermediate states is involved, and second, we do not know the oscillator strength of each transition. However, the two problems together offer a solution. The sum of all the oscillator strengths f_{gr} for an allowed electric dipole transition should be of the order of one. Same holds for f_{re} . To be on the conservative side, we will assume these sums to be each about 0.3. Also, we will assume that $C_1^2 C_2^2 = 0.1$.

Finally, Eq(17) is derived for the case where the laser linewidth and the homogeneous linewidth are about equal and the inhomogeneous linewidth is much larger. In our case, all three linewidths are comparable. The problem of lineshapes in two-photon spectroscopy is a complicated one, and we will assume that for our purposes, Eq(18) is useable.

In order to obtain two-photon photoacoustic signals, single photon transition probability $\gamma B_{12} I_\nu$ must be replaced by the two-photon transition probability $P_{ge}(0)$ in Eqs(2) through (15).

C. Apparatus

Our experimental set up is shown in Fig. 1. Light from a chromatix CMX-4 flash-lamp pumped dye laser was used to excite NO_2 molecules in the flame. The laser produces ~ 1 μsec long pulses with an average energy of about 9 mJ/pulse and with a bandwidth of about 3 cm^{-1} . The burner is a stainless steel flat-flame burner (Fig. 2) which is operated at atmospheric pressure. We use an oxygen rich mixture of O_2 , CH_4 , and N_2 for fuel. The burner is enclosed inside a glass cross. The combustion products are exhausted out of the room through

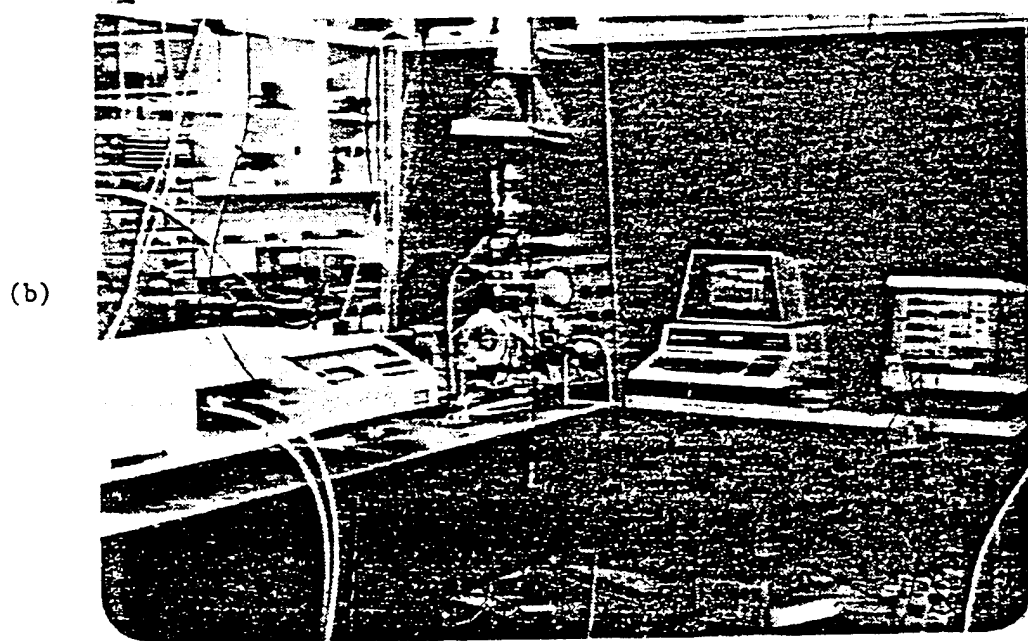
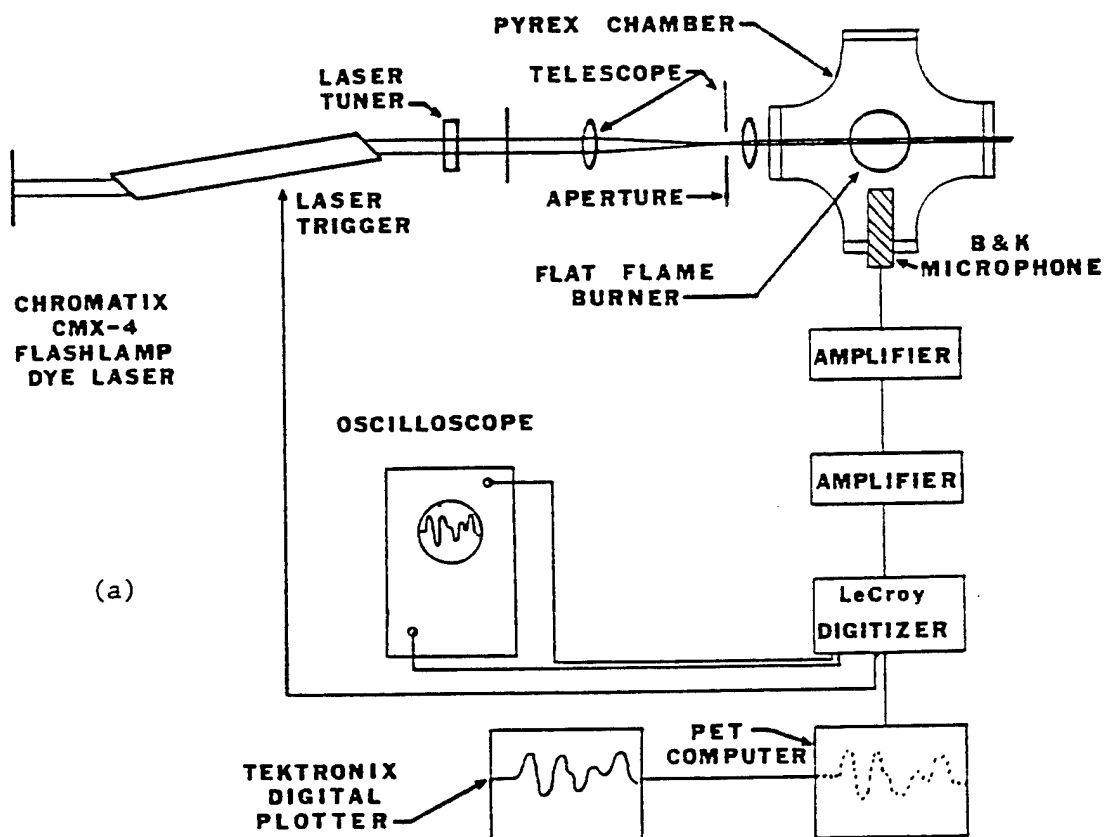
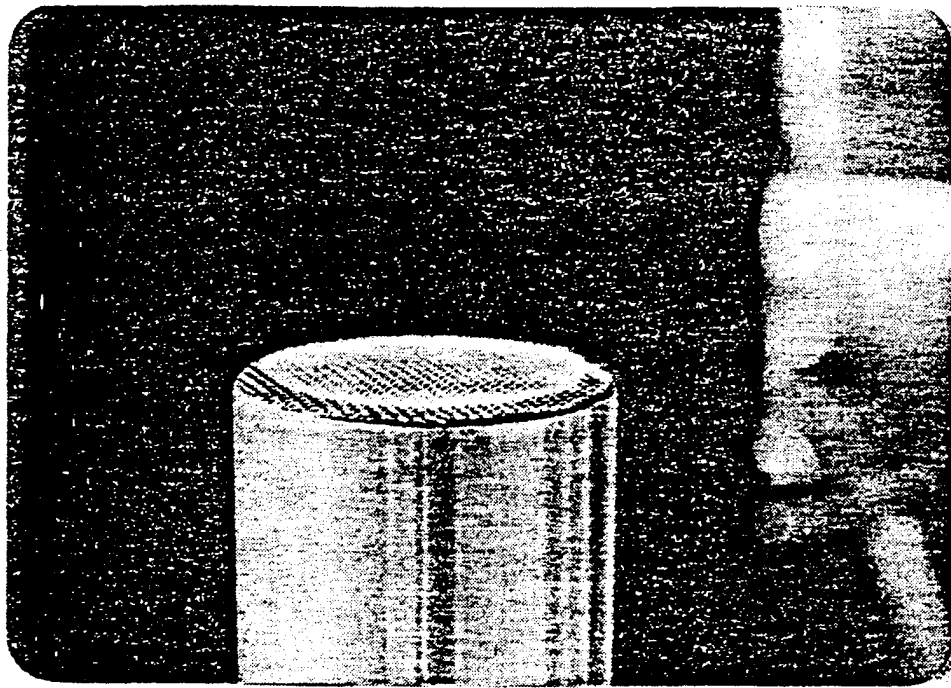


Figure 1: Experimental equipment



(a)



(b)

Figure 2: Pictures of burner. (a) Burner head with round flame on. The top porous disk is covered with a wire mesh in this case. (b) Burner inside pyrex cross.

the top of the cross. The laser beam enters and exits through two side ports and a microphone is inserted through a third side port, as shown in Fig. 1. The diameter of the burner head and that of the flame are approximately 6 cm. Under atmospheric pressure condition a faint blue flame is formed about 1.5 millimeter thick and situated a small fraction of a millimeter above the burner head. A Bruel and Kjaer Model 4135 condenser microphone is used to detect the photoacoustic signal. This microphone has a bandwidth of about 50 KHz and sensitivity of about 0.5 mV per mTorr. The output of the microphone amplified using a Bruel and Kjaer 2619 preamplifier, and either a Tektronix Type 123 or Le Croy TR 1000T preamplifier, is displayed on a Tektronix 545 oscilloscope. The oscilloscope trace is triggered by a pulse from the flash-lamp circuitry of the laser. When signal averaging is required, the output of the Tektronix preamplifier is fed to a LeCroy WD8256 waveform digitizer. The digitizer data is transferred to a Commodore PET microcomputer which is used as a signal averager. The averaged signal is viewed on the microcomputer screen and plotted on a Tektronix plotter. The details of the digitizer-microcomputer interface are given in Appendix IV.

In order to excite OH molecules, laser frequency was doubled using an intracavity ADP crystal. Using a high finesse etalon, the laser delivers an average energy of about 0.25 mJ/pulse in a bandwidth of about 0.3 cm^{-1} . Laser dye used was Rhodamine 6G in 4% Amino Lo solution. This solution shifts the dye gain peak toward red, giving higher second harmonic laser power of 3100 \AA .

Due to the limited bandwidth of the microphone, some of our measurements are taken with a pzt transducer. Panametrics V306 transducer with Model 5662 preamplifier was used. The transducer has a bandwidth of 2.25 MHz and a

sensitivity of 0.32 mV/Pa, however, this sensitivity is drastically reduced due to poor impedance match between the flame gases and the transducer.

D. Results & Discussion

(i) Experiments with sodium seeded flame

As a starting point, we have repeated Crosley's experiment.⁶ Our experimental set up was quite similar to that of Crosley except that our burner was very crude. We used an ordinary Bunsen burner sprinkled with table salt. The resulting sodium vapor in the flame was excited by a Chromatix CMX-4 dye laser and the photoacoustic signals were detected by a Knowles BT 1759 microphone. The signal output from the microphone was observed on an oscilloscope, triggered by a pulse from the flash-lamp circuitry. A typical oscilloscope trace is shown in Fig. 3. The signal was so strong that it was easily audible to the experimenter, confirming Crosley's results and indicating the enormous sensitivity of this technique.

(ii) Experiments with NO₂

A methane-air flame in a flat-flame burner produces a very low concentration of NO₂.¹¹ As a starting point in these experiments, we seeded the flame with small amounts of NO₂ in order to make the signal easily observable on a single-shot basis. A 500 ppm mixture of NO₂ in nitrogen, along with methane and oxygen, was used in the burner. A microphone was placed about 5 cm from the laser-flame interaction region for this experiment. A typical single-shot photoacoustic signal is shown in Fig. 4. In order to determine if the first dip was coming from the flame, we made speed of sound measurements. Leaving the microphone position fixed, the laser beam position in the flame was moved and relative arrival times of the photoacoustic signals recorded. Typical data are shown in Fig. 5. Successive signals, from top to bottom, were taken by

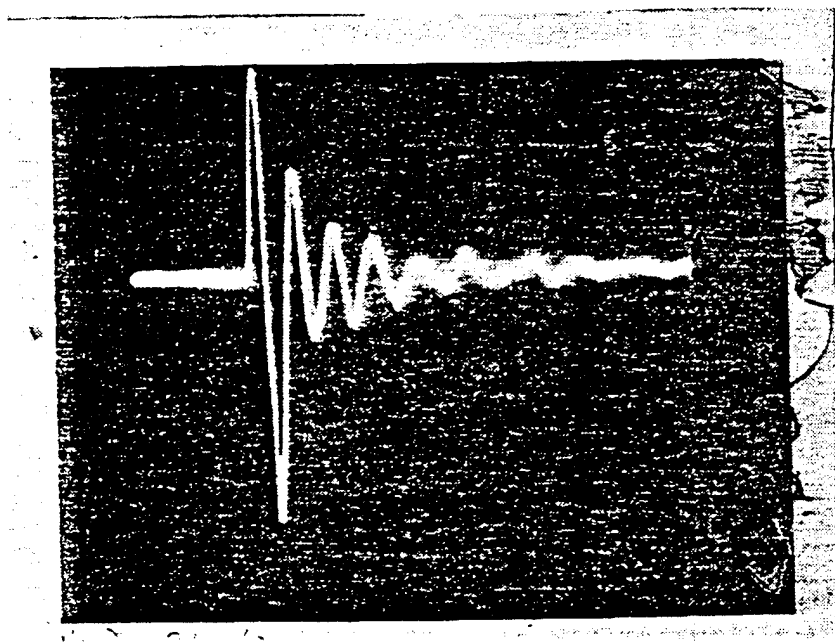


Figure 3: Photoacoustic signal generated in a Bunsen burner seeded with sodium.

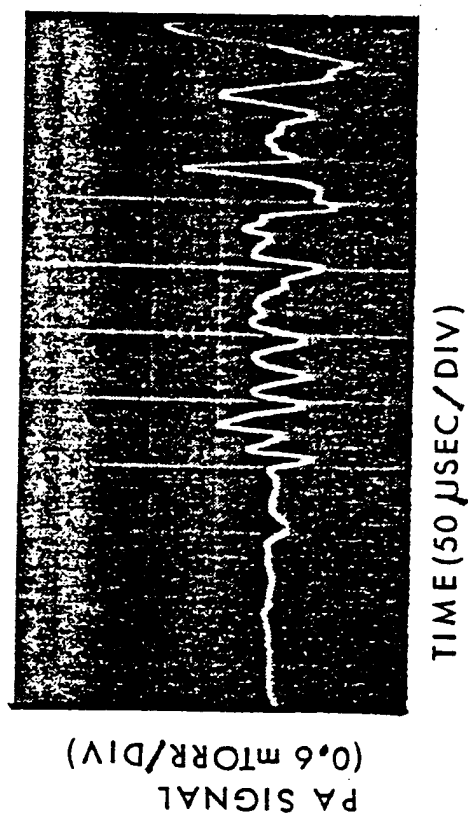


Figure 4: Photoacoustic signal generated in a methane-oxygen-nitrogen flame seeded with 350 ppm of NO_2 . This is a photograph of a single-shot oscilloscope trace.

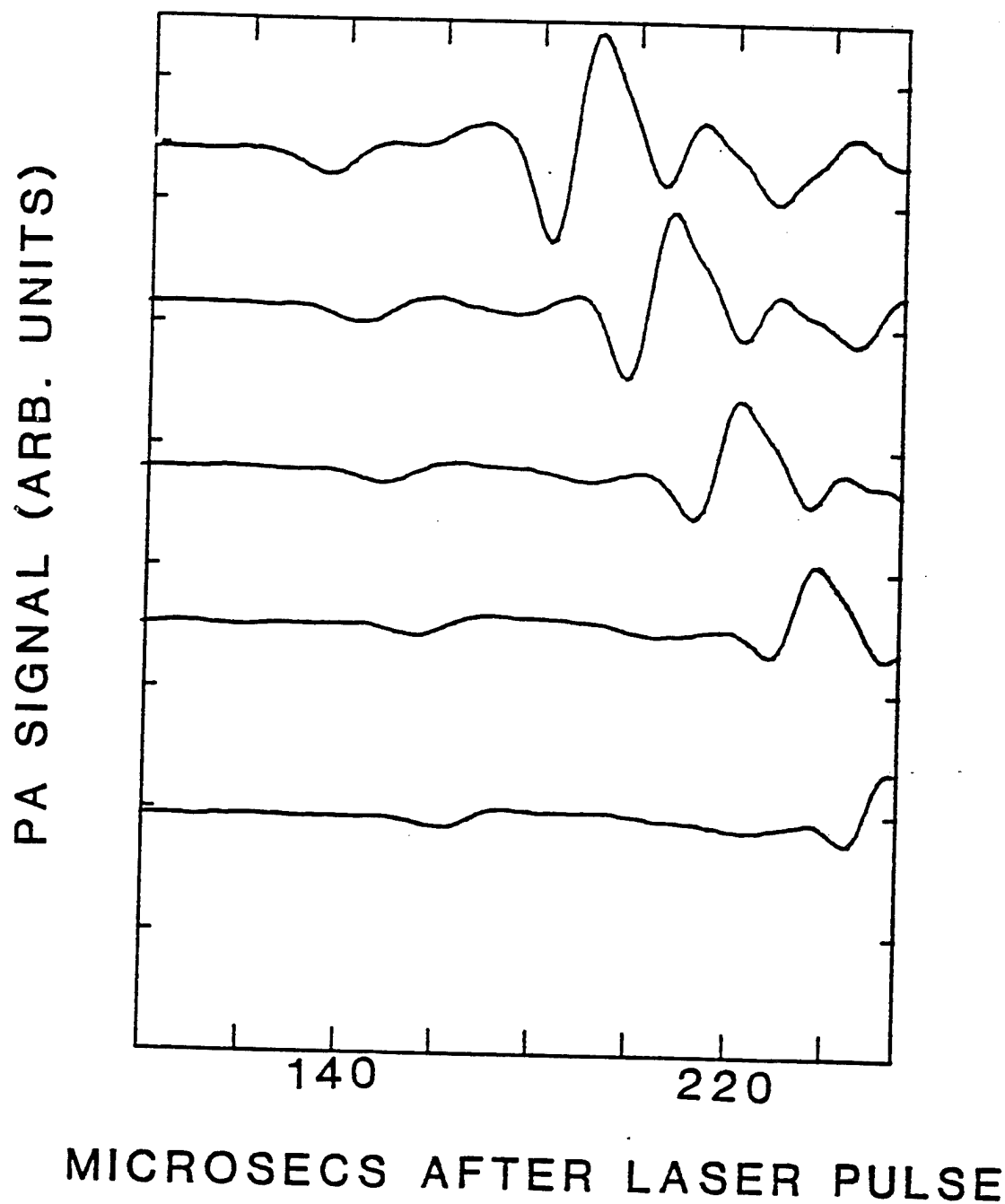


Figure 5: Change in the arrival times of the photoacoustic signal with changes in the laser beam position in a NO_2 seeded flame. Successive traces, from top to bottom, correspond to a shift of the laser beam position by 7 mm away from the microphone.

moving the laser beam by about 0.7 cm away from the microphone. These data clearly indicate that the velocity of the first dip is much larger than that of the subsequent structure. Since the velocity of sound is much larger in the flame than outside the flame, the data indicates that the first dip is coming from the flame whereas the subsequent structure is coming from outside the flame and is due to absorption of the laser radiation in other parts of the burner enclosure (cross) where the NO_2 density is higher and by reflection from the walls of the cross. A closer examination of the absolute arrival times* of the photoacoustic pulse showed, however, that the first signal did not originate at the center of the flame but originated at the boundaries of the flame, as shown in Fig. 6. No signal from the center of the flame was observed in this experiment. Comparison of the amplitude of this signal with photoacoustic signal generated by known concentrations of NO_2 at room temperature indicates that this signal corresponds to a NO_2 density of approximately 10^{14} molecules/cm³. The validity of the assumptions involved in arriving at this number will be discussed later in this section. It is clear from this experiment that most of the NO_2 is dissociated in the flame.

In the next phase of this experiment, we have observed the NO_2 produced as a result of the combustion process in the unseeded methane-air flame by increasing the sensitivity of our detection apparatus. First, we used a wave form digitizer interfaced with a Commodore PET microcomputer to do signal averaging over several pulses and thereby increasing the signal-to-noise ratio. Second, we covered about one-quarter of the flame with a stainless steel sheet. This allowed the microphone to be placed closer to the laser-flame interaction

*Expected arrival time of acoustic signal from the center of the flame was determined experimentally by measuring the arrival time of the acoustic pulse generated by laser radiation absorbed by a wire placed at the center of the flame.

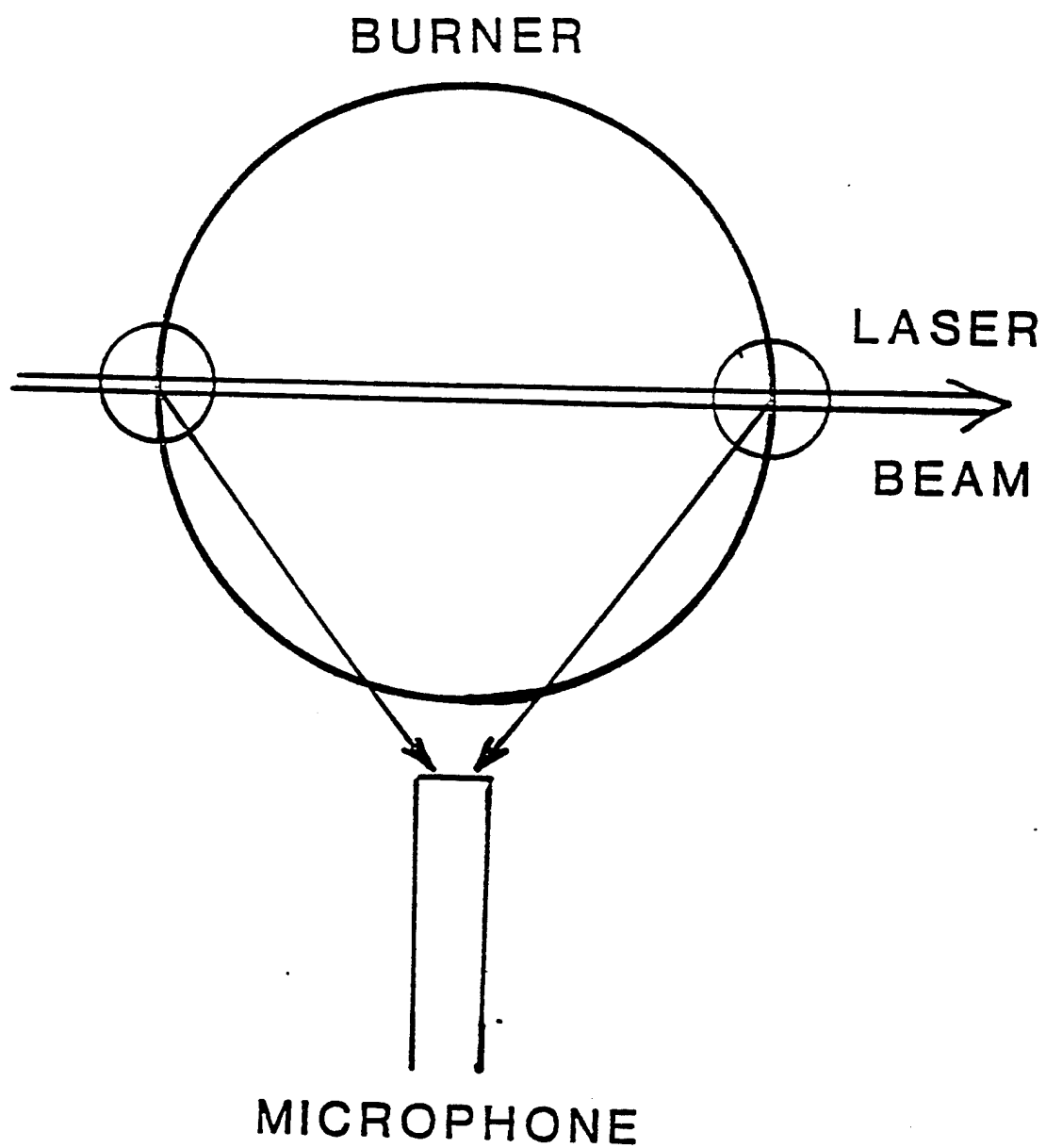


Figure 6. Diagram showing the regions where the observed photoacoustic signal (first dips in Figs. 4 and 5) originated.

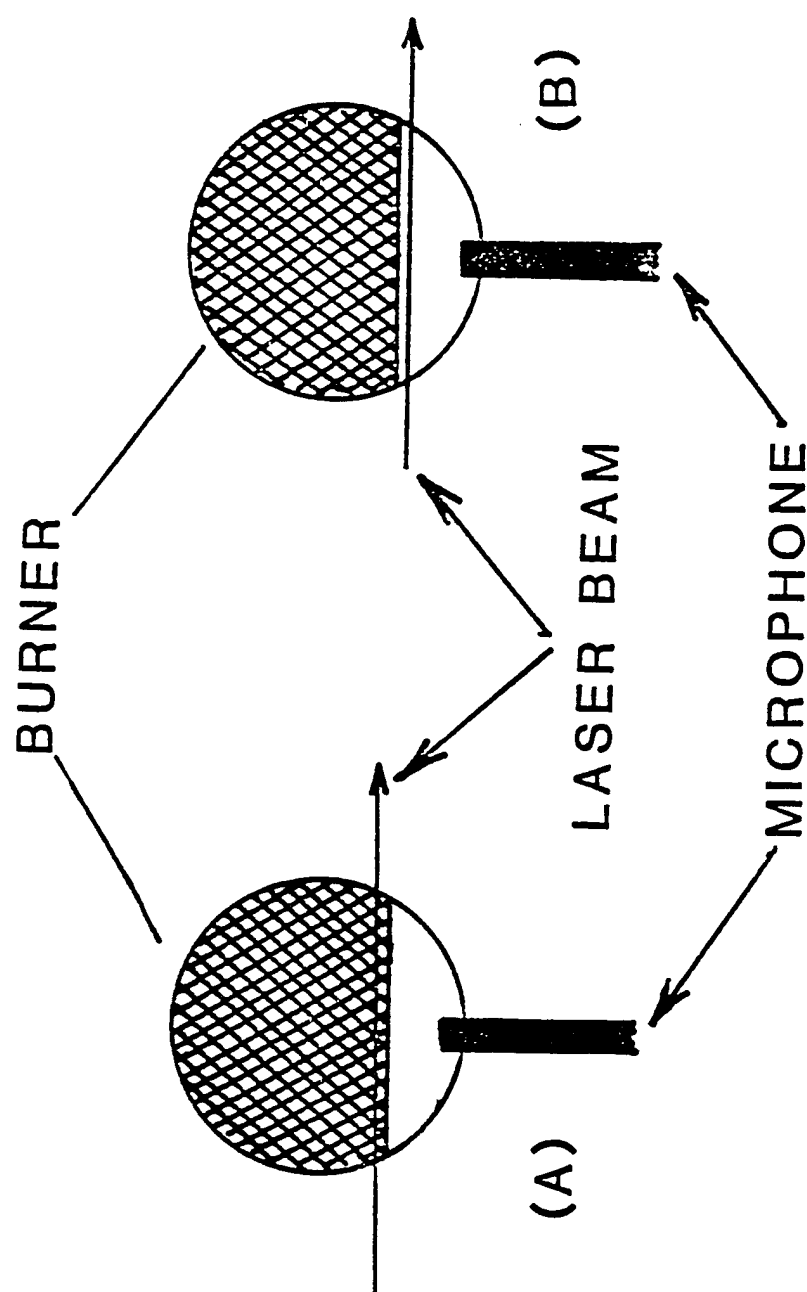


Figure 7. Diagram showing the relative positions of the flame, laser beam, and microphone for data shown in (a) Fig. 8, (b) top curves in Figs. 9(b) and 10(b).

region as shown in Fig. 7, and allowed a long beam path length near the edge of the flame where the NO_2 concentration is apparently larger thereby increasing the sensitivity of detection. Third, the width of the laser beam was reduced from a 4 mm dia to a 1 mm dia by using a telescope. Fig. 8 shows our typical data for two laser beam heights above the flame. The laser beam microphone distance was 3 cm. The structures marked with an arrow are the photoacoustic signals generated 4 mm (top curve) and 3 mm (bottom curve) above the luminous region of the flame. These data represent results of averaging over 1000 laser pulses.

The density of lines in the NO_2 absorption spectrum in the visible region is very large.¹² Moreover, these lines are pressure and Doppler broadened in a flame. Therefore NO_2 has almost continuous absorption in the visible and it is not possible to tune on or off specific absorption lines to ascertain the identity of the absorbing molecules. In order to ascertain that the observed signal is indeed due to NO_2 produced in the combustion process we have done the following experiments: We have compared the low resolution photoacoustic spectrum of NO_2 at room temperature with the low resolution spectrum of the observed photoacoustic signals in an unseeded methane-air flame. The results are shown in Figs. 9 and 10. Fig. 9 (a) shows the photoacoustic spectrum of NO_2 , taken with 43 ppm of NO_2 in nitrogen, in the rhodamine 6 G region. For comparison, in Fig. 9 (b) we show the photoacoustic spectrum of the flame for three different laser beam positions in the same spectral range. The top signal was obtained with the laser beam 8.5 mm outside the flame [Fig. 7 (b)]. The middle and bottom curves were taken with laser beam position shown in Fig. 7 (a), 8 mm and 3 mm above the burner head, respectively. Fig. 10 shows similar data in the blue region of the spectrum (LD 490 dye range). Similarity between the photoacoustic spectrum of NO_2 and that of the cooler parts of the

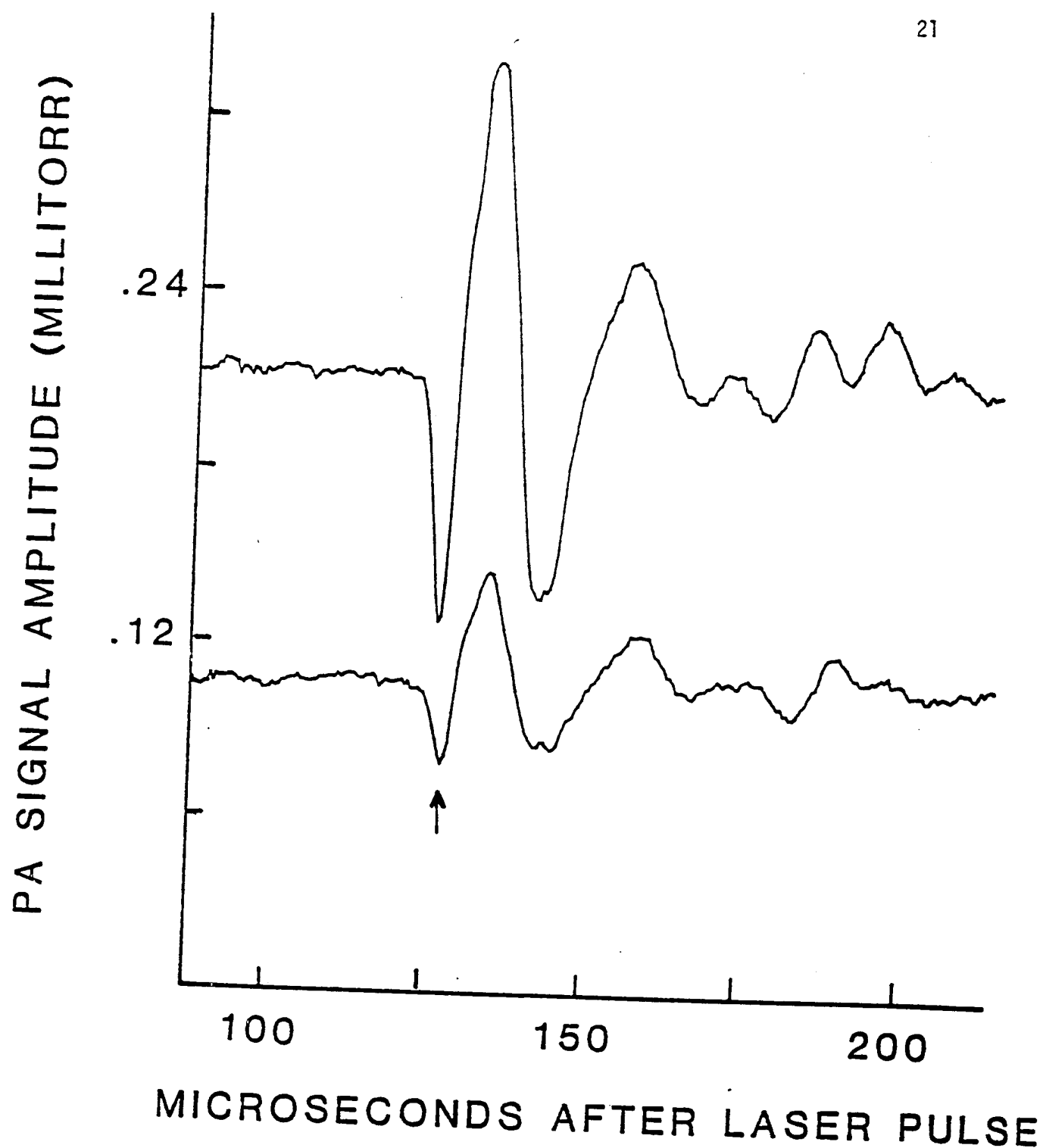


Figure 8. Photoacoustic signals generated in an unseeded oxygen-rich flame. The two traces, top and bottom, are for the laser beam 4 mm, 3mm, above the luminous region of the flame, respectively. The lateral position of the laser beam was as shown in Fig. 7(a) and it was collimated to a diameter of 1 mm. The incident laser energy was about 9 mJ/pulse at 4900 Å. These curves represent averaging over 1000 pulses. The arrow shows the position of the photoacoustic signal from the flame. The subsequent structure is mostly the photoacoustic signal from the flame. The subsequent structure is mostly the photoacoustic signals generated in the other parts of the burner enclosure which arrive later at the microphone, rather than noise. See Fig. 18 for noise data.

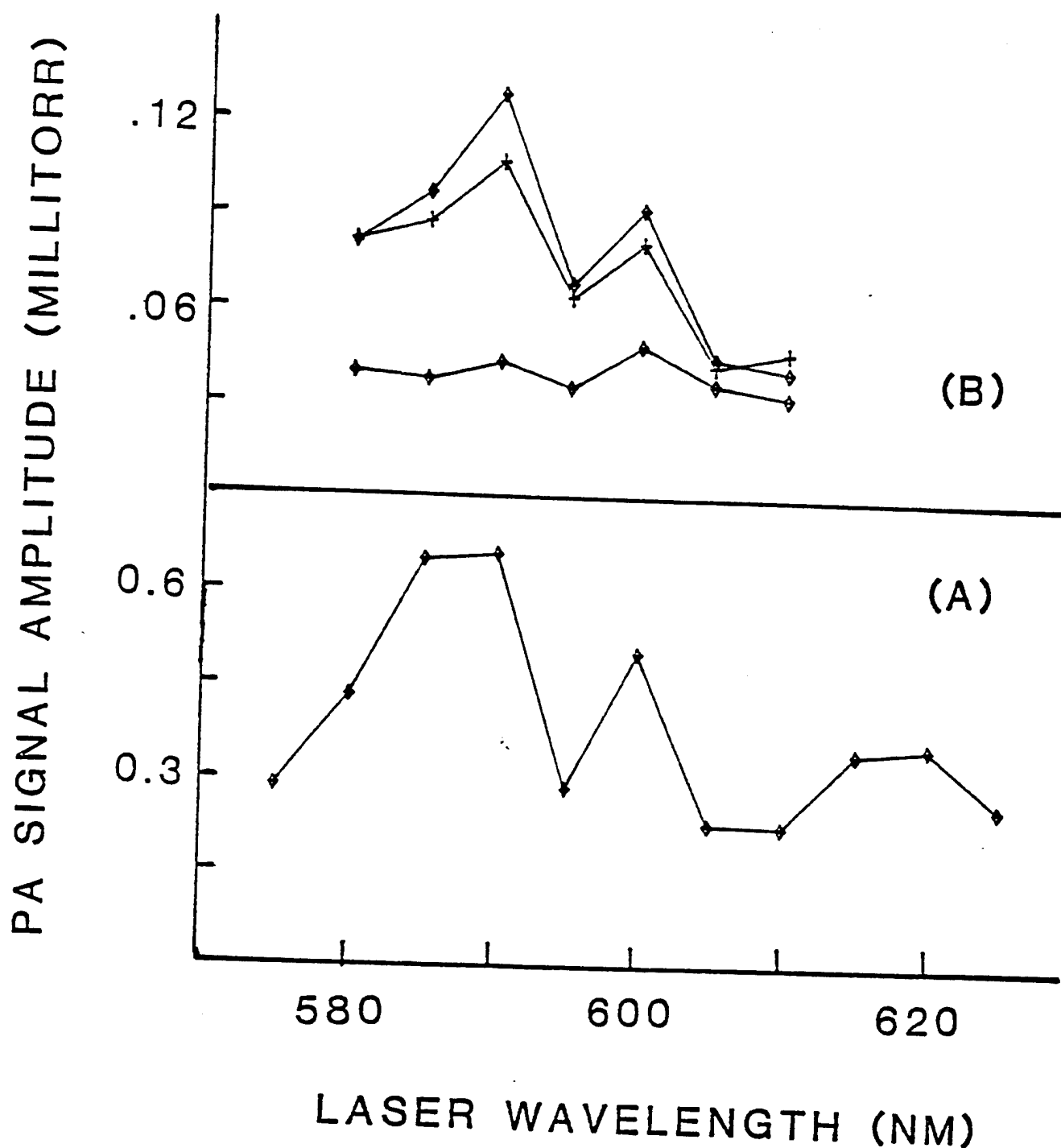


Figure 9. Frequency dependence of the photoacoustic signal amplitude for (a) 43 ppm NO_2 in N_2 with no flame and (b) in an unseeded flame.

The top curve was taken with the laser beam outside the flame [Fig. 7(b)] about 9 mm above the burner head, and the middle and the bottom curves were taken with the laser beam 7 mm and 3 mm, respectively, above the flame as shown in Fig. 7(a). These data are normalized with the laser power.

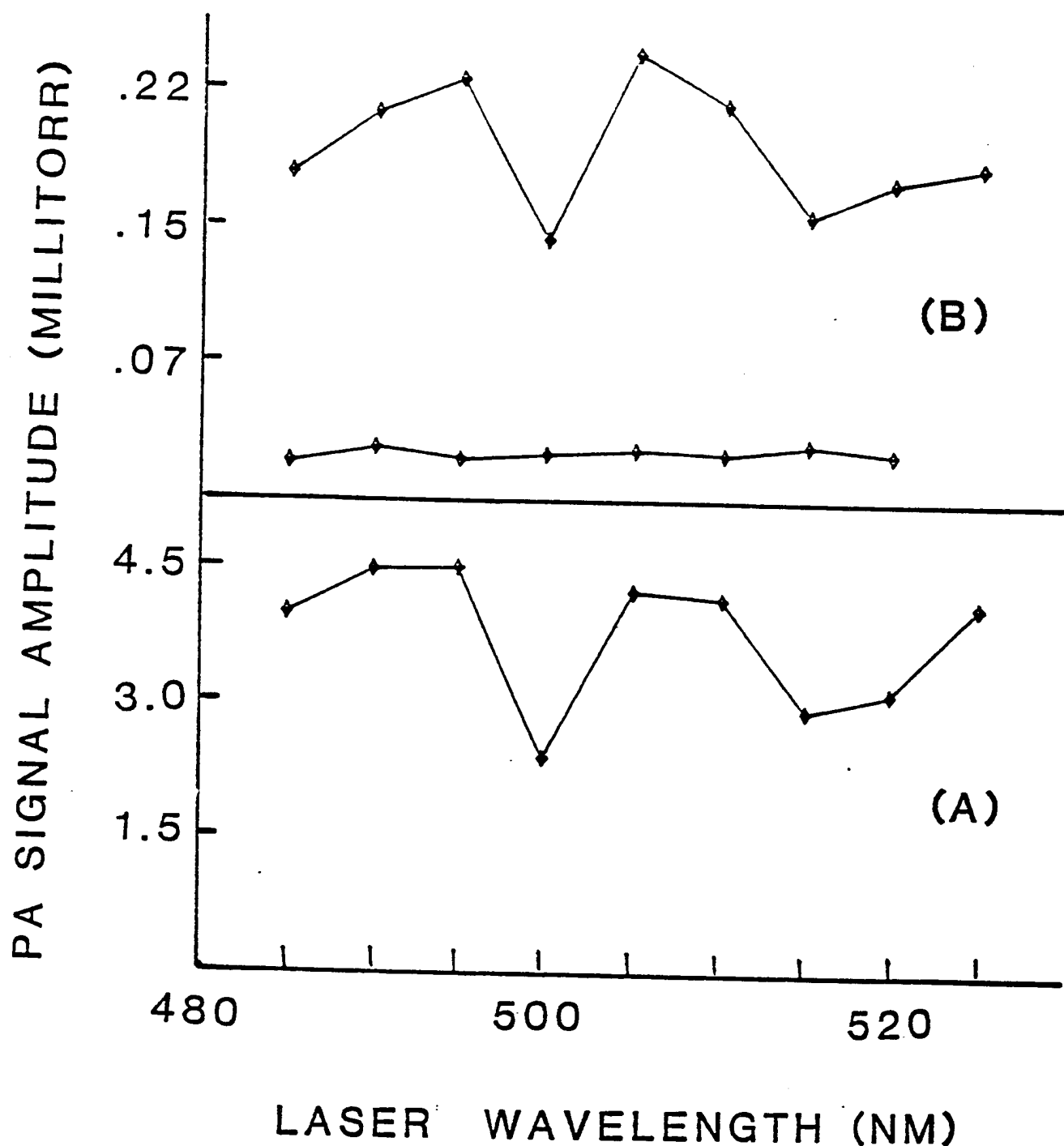


Figure 10. Frequency dependence of the photoacoustic signal, similar to Fig. 9, in the blue region of the spectrum. Figs. 9 and 10 have been taken under identical conditions so that direct comparison of signal amplitude between the two figures is possible. The data corresponding to the middle curve in Fig. 9(b) was not taken in the blue range.

flame shown in Fig. 9 leave little doubt that what we are observing is NO_2 . Moreover, we know of no other molecule which could be produced in the combustion of methane, nitrogen, and oxygen and which has a continuous spectrum in the visible region. It is clear from Figs. 9 and 10 that this spectrum has much less structure and the signal is much smaller in the hotter regions of the flame. The effect is particularly dramatic in the blue region. We note that the photoacoustic signal is about eight times larger in the blue region than in the red region for the non-flame conditions [Figs. 9 (a) and 10 (a)]. This is consistent with the wavelength dependence of the absorption coefficient of NO_2 . This ratio is much smaller in the hot gases outside the combustion region and is almost unity close to the visible flame. From these data it is not possible to tell if the reduced photoacoustic signal at higher temperatures is due to a lower absorption coefficient, lower NO_2 density, partial dissociation of NO_2 after optical absorption, or a combination of these effects. This point will be discussed further later in this section. A low resolution photoacoustic spectrum of the flame over a wider spectral region for two different laser beam heights is shown in Figure 11. These data were taken with four different laser dyes and have been normalized with the laser intensity.

In order to further ascertain the identity of NO_2 molecules, we introduced a small amount of monomethylamine in the fuel mixture. Addition of monomethylamine increases the concentration of NO_2 produced in the combustion process.¹¹ We observe a factor of 20 increase in our photoacoustic signal as shown in Fig. 12. This observation is further evidence that the observed photoacoustic signals are due to NO_2 molecules.

It was mentioned previously that the NO_2 density is higher near the edge of the flame. In Fig. 13 we show the amplitude of the photoacoustic signal

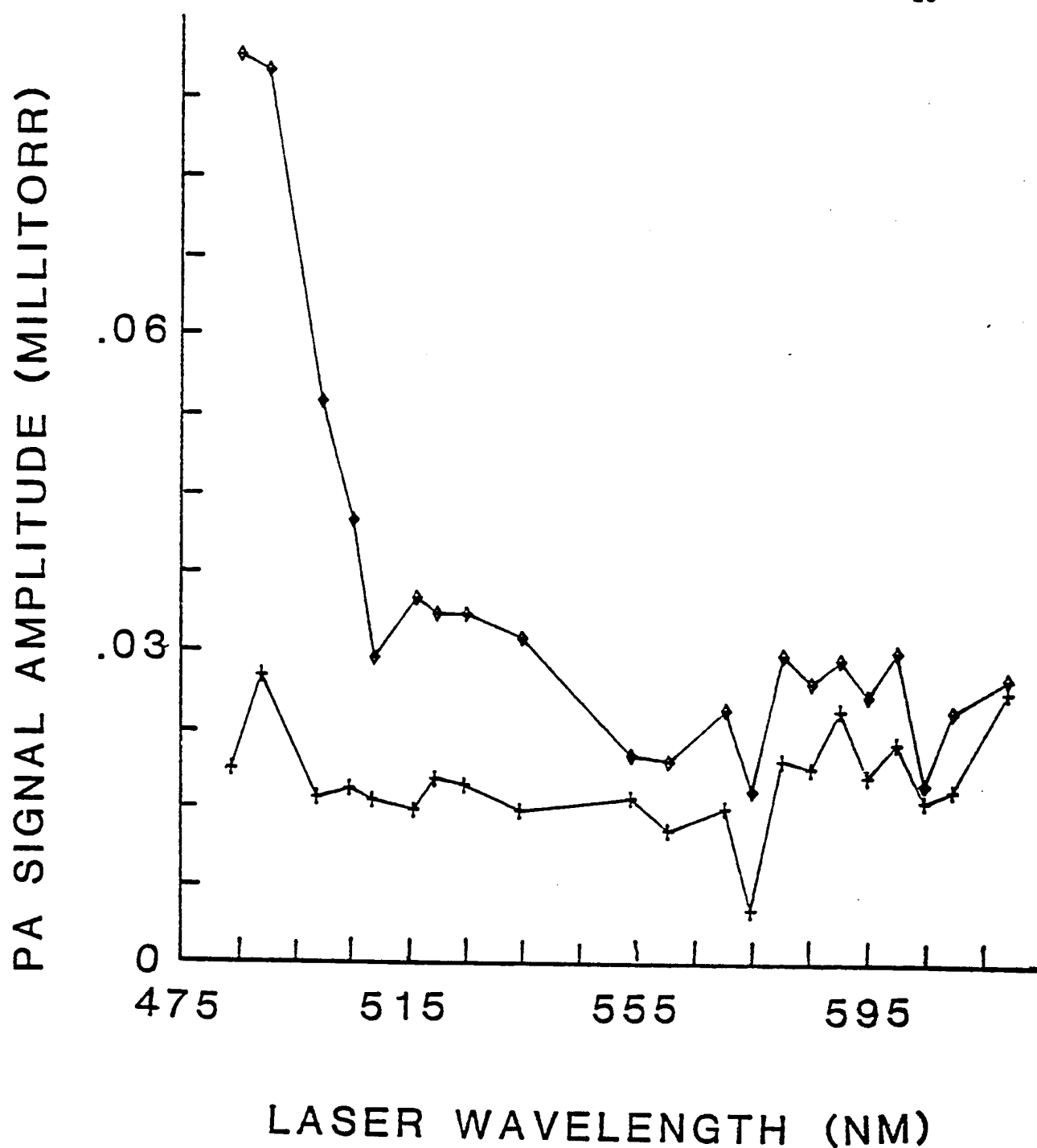
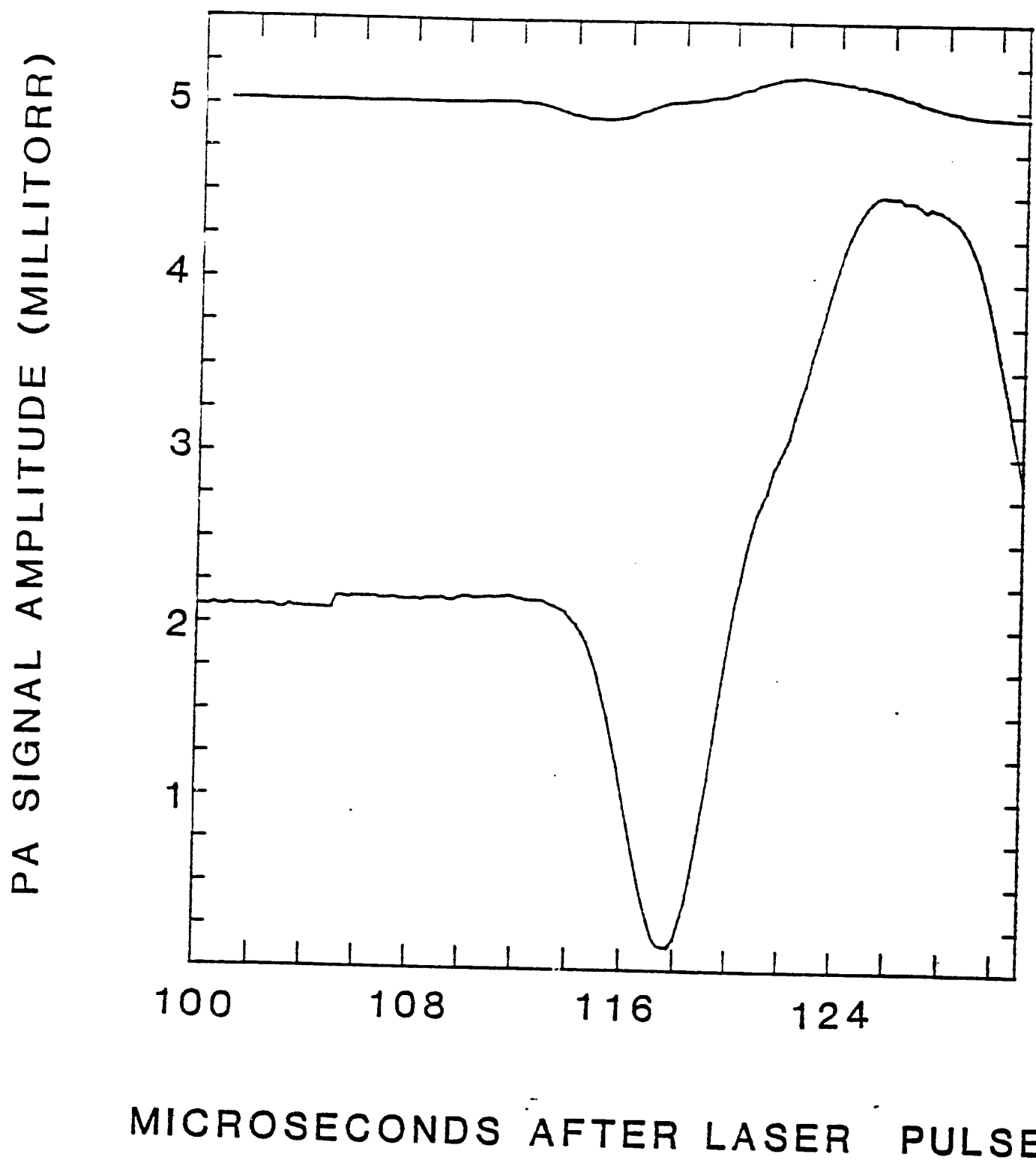


Figure 11. The frequency dependence of the photoacoustic signal in the flame over a wide spectral range. These data have been taken with four different dyes and are normalized with the laser power. The upper and lower curves were taken with the laser beam 4 mm and 3 mm, respectively, above the flame.



MICROSECONDS AFTER LASER PULSE

Figure 12. Increase in the NO_2 concentration in our flame due to addition of monomethylamine to the fuel-mixture. The top curve was taken for the unseeded flame while the bottom curve was taken for flame seeded with 75 ppm monomethylamine. The laser beam was about 6 mm above the flame.

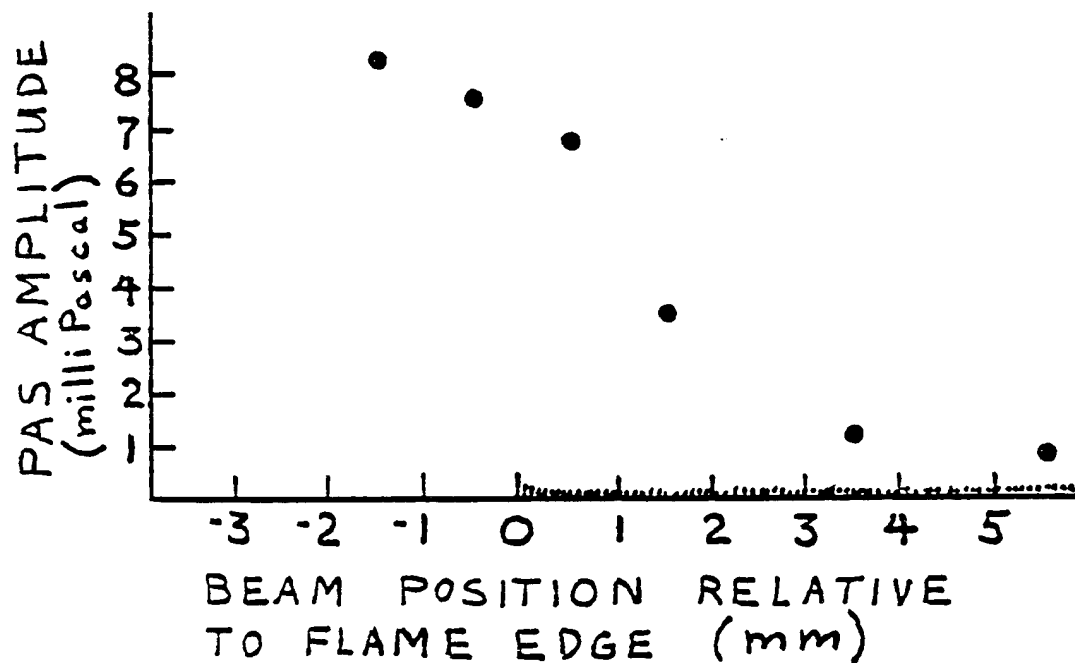


Figure 13: PAS Amplitude versus lateral beam position. The microphone position was kept fixed as the beam was moved. Zero corresponds to the beam center over the edge of the flame. The beam was 4 mm above the burner head.

as a function of the lateral position of the laser beam. These data were taken with the straight edge flame (Fig. 7) and zero in Fig. 13 corresponds to the edge of the flame.

Dependence of the photoacoustic signal on the laser power is shown in Fig. 14 indicating that the NO_2 was not saturated even at the highest powers used.

In order to obtain the density of the NO_2 molecules from the observed photoacoustic signal, one must calibrate the signal with known densities of NO_2 . To this end, we introduced several known densities of NO_2 in N_2 at atmospheric pressure into the burner (without the fuel gases O_2 and CH_4). Leaving all other conditions identical to those in Fig. 8, photoacoustic signals were recorded, and are shown in Fig. 15. A few comments concerning the signal shapes are in order at this point. The dispersion shape (dip followed by a rise) is the characteristic shape of photoacoustic signals observed in these experiments with the dip corresponding to a compression. This signal shape is extremely reproducible and is in accord with the predictions of the theory. The subsequent parts of the signal are caused primarily by photoacoustic signals generated in the other parts of the burner enclosure, and by the reflection at the burner head and the burner enclosure (cross) walls. The first peak following the first dip is affected in a significant way by reflection from the burner head only when the laser beam is very close to the burner head as shown in Fig. 16. The signal of interest (first dip), however, is not affected by any of the reflections, i.e., all of the reflections are time resolved from the main signal. In Fig. 17 we have plotted the photoacoustic signal strength (taken to be baseline to the tip of the first dip) against NO_2 density, and we find it to be linear as expected. In order to deduce the number density of NO_2 molecules in the flame using the calibration curve generated at room

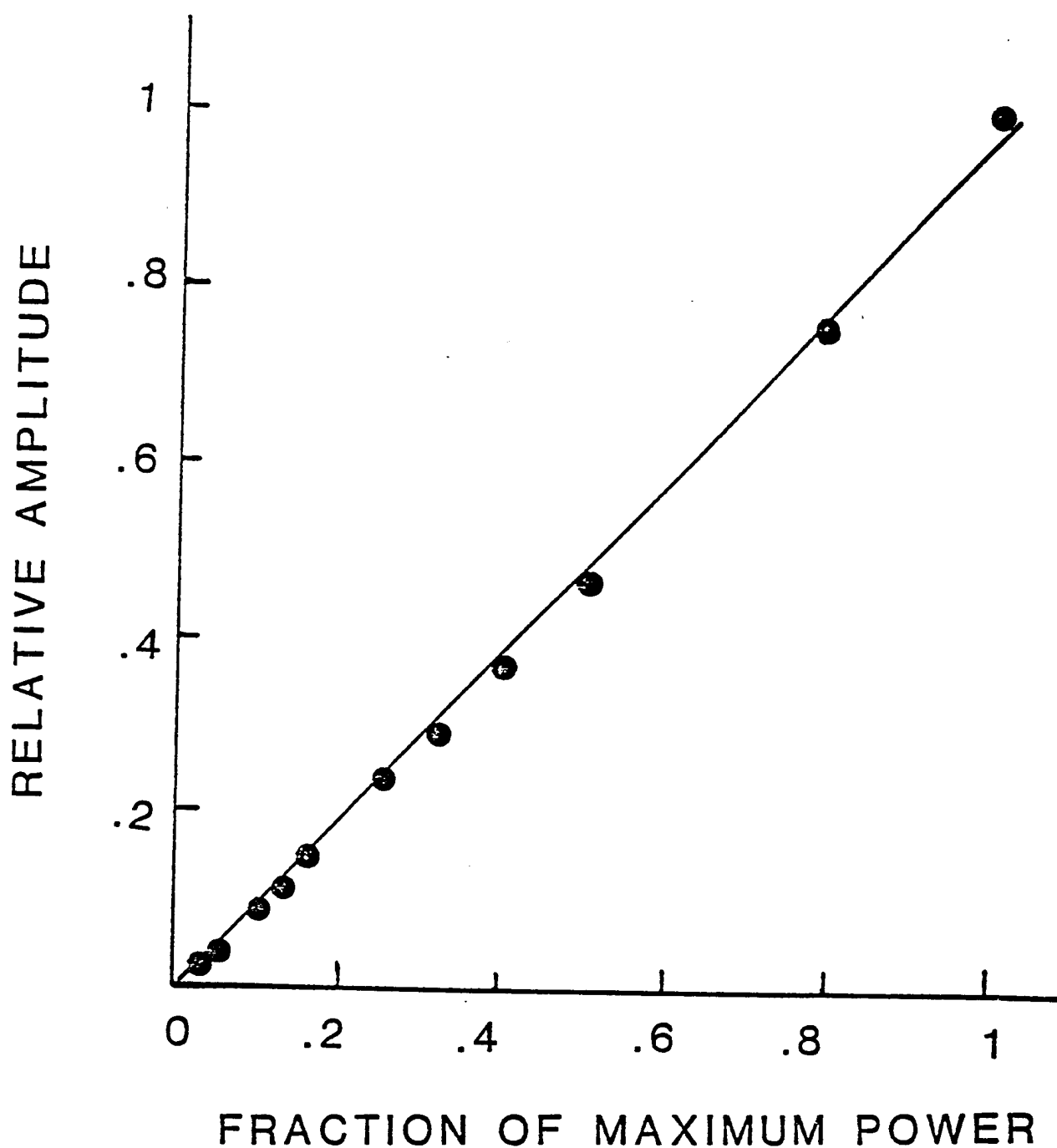


Figure 14. Dependence of the photoacoustic signal on laser power. The maximum laser energy was 6 mJ per pulse, corresponding to $8 \times 10^5 \text{ W/cm}^2$.

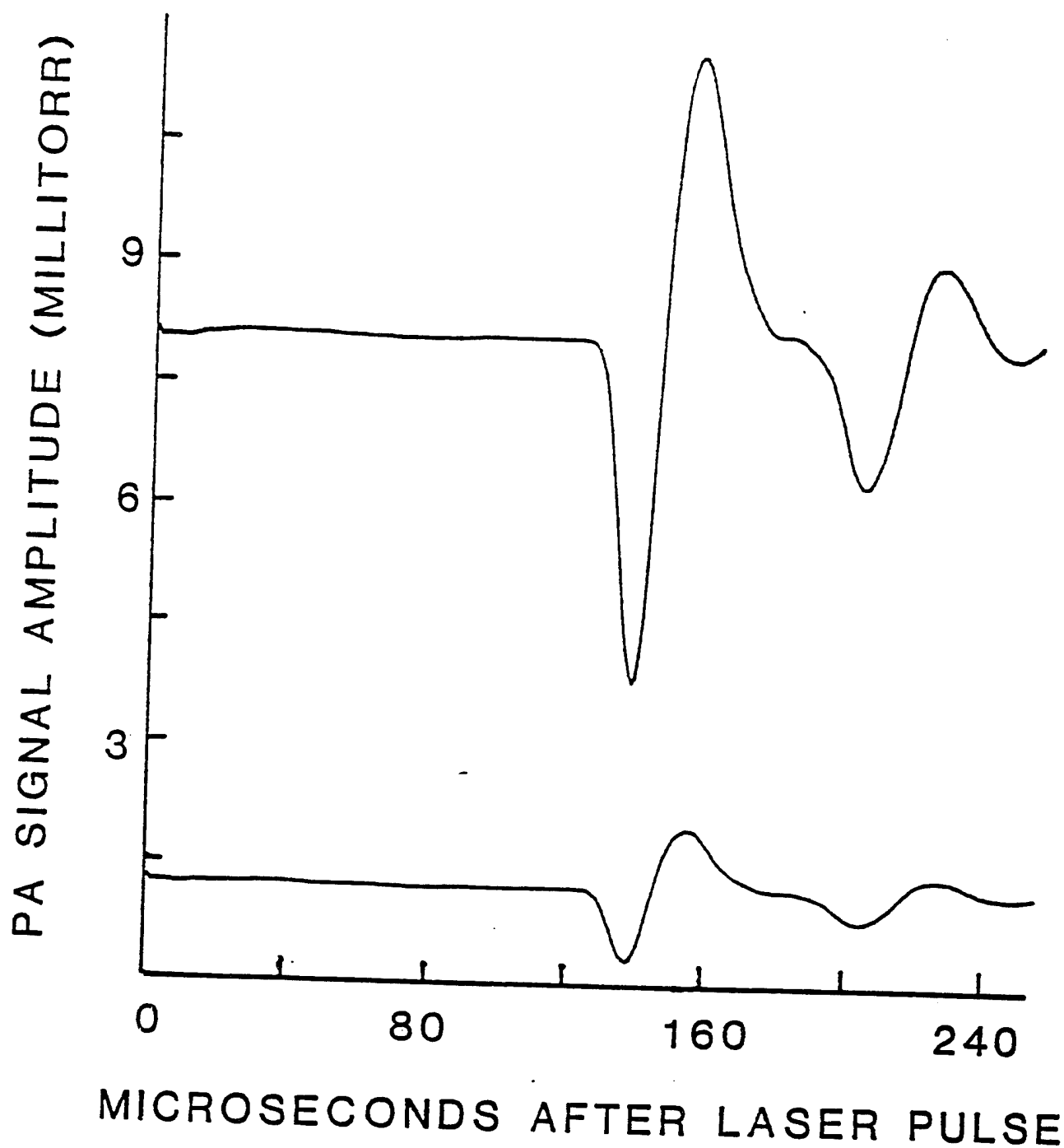


Figure 15. Photoacoustic signals for NO₂ in N₂ with no flame. Upper and lower curves correspond to 43 ppm and 8.6 ppm, respectively. Signal averaged over 1000 pulses. Laser wavelength was 4900 Å with 9 mJ/pulse energy.

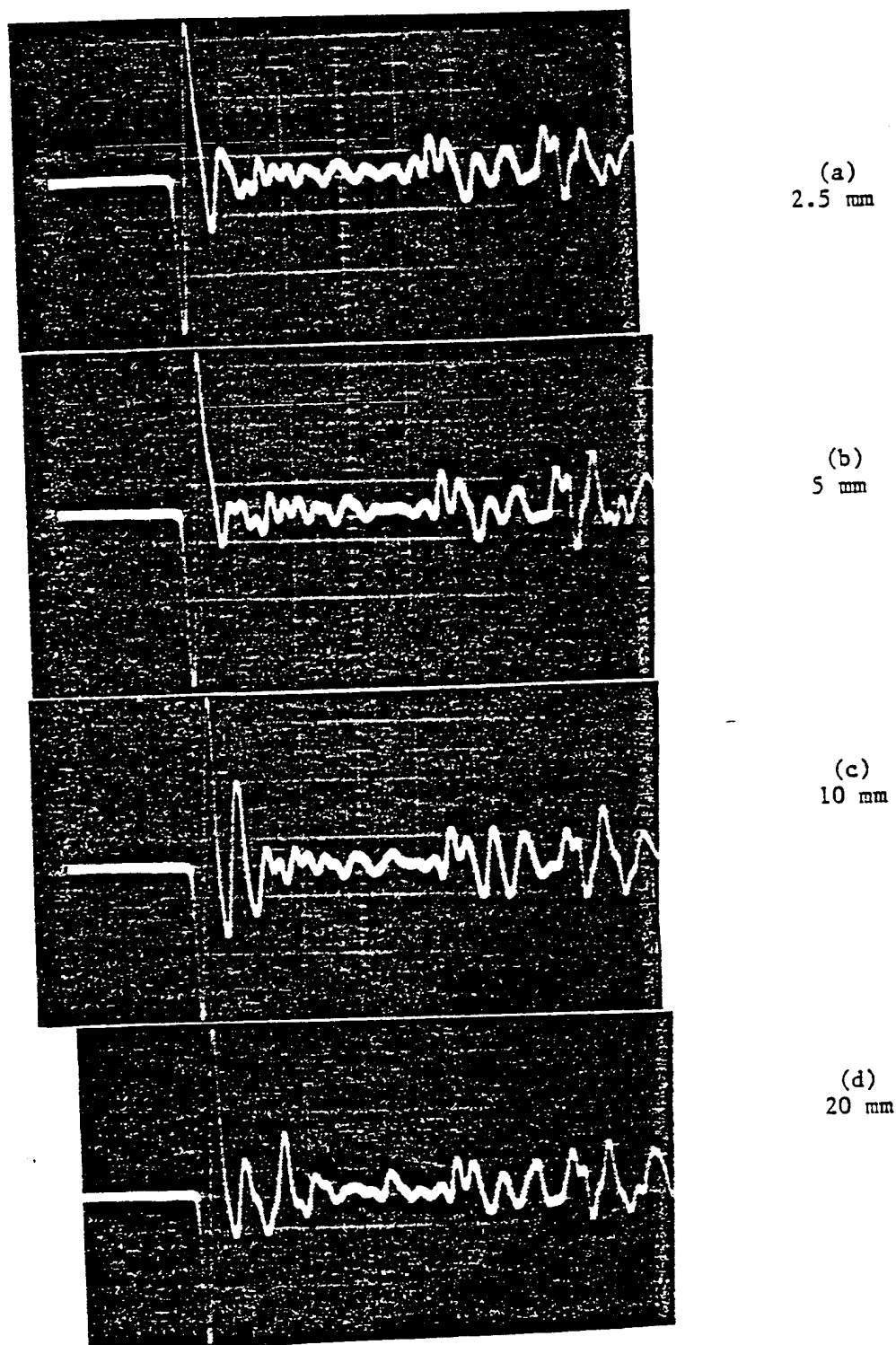


Figure 16: Effect of beam height above burner on peaks following initial dip. Beam height is listed by figures. The horizontal scale is 50 microseconds per division. The interference can be seen as the shoulder on the first peak and by the changing amplitude ratios between the first peak and the first dip.

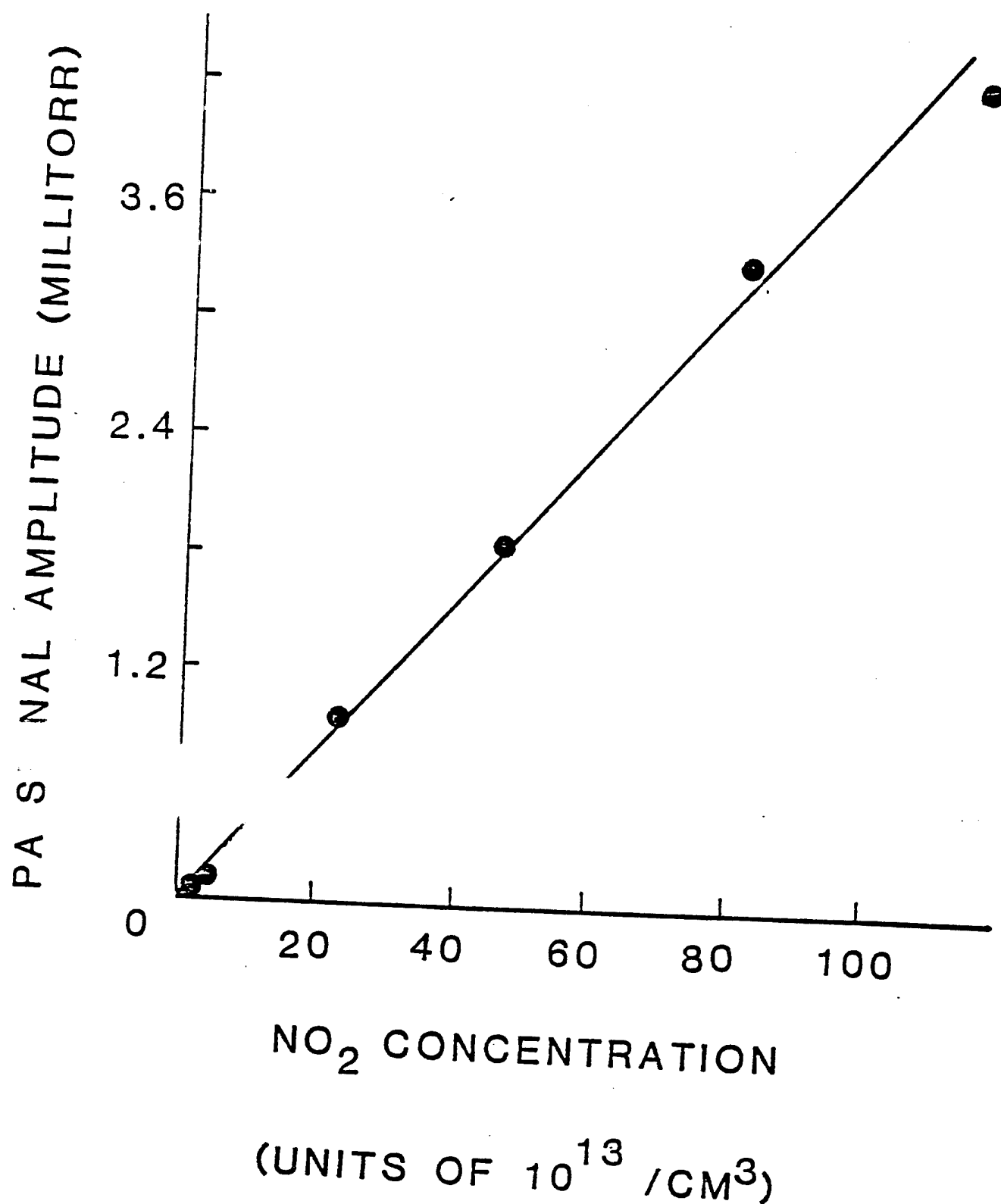


Figure 17. Photoacoustic signal amplitude plotted against the known NO₂ concentration at room temperature. Laser wavelength was 4900 Å and laser energy was 9 mJ per pulse.

temperature, three basic assumptions have to be made: (i) The photoacoustic signal is independent of the quenching rates, since the quenching rates are different in a flame than those at room temperature. It was shown in Section B that the photoacoustic signal is nearly independent of the quenching rates when they are very fast compared to the radiative rates in NO_2 . (ii) The absorption coefficient of NO_2 molecules is the same at flame temperature as it is at room temperature. Although an argument can be given that NO_2 absorption should not significantly change with temperature, the data of Figs. 9 and 10 indicate that it may be changing. Unfortunately, the absorption coefficient of NO_2 is so small that it is not easily possible to measure directly the attenuation of our laser beam in the flame. Moreover, there is no other independent and reliable method of measuring NO_2 density at such low concentrations, which in turn could be used to deduce the absorption. (iii) The signal is independent of the acoustic velocity. This assumption is not strictly justifiable, however, considering the other larger uncertainties involved in our calibration, we have disregarded this effect at this time.

Making the above assumptions, we conclude that the detection sensitivity of our technique in LD 490 dye range is about 4×10^{13} NO_2 molecules/ cm^3 on the single shot basis and about 1×10^{12} NO_2 molecules/ cm^3 for averaging over 10^3 laser pulses (for a signal to noise ratio of 3). This sensitivity may be stated in terms of the absorption coefficient as $2 \times 10^{-7} \text{ cm}^{-1}$ for averaging over 10^3 pulses.* This sensitivity is based on the observed strength of the photoacoustic signal with known NO_2 density (Fig. 17) and the observed noise in our flame (Fig. 18). Fig. 18 shows that noise, in the bandwidth in which

*Figure of 10^3 pulses has been arbitrarily chosen as a reasonable integration time in situations where temporal resolution is not terribly important. For 30 pps from a Chromatix CMX-4 dye laser, this corresponds to about 30 sec integration time.

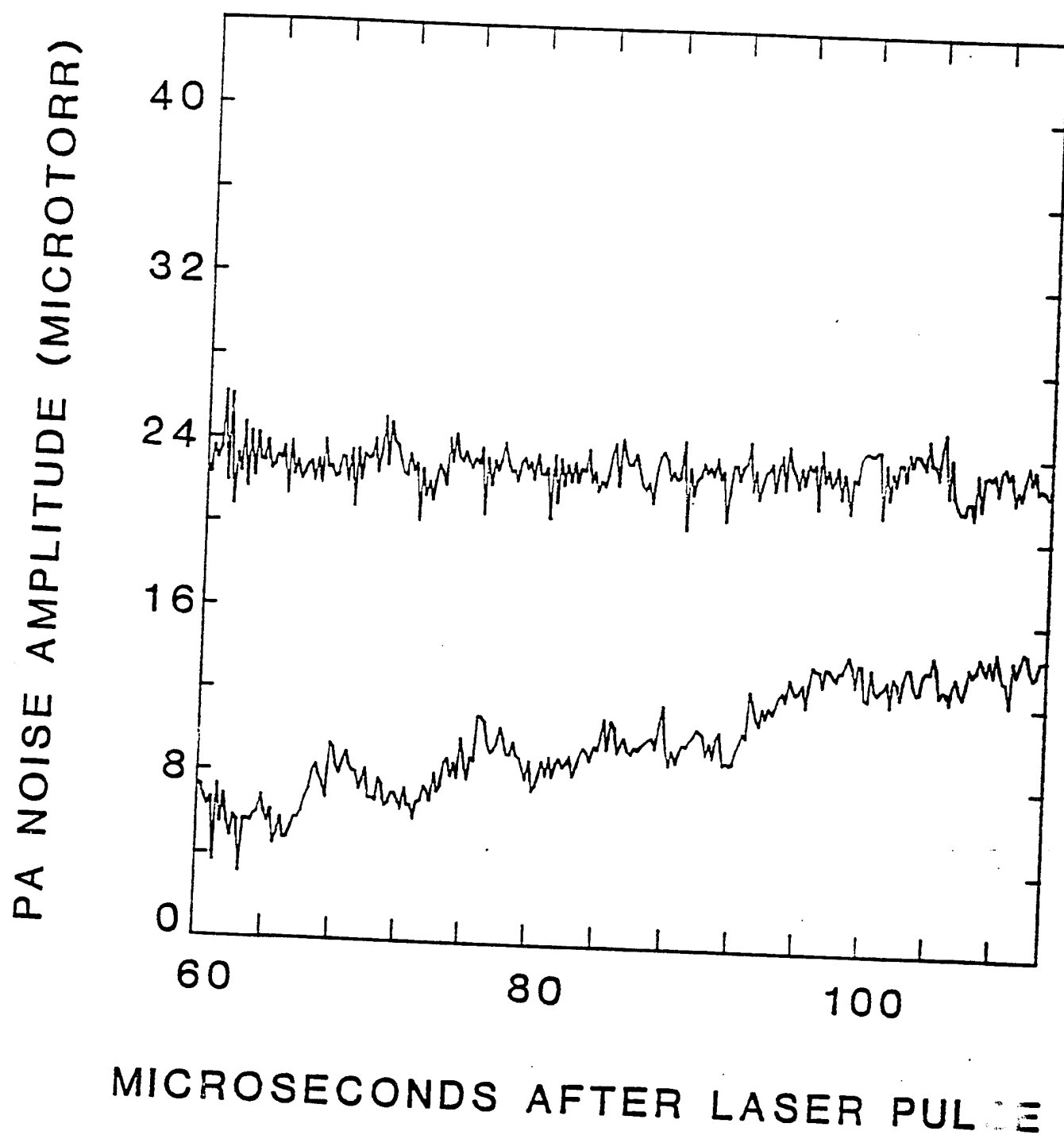


Figure 18. Comparison of the acoustic noise observed in our experiment with (lower trace) and without (upper trace) the flame. These curves were taken under conditions identical to those of Fig. 6 and represent averaging over 1000 pulses.

our pulsed detection system is sensitive, and it is not significantly worse in the flame than without the flame (ambient noise in the laboratory). From our calibration curve, we also conclude that the NO_2 density corresponding to the first dip in Fig. 8 is about $3 \times 10^{13} \text{ cm}^{-3}$ for the top curve (3 ppm assuming a temperature of 1000° K in the region of measurement). These numbers naturally are uncertain perhaps by about a factor of five due to uncertainties in the absorption coefficient of NO_2 at high temperatures.

In order to check the validity of the theoretical model of Section B, we estimate the amplitude of the photoacoustic signal corresponding to a concentration of $3 \times 10^{13} \text{ NO}_2 \text{ molecules/cm}^3$ in the flame (number corresponding to the top curve in Fig. 8, as obtained by the calibration curve). At 4900 \AA the absorption coefficient of NO_2 has been measured¹³ to be $\sim 5 \times 10^{-3} \text{ cm}^{-1} \text{ Torr}^{-1}$. Due to the complexity of the NO_2 spectrum it is very difficult to estimate the effect of pressure and Doppler broadening in a flame on the absorption coefficient. Moreover, the NO_2 molecules are distributed differently over vibration-rotation states at flame temperature than at room temperature. We will, however, assume that the absorption coefficient in the flame is still $5 \times 10^{-3} \text{ cm}^{-1} \text{ Torr}^{-1}$. This point has already been discussed in connection with calibration above. Assuming laser operating with 9 mJ of energy per pulse, we expect an absorption of about $1.5 \times 10^{-7} \text{ J}$ by the NO_2 molecules in the laser beam path (about 5 cm long). Here we have used Eqs(2), (AIII.4), and assumed "white-light" excitation ($\gamma = 1$). The heat capacity of 1 mm dia x 5 cm long region at flame temperature is about $8 \times 10^{-6} \text{ J K}^{-1}$, which gives a temperature rise of about $2 \times 10^{-2} \text{ K}$. This corresponds to a pressure rise of about 7 mTorr in irradiated region [using Eq(4)], or a pressure rise of about one mTorr at the microphone. The observed pressure rise in the top curve of Fig. 8 is 0.1 mTorr. The order of magnitude agreement is not bad considering

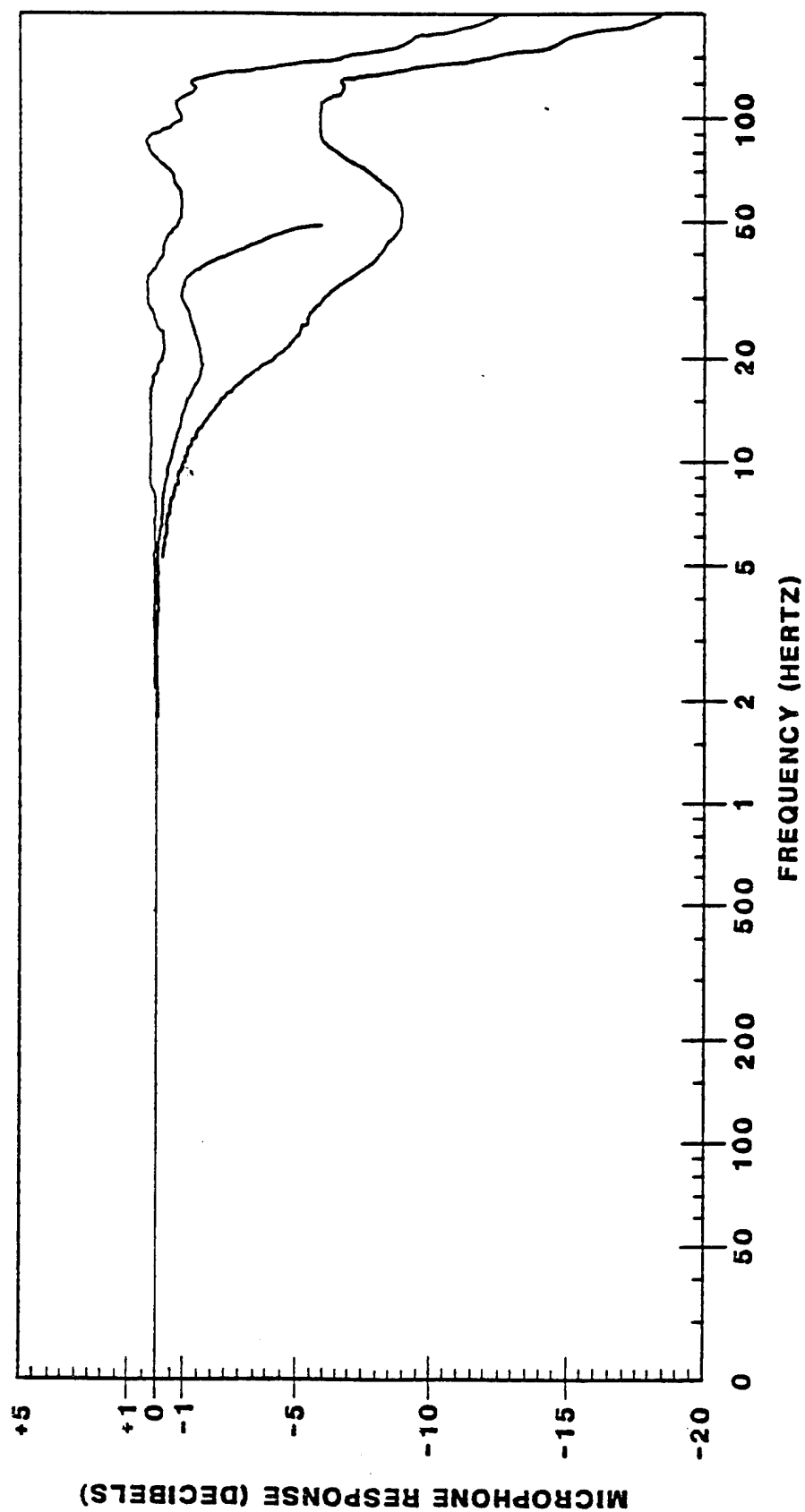


Figure 19. Frequency response of the B&K Model 4135 microphone. The upper curve is the open circuit free-field characteristic, valid for microphone cartridge without protecting grid. Sound waves perpendicular to the diaphragm. The lower curve is the open circuit pressure response with electrostatic actuator. The middle curve is the open circuit random incidence response. Protection grid included.

the crudeness of our model and the fact that we do not know the absolute calibration of our microphone for response to a few microsecond wide pulse. Response of our microphone is 0.5 mV/mTorr for frequencies up to about 50 KHz and falls off thereafter as shown in Fig. 19. We have assumed the above response in our computations, but in all probability it is considerably less than this for our photoacoustic pulse of ~ 1 μ sec duration.

As it was pointed out earlier, OH molecules, due to their well resolved and well understood spectrum, are better suited for a quantitative investigation. Investigation of the photoacoustic effect in OH is described next.

(iii) Experiments with OH

A typical photoacoustic signal taken with the B & K microphone due to OH molecules is shown in Fig. 20. The laser was tuned to the $Q_1(2)$ transition¹⁴ of the $A^2\Sigma^+(v' = 0) - X^2\Pi(v'' = 0)$ band at 3080 Å (see Figs. 21 and 22). The laser beam was collimated to about 1 mm in diameter and passed through the luminous region of the methane-air flame. Microphone to laser beam distance was about 4 cm. the laser energy was 19 μ J per pulse. The curve shown in Fig. 20 represents signal averaging over 500 pulses. Signal averaging was not necessary to observe the signal; it was used to average out the pulse-to-pulse fluctuations in the laser power. Zero of the abscissa corresponds to the instant of laser firing. The photoacoustic signal corresponds to a compression wave followed by a rarefaction wave, in agreement with the theoretical predictions. The structure subsequent to the signal, is not noise, but it is the reflections of the acoustic wave from the burner structure and the enclosure. Similar data for $Q_2(6)$, $Q_2(5)$, and $Q_1(5)$ lines is shown in Figs. 23-25.

In order to show noise explicitly, we show in Fig. 26 a typical single shot signal taken directly with an oscilloscope. The oscilloscope was

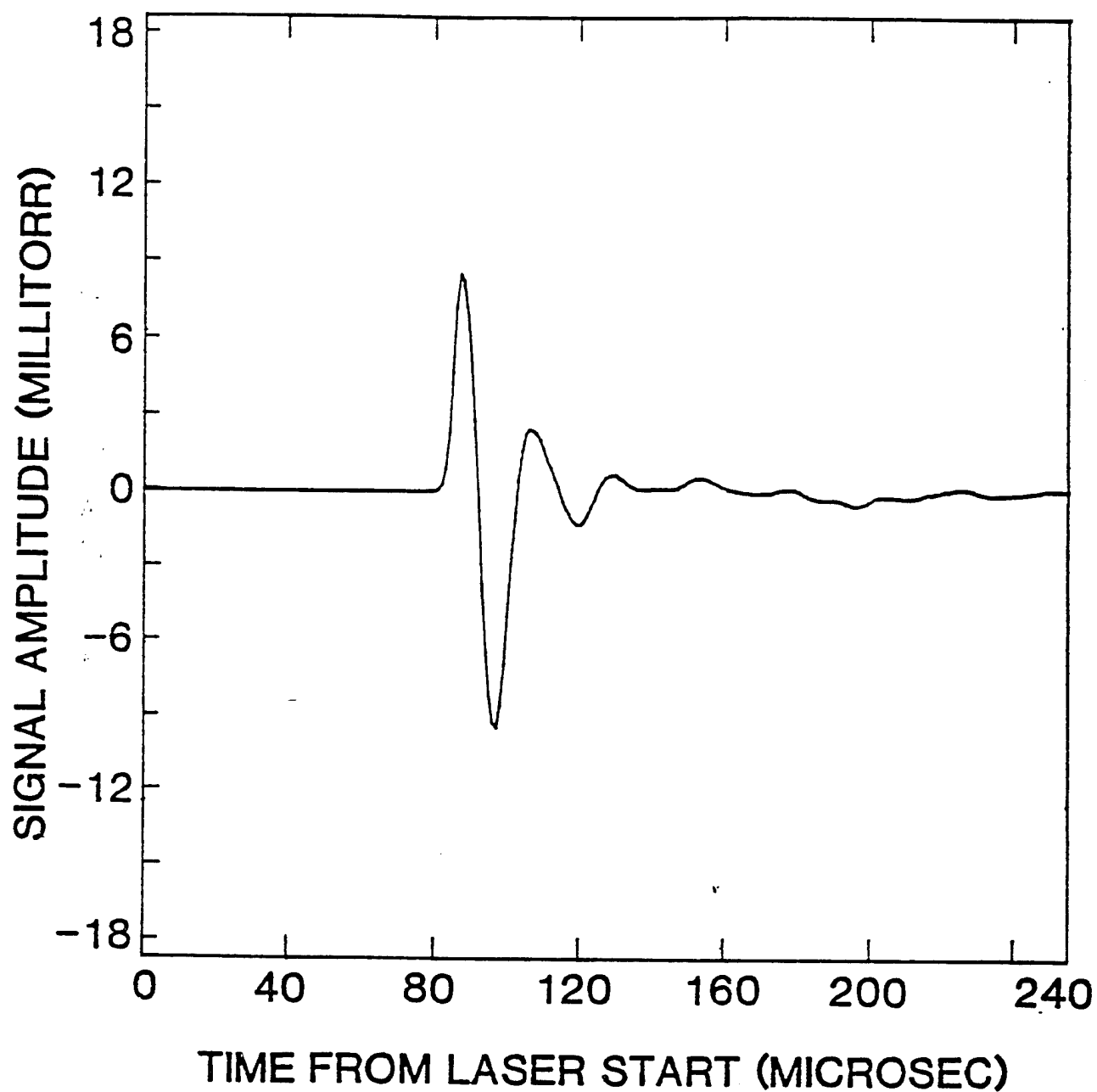


Figure 20. Photoacoustic signal from the OH molecules in methane-air flat-flame burner. Laser was tuned to the $Q_1(2)$ transition of the $A^2\Sigma^+(v' = 0) - X^2\Pi(v'' = 0)$ band at 3080 Å.

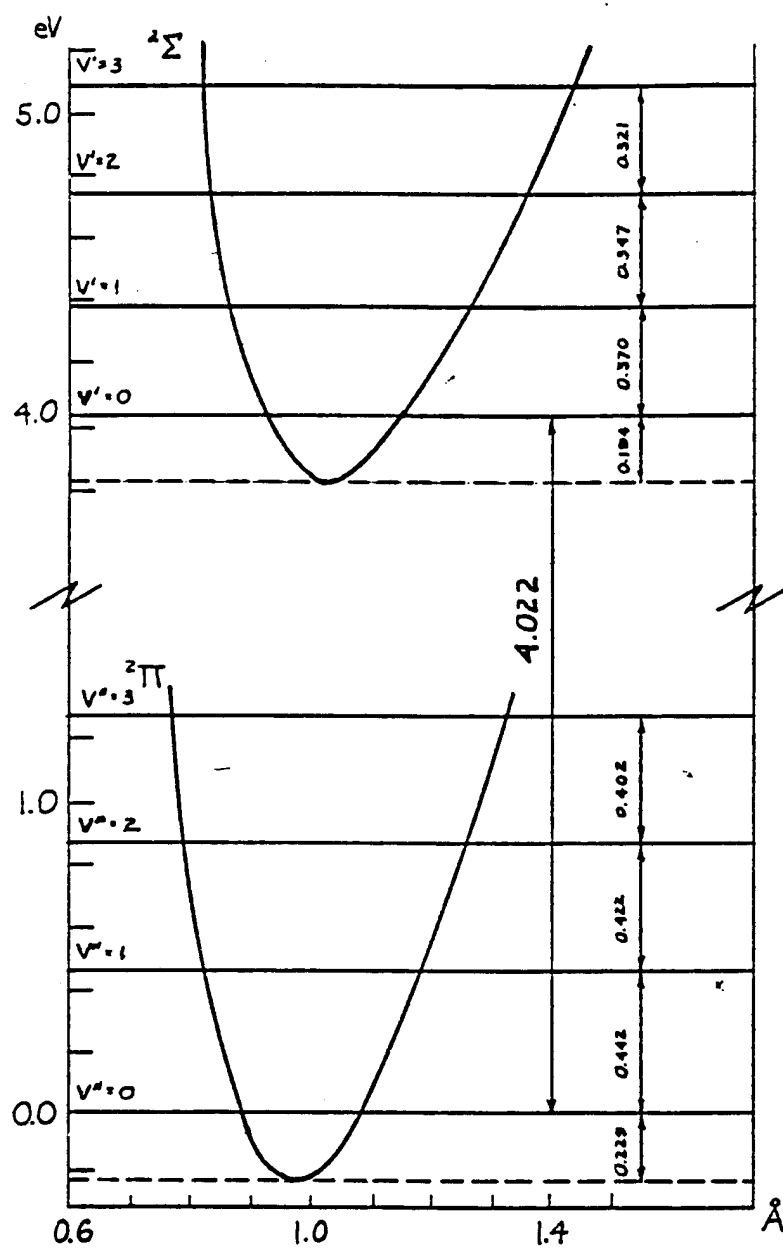


Figure 21. Electronic-vibrational structure of the OH molecule.

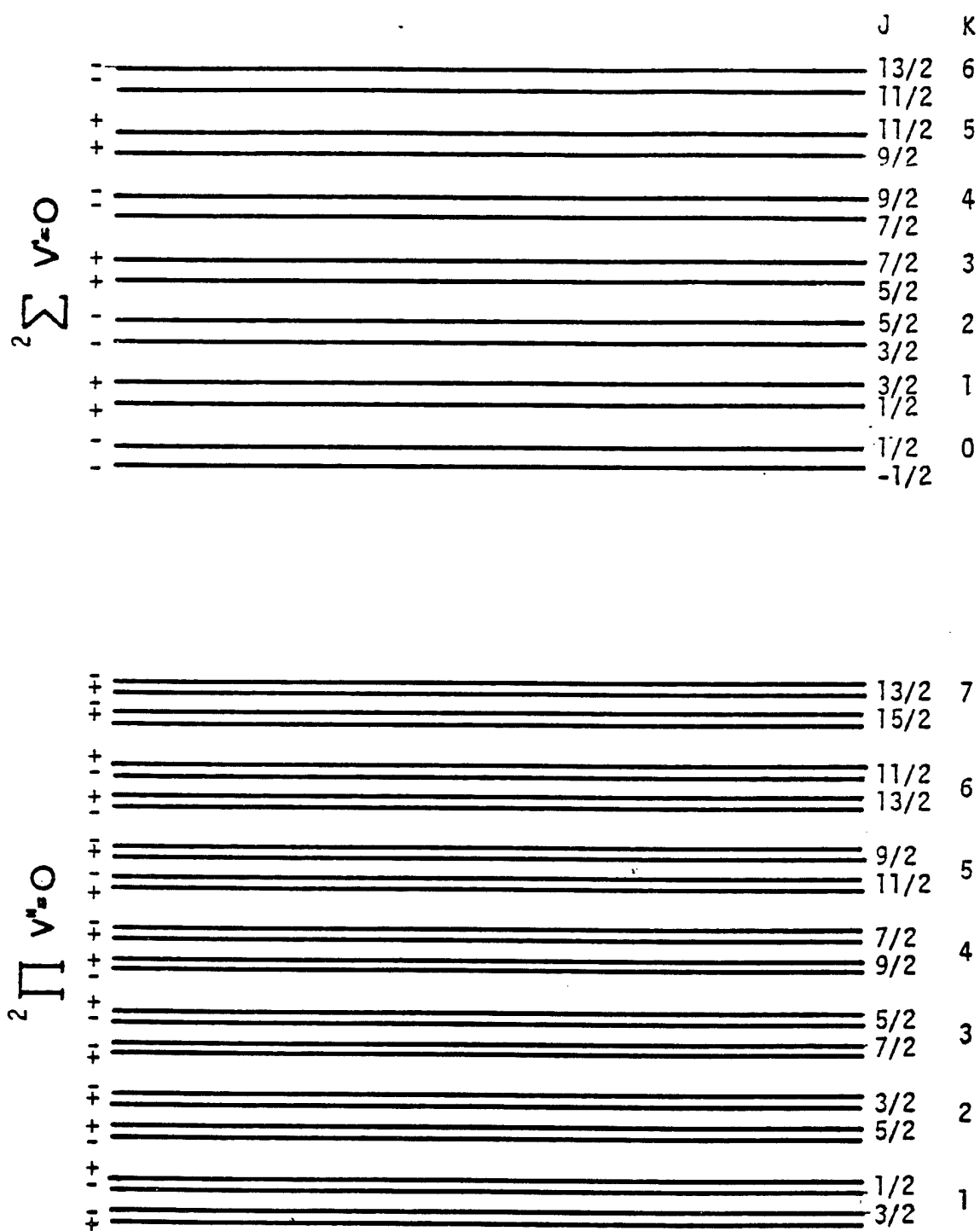


Figure 22. Vibrational-rotational structure of the OH molecule.

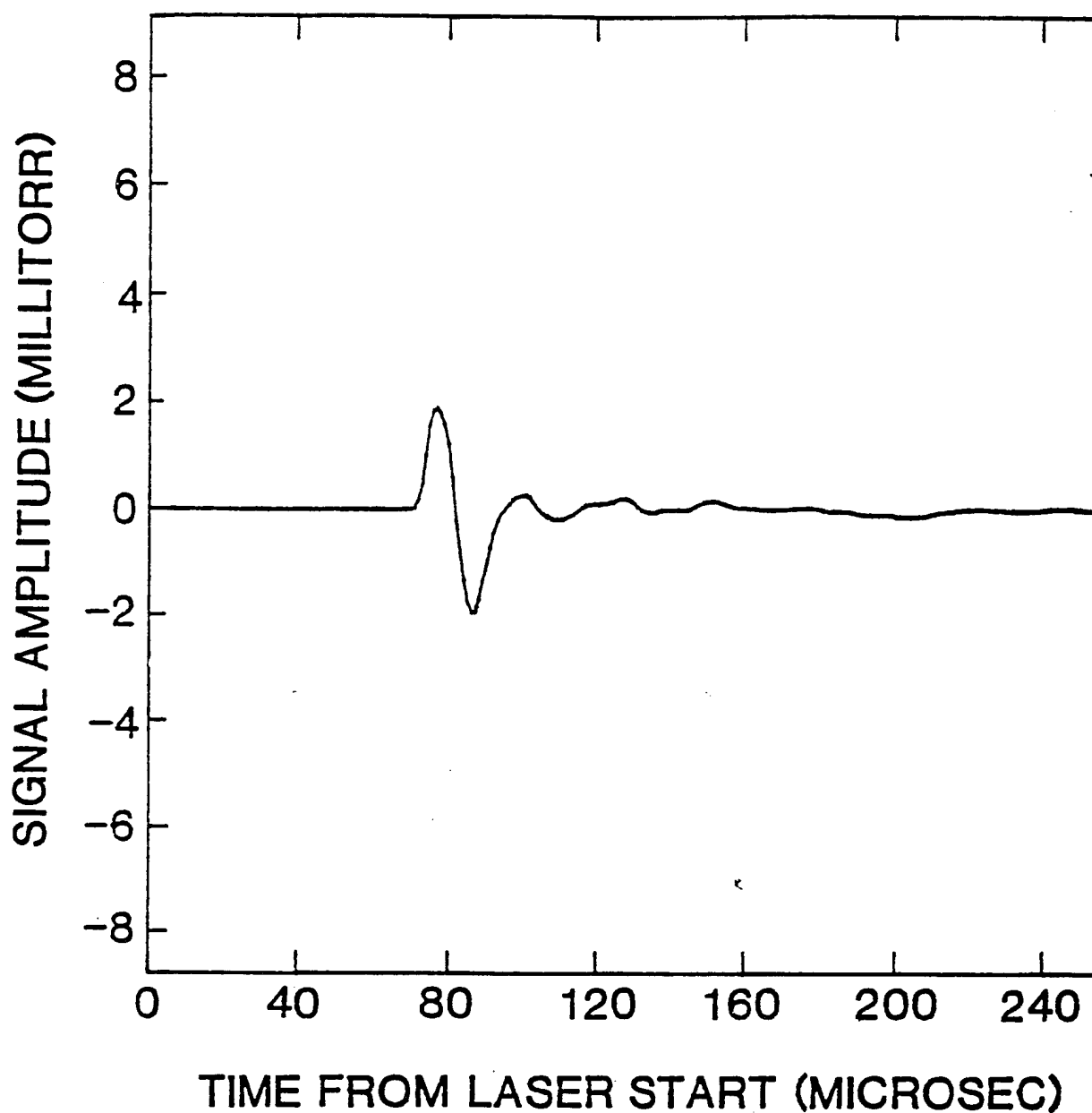


Figure 23. Photoacoustic signal from the OH molecules in methane-air flame. Laser was tuned to the $Q_2(6)$ transition at 3092.8 \AA . Laser energy was about 20 \mu J per pulse and the signal was integrated over 500 pulses.

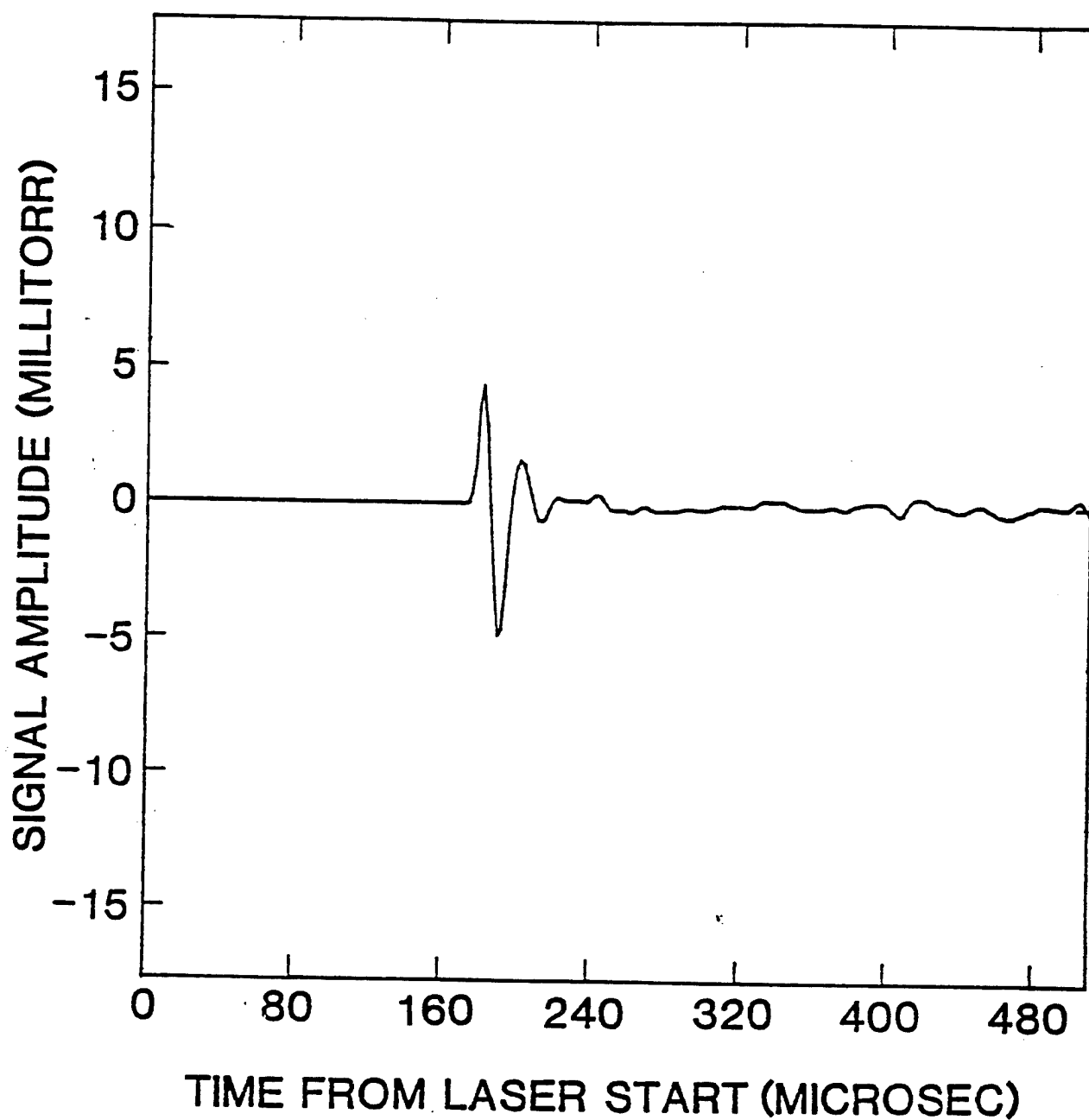


Figure 24. Photoacoustic signal from the OH molecules in methane-air flame. Laser was tuned to the $Q_2(5)$ transition at 3091.4 \AA . Laser energy was about 25 \mu J per pulse and the signal was integrated over 500 pulses.

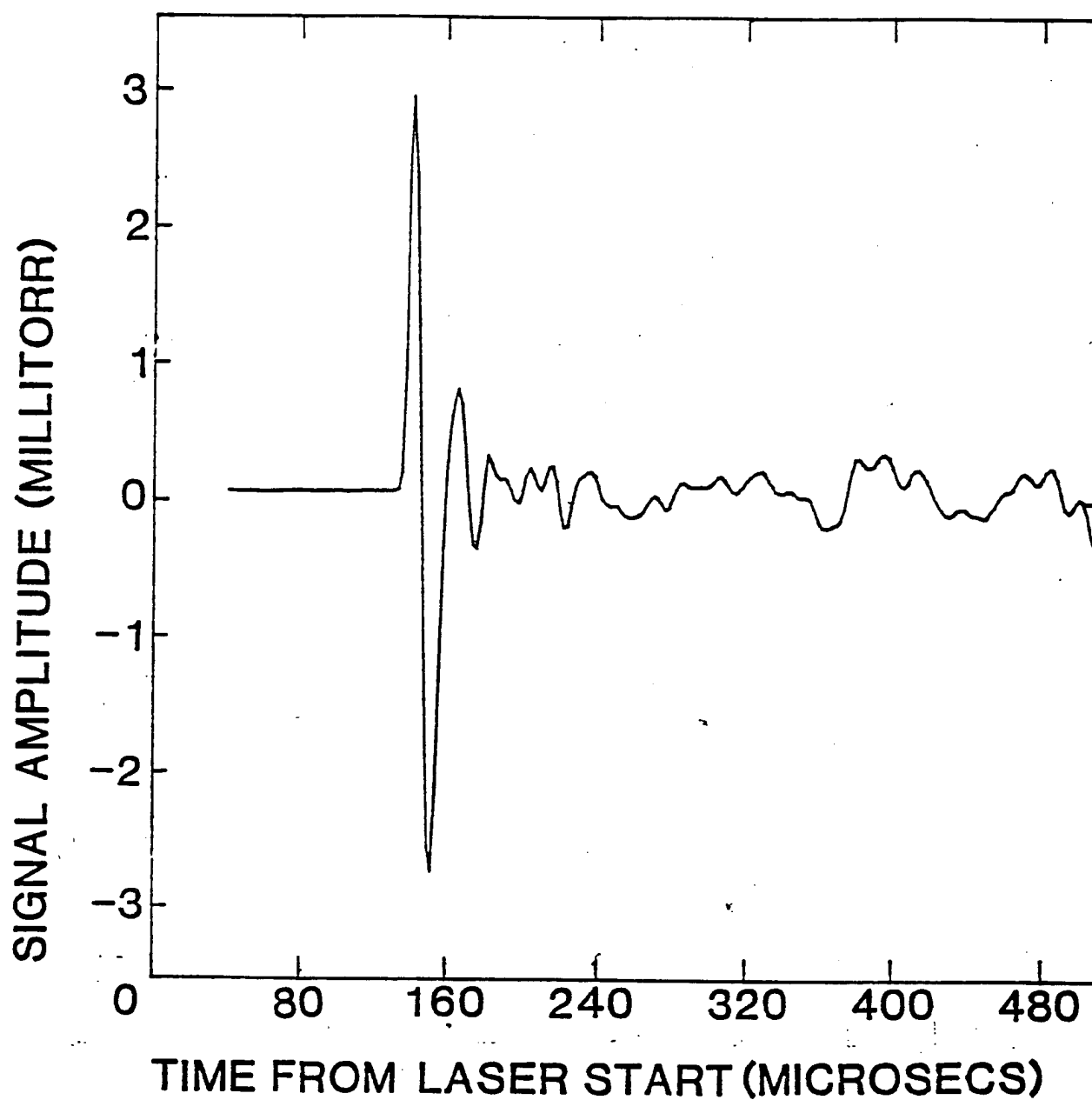


Figure 25. Photoacoustic signal from the OH molecules in methane-air flame. Laser was tuned on the $Q_1(5)$ transition at 3085.2 \AA . Laser energy was 50 \mu J per pulse and the signal was integrated over 500 pulses.

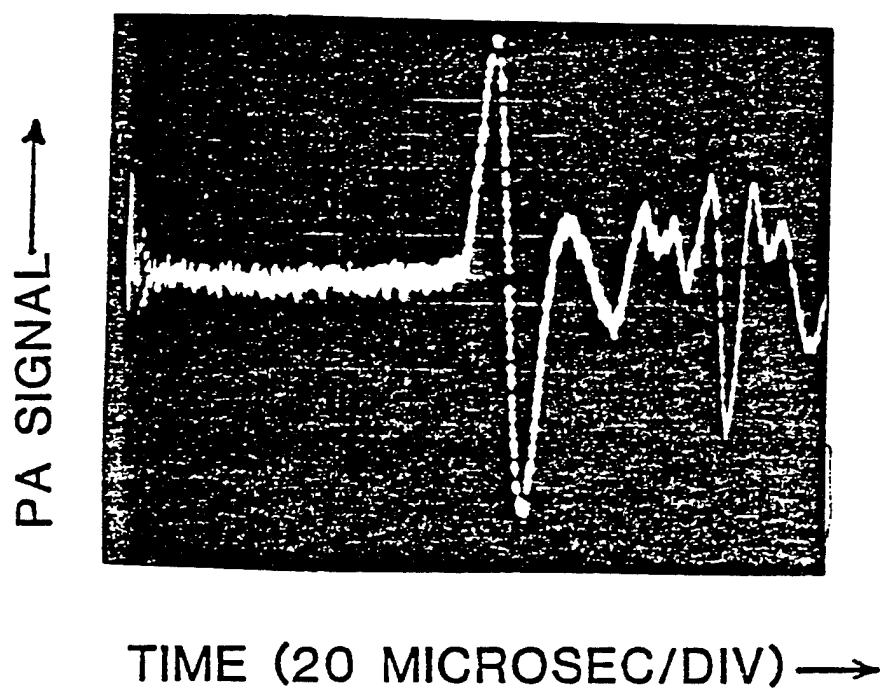


Figure 26. Single shot oscilloscope trace of the OH photoacoustic signal in the methane-air flame. Laser energy was 15 μ J per pulse and was tuned to the $Q_2(6)$ transition at 3092.8 \AA .

triggered by a pulse from the laser flashlamp circuitry, had a sweep rate of 20 $\mu\text{sec/div}$, and a single shot photograph was taken of the screen. All the conditions for this curve were similar to those of Fig. 20, except that the laser power was 15 μJ and it was tuned to the $Q_2(6)$ transition of the $A^2\Sigma^+(v' = 0) - X^2\Pi(v'' = 0)$ band at 3092.8 \AA . It is worth pointing out that this curve was taken with an old dye solution when the laser power was degraded far below the optimum available from chromatix CMX-4 dye laser.

In order to test the theoretical model given in Sec. B, we determined the density of OH molecules in our flame by absorption measurements. Laser power transmitted through the flame was measured by a Scientech Model 36200-2 calorimeter. Transmitted laser power was measured when the laser was tuned on to the desired OH absorption line as well as when it was tuned off the line. The background from the flame was minimized by a UV transmitting Schott UG-11 filter in front of the calorimeter. The remaining background was measured and taken into account.

Absorption on the $Q_1(2)$ line of OH at 3080 \AA in our flame was measured to be 40%. The pathlength in the flame was about 6 cm. This corresponds to an average absorption coefficient $\bar{\alpha}$ of 8.5 m^{-1} (see Appendix III). Using Eq. AIII.4 and the Einstein B-coefficients given by Dimpfl and Kinsey,¹⁵ we deduce the number of OH molecules in the $K = 2$ rotational state to be $6.6 \times 10^{13} \text{ cm}^{-3}$. Assuming a flame temperature of 1300° K, this corresponds to a total number density of OH molecules of approximately $3 \times 10^{15} \text{ cm}^{-3}$. We have taken absorption measurements (as well as photoacoustic measurements) on four different lines $Q_1(2)$, $Q_2(6)$, $Q_2(5)$, and $Q_1(5)$ giving, respectively, 40%, 57%, 49%, and 31% absorption. these measurements give consistent values of the OH number density.

We have calculated the size of the photoacoustic signal expected for the $Q_1(2)$ line using $N_0 = 6.6 \times 10^{13} \text{ cm}^{-3}$ in Eqs(5) and (15). Both equations yield a pressure pulse of amplitude 32 mTorr. This is to be compared with the observed signal of 8.6 mTorr (Fig. 20). Here we have assumed that the microphone sensitivity is 0.5 mV/mTorr. The agreement between the theoretical model and the experiment is quite good considering that we do not know the sensitivity of the microphone for response to a 1 μsec acoustic pulse, and the simplifying assumptions made in our theoretical model. The microphone response is 0.5 mV/mTorr up to about 50 KHz and declines for higher frequencies. The response of the microphone for a one μsec pulse could not be obtained from the manufacturer.

The theoretical model [Eq(13)] predicts that the compression wave and the rarefaction waves should be separated in time by roughly the width of the laser pulse. This conclusion, of course, is true when the laser pulse length is long compared to the acoustic travel time in the irradiated region (i.e. $\tau_p > r/v_a$). Our photoacoustic data taken with B & K microphone shows the time separation to be about 8-10 μsec . As mentioned previously, the microphone response is flat up to about 50 KHz and declines for higher frequencies. It appeared therefore that the observed width was the instrumental response time of the microphone. Therefore we have observed the photoacoustic signal with a Panametrics pzt transducer, with specified bandwidth of 2.25 MHz. The observed signal for the $Q_2(6)$ line of OH at 3092.8 \AA is shown by the lower trace in Fig. 27. For comparison, the signal observed by the microphone is shown by the upper trace. These signals were taken with only about 6 μJ of laser energy per pulse, and represent a result of integration over 100 pulses for the upper curve and over 1000 pulses for the lower curve. The microphone (pzt transducer) distance from the laser was about 7 cm. The signal-to-noise ratio is much poorer with the

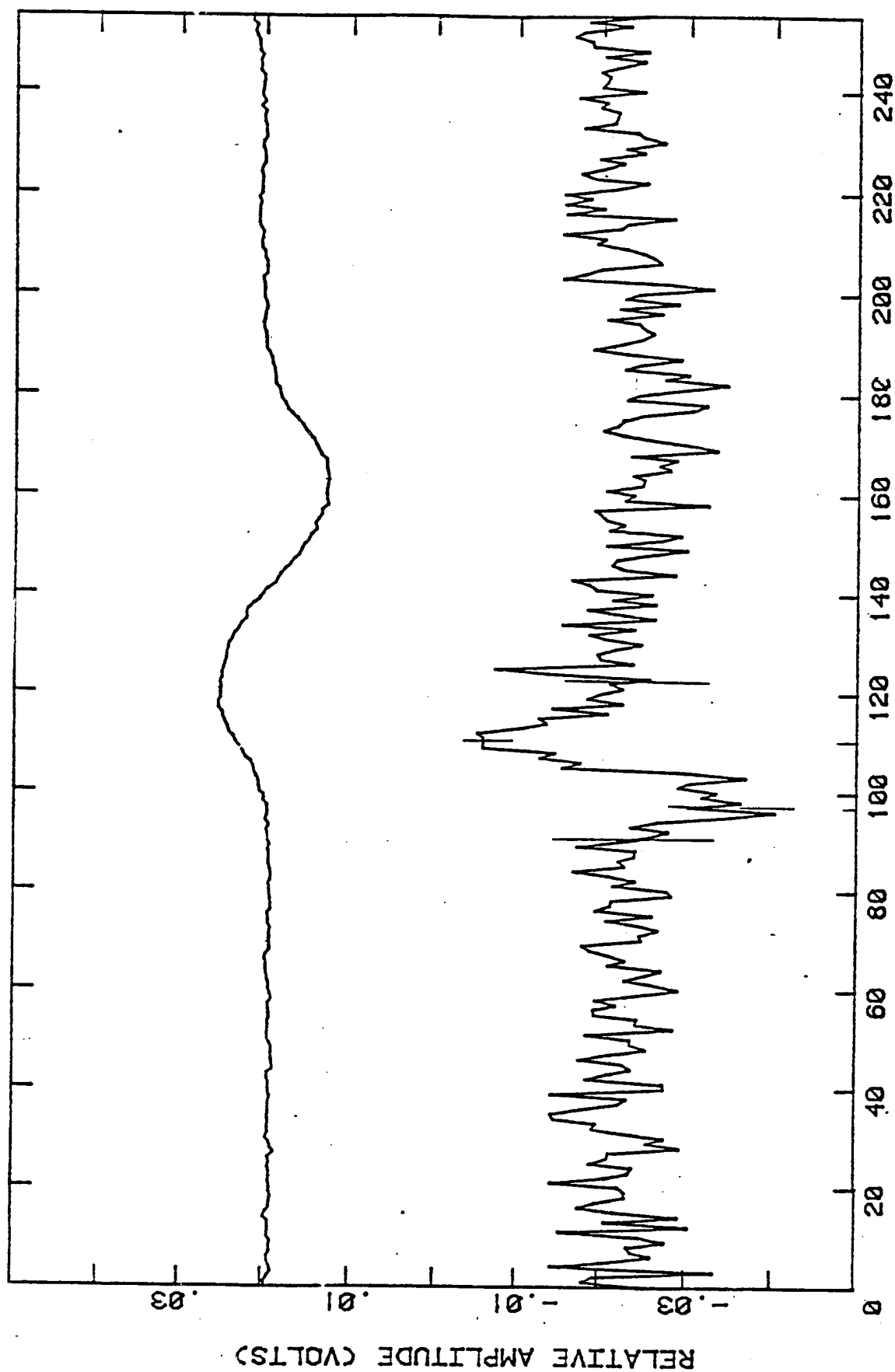


Figure 27. Comparison of the photoacoustic signals due to OH in methane-air flame with a B & K microphone (upper curve) and a Panametrics pzt transducer (lower curve).

pzt transducer, as expected, due to the poor acoustic impedance match between the flame gases and the pzt crystal. However, the lower curve is clearly much narrower than the upper one. We measure the separation between compression peak and the rarefaction peak to be about 2.6 μsec for the lower curve. This is somewhat longer than the laser pulse strength (manufacturer's specification: $\sim 1 \mu\text{sec}$ FWHM). We expect this to be the case since assumptions leading to Eq(13) [$\tau_p > r/v_a$] are not strictly satisfied in our case. In our case $\tau_p \approx r/v_a$ and the UV laser beam cross section is oblong in shape. Nevertheless, Fig. 27 confirms the essential correctness of our theoretical model.

For a cylindrical pressure wavefront the intensity decreases with distance as $1/R$ whereas the pressure amplitude decreases as $1/R^{1/2}$ as given by Eqs(5) and (15). This is of course true only if no modification of the cylindrical wavefront by the flame boundary takes place. With our experimental arrangement using a flat flame burner (Fig. 1), due to changes in the acoustic velocity at the round flame boundary, the flame interface acts like a cylindrical diverging lens with its axis vertical. Fig. 28 shows the OH photoacoustic signals for various microphone distances (R) from the laser irradiated region (for round flame interface as in Fig. 1). In Fig. 29 we have plotted the amplitude of the photoacoustic signal as a function of R . The data points are fitted to a function

$$P_o(R) = \frac{C}{R^n} \quad (19)$$

using a log-log plot. n is found to be approximately -1.4. In order to test our model, similar data was taken with the straight edge flame (Fig. 7). In this case, as the acoustic wave passes through the straight flame boundary, the wave-front retains cylindrical shape. Fig. 30 shows a plot of the photoacoustic signal as a function of the microphone laser beam distance R , for

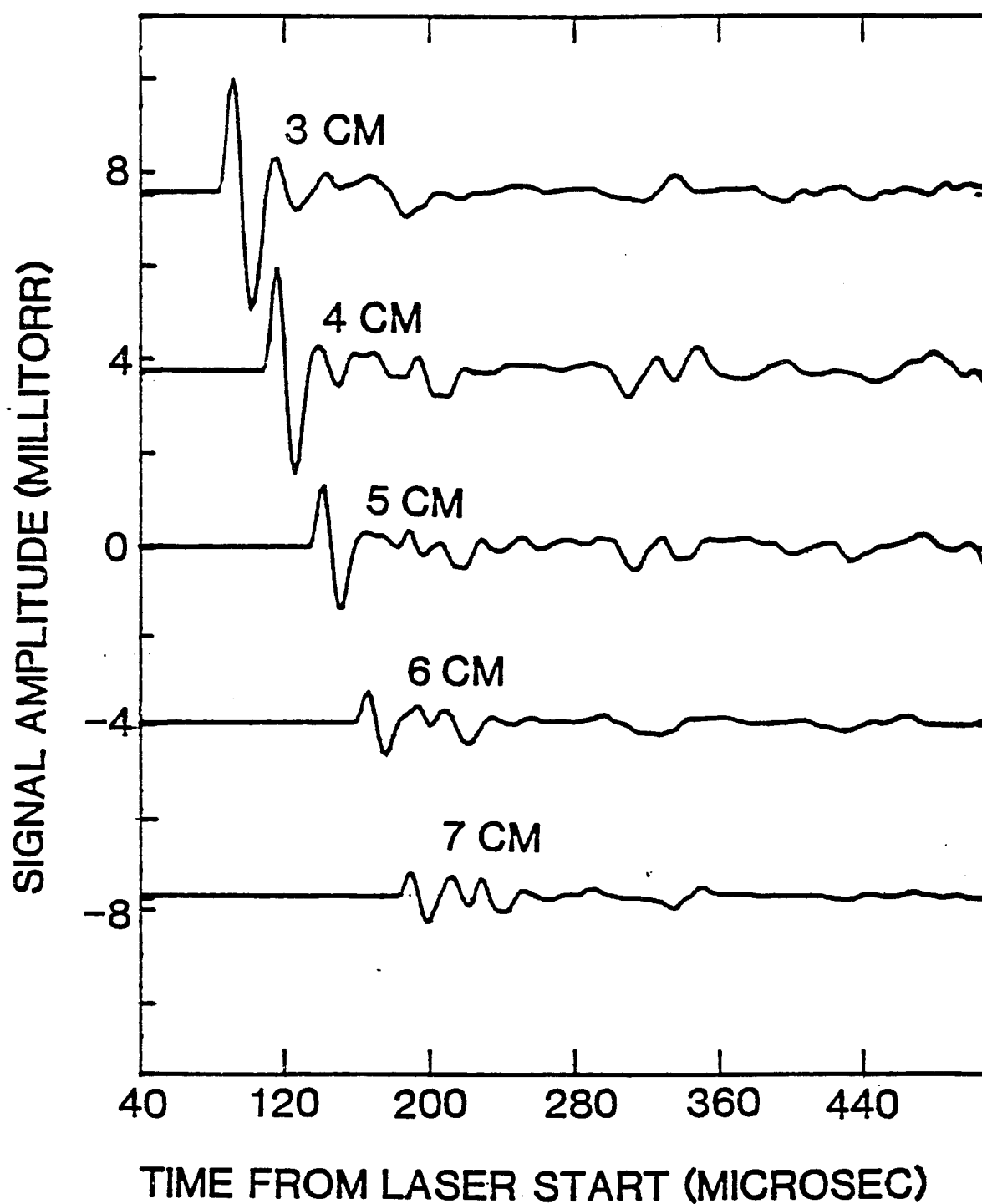


Figure 28. OH photoacoustic signal for various laser microphone distances. These distances are marked on the curves.

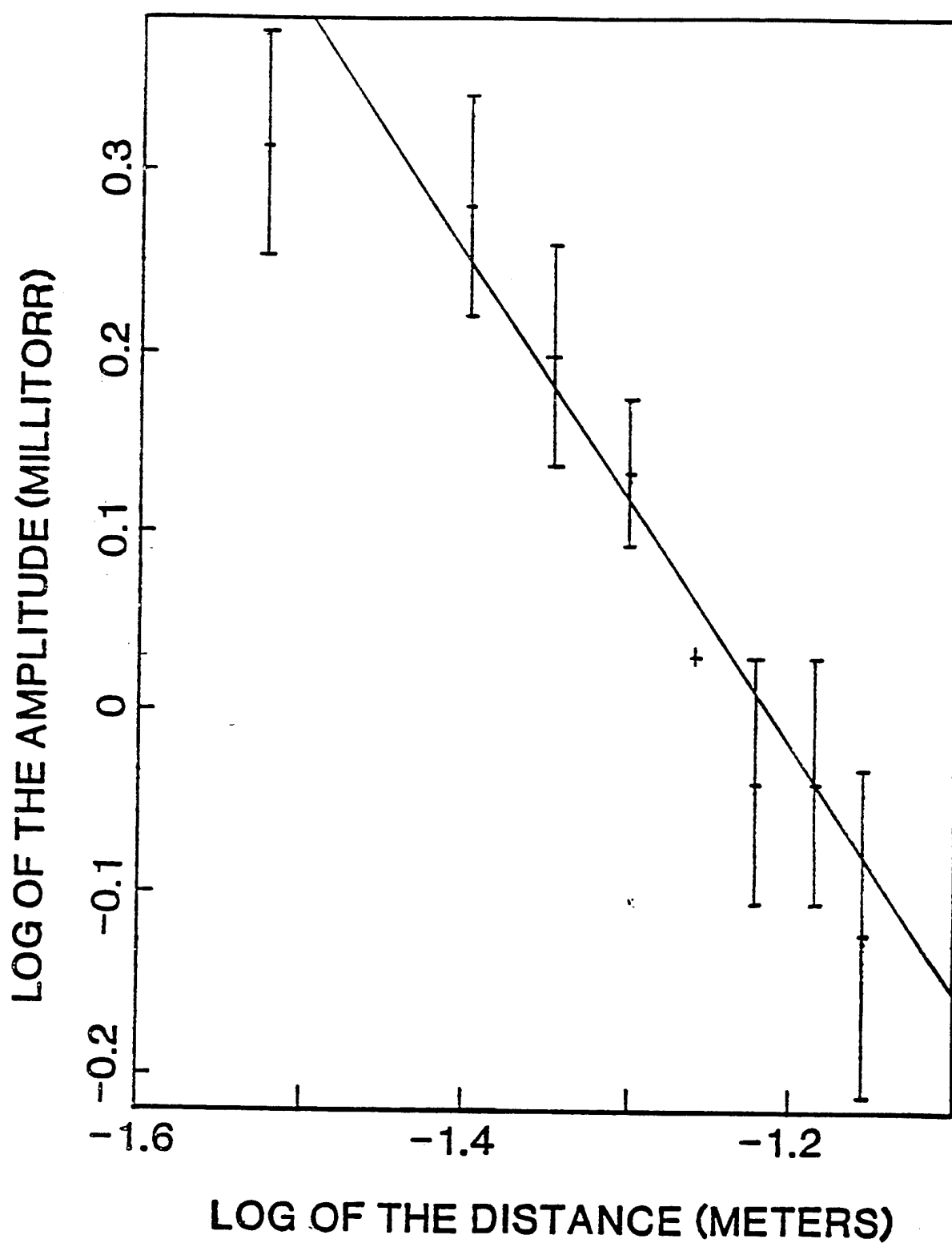


Figure 29. Photoacoustic signal amplitude plotted against the laser-microphone distance for round flame interface.

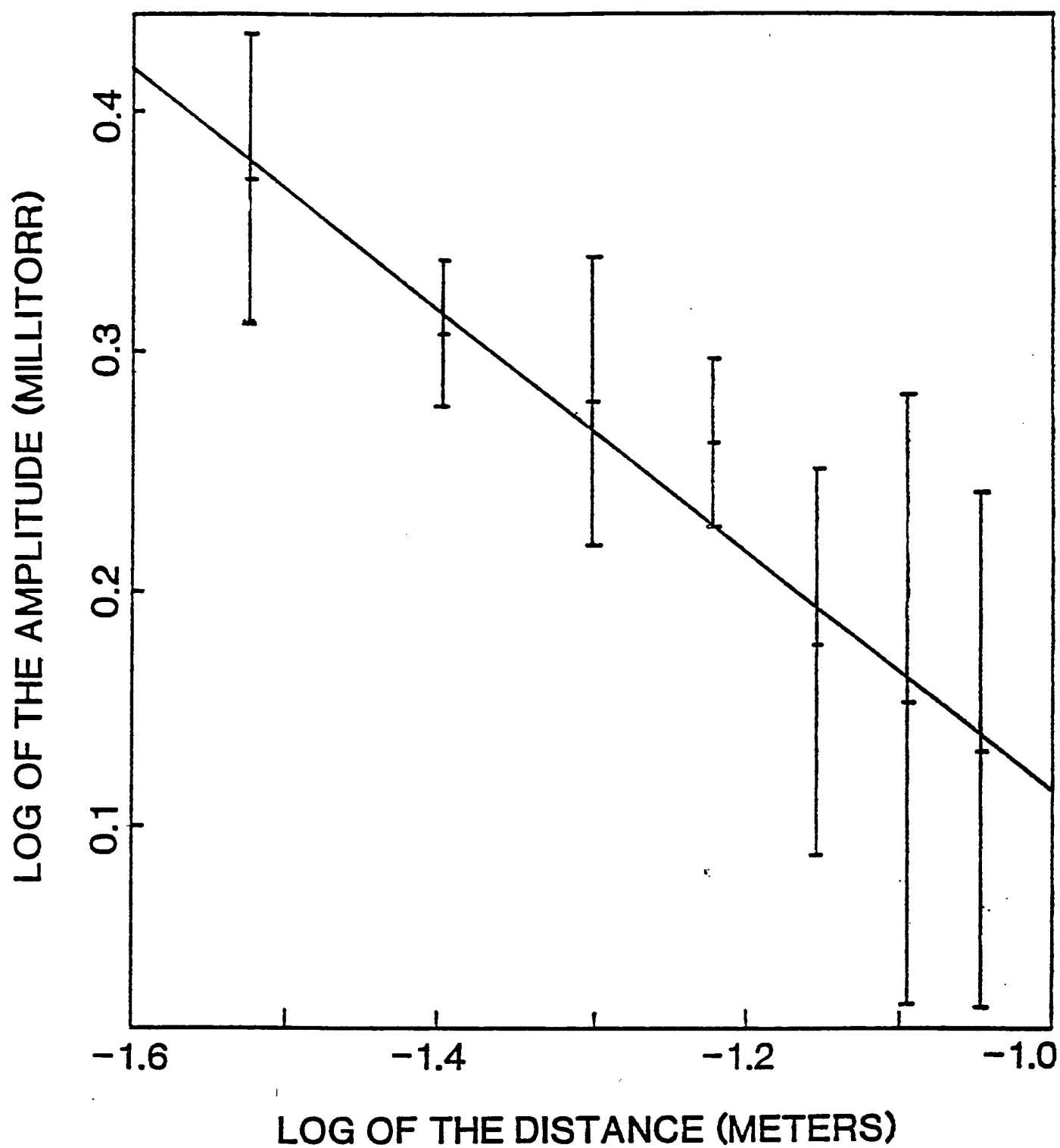


Figure 30. Photoacoustic amplitude plotted against the laser-microphone distance for the straight edge flame.

straight interface. In this case the exponent n is determined to be approximately -0.5, in agreement with our theoretical model.

Fig. 31 shows the concentration of OH molecules in the ground electronic state as a function of the distance above the burner head, as measured photoacoustically. The flame was operated under oxygen rich conditions. These results compare favorably with those of Cattolica.¹⁶

(iv) Two-photon experiments

Two-photon photoacoustic experiments were attempted by tuning the laser to 6174.3 \AA . This corresponds to a transition from the $x^2_{\pi}, v'' = 0, f_1(6)$ state to the $A^2_{\Sigma^+}, v' = 0, F_1(6)$ state of OH molecules.¹⁴ Both of these states have the same parity. Note that $F'_1(6) - F_1(6)$ is the single-photon $Q_1(6)$ transition. Unfortunately the two-photon OH photoacoustic signal was masked by the much larger single-photon NO_2 photoacoustic signal. Therefore we tried to substitute He for N_2 in our flame. We were unable to stabilize the flame with helium. After much effort, we were able to stabilize the flame with argon, i.e., we used a mixture of CH_4 , O_2 , and Ar. No NO_2 is produced with this fuel mixture. We attempted to observe the OH two-photon signal by integrating the signal over 4,000 laser pulses. No signal was observed. Our estimates based on Eq(18) and the assumptions mentioned in Sec. B indicate that a signal-to-noise ratio of 8 should have been observed. In this estimate, we assumed that the OH density in our flame with Ar was the same as that with N_2 .

These results indicate that the actual signal-to-noise ratio was at least a factor of four or five smaller than that given by our estimates. This is not totally surprising in view of the crude approximations made in the evaluation of Eq(18).

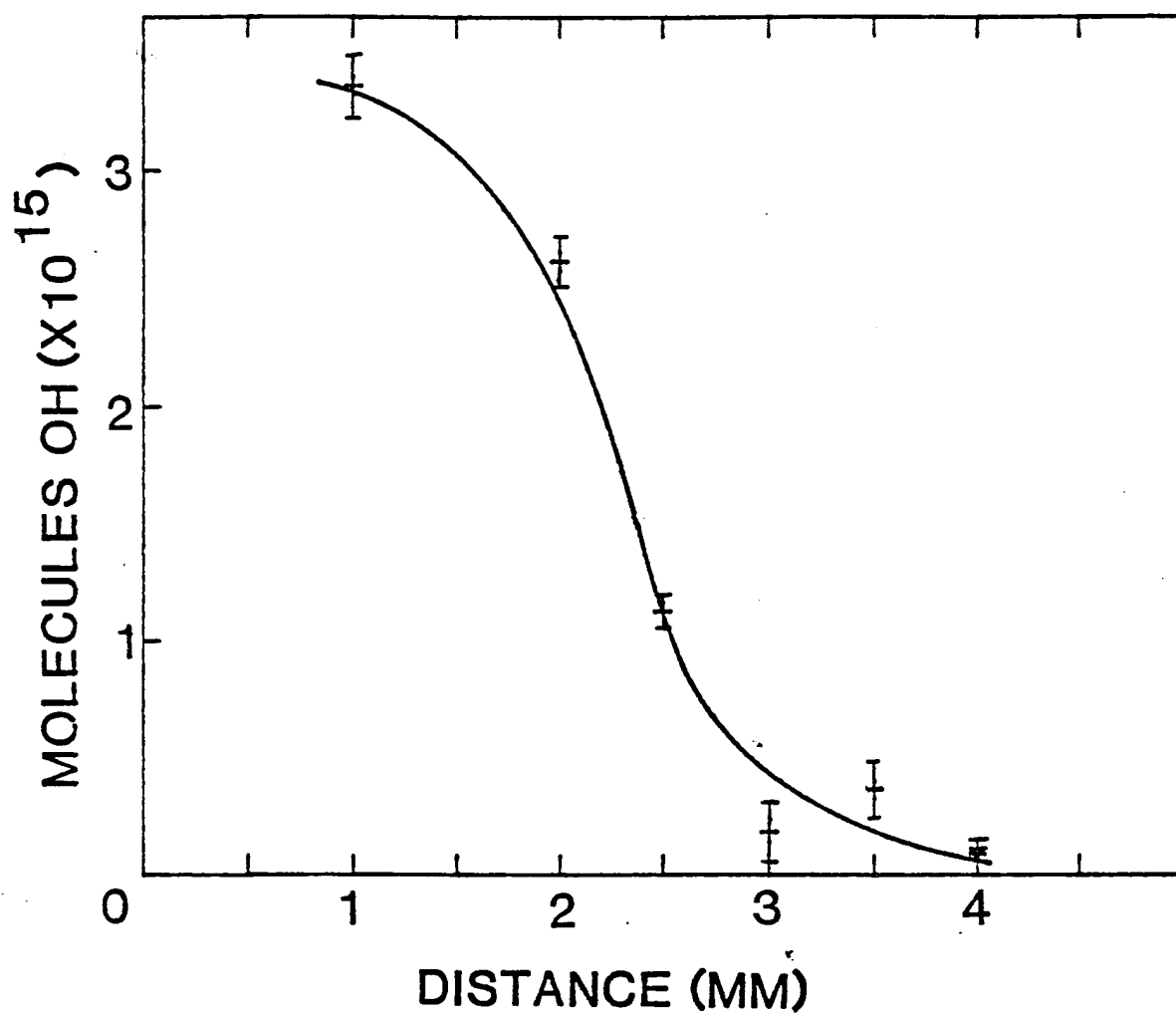


Figure 31. Density of OH molecules as a function of the distance above the burner head, as measured photoacoustically.

E. Conclusions

As it was pointed out in the Introduction, several optical combustion diagnostic techniques are currently under investigation at various laboratories. Coherent anti-Stokes Raman scattering (CARS) is generally believed to be a very successful diagnostic technique. Its sensitivity, however, limits its use to specie concentrations greater than about 0.1%.³ Fluorescence techniques generally have a higher sensitivity and are suitable for minority species concentration measurements. The fluorescence techniques, however, are beset by the problem of quenching collisions. In an atmospheric pressure flame, the quenching rates are generally faster than the radiative rates, and generally the effect of quenching collisions cannot be quantitatively accounted for. Several schemes have been devised to either eliminate or account for the effect of quenching collisions. Muller et al.¹⁷ have shown that if an extremely narrow bandwidth detection is used, then to a good approximation the collision quenching summation varies in a simple manner from flame to flame and can be accounted for. In another scheme,^{18,19} an atomic or molecular transition is saturated by an intense laser pulse which is then abruptly cut off. From the decay of the fluorescence after the laser pulse is over, both the quenching rate and the number density of molecules of interest is deduced. In the presence of high quenching rates, the decay is very fast requiring fast electronics. In yet another scheme, the saturated fluorescence technique,^{20,21} the effect of quenching is made negligible by making the absorption and stimulated emission rate faster than the quenching rate using a very intense laser. It should be noted that fluorescence techniques are by no means the only techniques suitable for minority species concentration measurements. For example, optogalvanic spectroscopy,²² where laser excitation of an atomic (or molecular) state is used to change the ion concentration in a flame, may be used. These

changes can be detected by observing the changes in electrical conductivity of the flame. Of all the techniques suitable for minority species concentration measurements mentioned above, saturated fluorescence has been extensively investigated as a combustion diagnostic technique and is generally believed to be the most successful technique. Therefore, in the following we will limit the comparison of the photoacoustic technique to the saturated fluorescence technique.

The basic idea behind saturated fluorescence technique is to use such high laser powers that stimulation emission rate from the upper level becomes much larger than the quenching rate.^{20,21} Under these circumstances the effect of quenching collisions on the steady state upper level population may be ignored. Temporal resolution is achieved by using a pulsed laser and spatial resolution is achieved by focusing the laser beam down in a small volume and by the use of suitable detection optics. Baronavski and McDonald²³ have shown that it is not necessary to fully saturate a transition. Both the quenching rate and the specie concentration can be derived from the slope of the saturation curve, even under partial saturation conditions. Extensive work both theoretical^{20, 21,24-26} and experimental^{23,27-29} has been performed on the development of this technique. One of the major limitations of this technique is that it requires very high intensities of tunable laser radiation. Many molecules of combustion interest have their resonance transitions in the ultra-violet or vacuum ultra-violet, which makes the application of this technique very difficult. A good example of this is NO molecule where it is estimated³⁰ that $4 \times 10^8 \text{ W/cm}^2 \text{ cm}^{-1}$ of laser intensity is required at 2260 \AA . On the other hand, the photoacoustic technique requires less laser power since the transition is not required to be saturated. Moreover, in saturated fluorescence one needs large laser intensities regardless of the concentration of molecules being

measured, while in the photoacoustic technique larger concentrations of molecules requires correspondingly smaller laser power. In other words, one may trade off laser power for sensitivity. Also, multiphoton ionization and dissociation would be more of a severe problem in saturated fluorescence than in photoacoustic technique. It should be noted that the use of Baronavski and McDonald's technique of partial saturation²³ results in a significant loss of temporal resolution. Moreover, radiative decay rates must be known for saturated fluorescence to be useful, on the other hand, in photoacoustic technique one does not need a precise knowledge of the radiative rates as long as they are slower than quenching rates. The sensitivity of the photoacoustic technique is limited by the acoustic noise in the flame while that of the saturated fluorescence is limited by the optical background of the luminous flame, laser scattering background, etc. We have shown, however, that in the detection bandwidth, our flame does not contribute appreciable noise above the ambient noise in a typical laboratory environment. This is the primary reason for high sensitivity of the photoacoustic technique.

Finally, we must compare the sensitivity of the two techniques. We have determined that the sensitivity of the photoacoustic technique is about 2×10^{-9} J of laser energy absorbed per cm of path length for averaging over 1000 pulses. This corresponds to a sensitivity of about 4×10^{13} NO_2 molecules/ cm^3 single shot or about 10^{12} NO_2 molecules/ cm^3 for integration over 1000 pulses (~ 30 secs). This also corresponds to a detection sensitivity of about 4×10^{12} OH molecules/ cm^3 single shot or about 1×10^{11} OH molecules/ cm^3 for integration over 1000 pulses. The sensitivity quoted above is, of course, without spatial resolution.

We conclude that the photoacoustic technique has an excellent potential of proving to be a very useful technique for minority species concentration

measurements. The technique as applied to a flame, is still in its infancy and still more work needs to be done in order to obtain accurate measurements.

F. References

1. P. W. Schreiber, R. Gupta, and W. B. Roh, in Laser Spectroscopy--Applications and Techniques (Editor, Howard Schlossberg, Proceedings of the Society of Photo-Optical Instrumentation Engineers, Washington, 1978).
2. A. C. Eckbreth, P. A. Bonczyk, and J. F. Verdieck, Applied Spectroscopy Reviews 13, 15-164 (1978); Progress in Energy and Combustion Science 5, pp. 253-322 (Pergamon Press, 1979).
3. A. C. Eckbreth, Eighteenth Symposium (International) on Combustion, pp. 1471-1488 (The Combustion Institute, Pittsburgh, PA, 1981).
4. A. G. Bell, Proc. Am. Assoc. Adv. Sci. 29, 115 (1880); Philos. Mag. 11, 510 (1881).
5. Optoacoustic Spectroscopy and Detection, Ed. Y-H Pao, (Academic Press, 1977).
6. J. E. Allen, W. R. Anderson, and David Crosley, Optics Letters 1, 118 (1977); W. R. Anderson, J. E. Allen, Jr., T. D. Fansler, and D. R. Crosley, Paper presented at Tenth Materials Research Symposium, Gaithersburg, MD, Sept. 1978.
7. K. Tennal, G. J. Salamo, and R. Gupta, Applied Optics 21, 2133 (1982).
8. C. K. N. Patel and A. C. Tam, Rev. Mod. Phys. 53, 517 (1981).
9. L. D. Landau and E. M. Lifshitz, Fluid Mechanics (Pergamon, New York, 1959).
10. G. Grynberg and R. Cagnac, Rep. Prog. Physics 40, 791 (1977).
11. E. L. Merryman and A. Levy, Fifteenth Symposium (International) on Combustion, pp. 1073-83 (The Combustion Institute, Pittsburgh, PA, 1975).
12. D. Hsu, D. L. Monts, and R. N. Zare, A Spectral Atlas of NO₂, (Academic, New York, 1978).
13. T. C. Hall, Jr., and F. E. Blacet, J. Chem. Phys. 20, 1745 (1952); V. M. Donnelly and F. Kaufman, J. Chem. Phys. 66, 4100 (1977).
14. G. H. Dieke and H. M. Crosswhite, J. Quant. Spectroscopy and Rad. Transfer 2, 97 (1962).
15. W. L. Dimpfl and J. L. Kinsey, J. Quant. Spectroscopy and Rad. Transfer 21, 233 (1979).
16. R. J. Cattolica, Sandia National Laboratory report.
17. C. H. Muller III, K. Schofield, M. Steinberg, and H. P. Broida, Seventeenth Symposium (International) on Combustion, pp. 867-879 (The Combustion Institute, Pittsburgh, PA, 1979).

18. J. W. Daily, Applied Optics 15, 955 (1976).
19. D. Stepowski and M. J. Cottureau, Applied Optics 18, 354 (1979).
20. E. M. Piepmeier, Spectrochimica Acta, 27B, 431 (1972); 27B, 445 (1972).
21. J. W. Daily, Applied Optics 16, 568 (1977).
22. R. B. Green, R. A. Keller, P. K. Schenck, J. C. Travis, and G. G. Luther, J. Am. Chem. Soc. 98, 8517 (1976).
23. A. P. Baronavski and J. R. McDonald, J. Chem. Phys. 66, 3300 (1977); Applied Optics 16, 1897 (1977).
24. J. O. Berg and W. L. Shackelford, Applied Optics 18, 2093 (1979).
25. R. P. Lucht and N. M. Laurendeau, Applied Optics 18, 856 (1979).
26. J. W. Daily, Applied Optics 17, 225 (1978).
27. L. Pasternack, A. P. Baronavski, and J. R. McDonald, J. Chem. Phys. 69, 4830 (1978).
28. P. A. Bonczyk and J. A. Shirley, Combustion and Flame 34, 253 (1979).
29. M. B. Blackburn, J. -M. Mermet, G. D. Boutilier, and J. D. Winefordner, Applied Optics 18, 1804 (1979).
30. A. C. Eckbreth, P. A. Bonczyk, and J. F. Verdick, EPA publication No.-600/7-80-091.
31. R. K. Lenzel and D. R. Crosley, J. Chem. Phys. 68, 5309 (1978).
32. V. M. Donnelly, D. G. Keil, and F. Kaufman, J. Chem. Phys. 71, 659 (1979).

Appendix I

The probability of excitation from level 1 to level 2 is given by

$$\omega_{12} = B_{12} \int g(\nu) I_\nu d\nu \quad (\text{AI.1})$$

where B_{12} is the Einstein coefficient for absorption, I_ν is the laser intensity per unit frequency (watts/m²Hz), and $g(\nu)$ is the absorption profile of the molecules. The absorption profile in general is due to a combination of homogeneous and inhomogeneous broadening mechanisms and is given by a Voigt profile. We will assume $g(\nu)$ to be normalized to unity, i.e.

$$g(\nu) d\nu = 1 \quad (\text{AI.2})$$

For a simplified discussion, we will write AI.1 as

$$\omega_{12} = \gamma B_{12} I_\nu \quad (\text{AI.3})$$

where γ is a factor which is given by the laser line profile and absorption profile of the molecules. For example $\gamma = 1$ for "white light" excitation. In our experiments with NO₂, the laser linewidth was 3 cm⁻¹ and the "white-light" excitation is a good approximation.

In our experiments with OH molecules, the laser was operated with a high finesse etalon and the laser linewidth was about 10 GHz. The absorption linewidth of OH molecules is also about 10 GHz. For simplified discussion, we will assume that both the laser profile I_ν and the molecular absorption profile $g(\nu)$ are given by Gaussians of equal width (FWHM) $\Delta\nu$. In that case it is a simple matter to integrate AI.1 and one gets

$$\gamma = \sqrt{\frac{2 \ln 2}{\pi}}$$

Appendix II

The quenching rate of the excited OH molecules Q_2 is given by

$$Q_2 = \sigma \bar{v} n \quad (\text{AII.1})$$

where σ is the quenching cross section, \bar{v} is the average relative velocity of OH molecules with respect to other flame molecules, and n is the number density of the flame molecules. Assuming the flame molecules to be predominantly N_2 , the quenching cross section is³¹ $\sigma = 5.8 \times 10^{-16} \text{ cm}^2$. For a flame temperature of about 1300° K, we obtain $Q_2 = 6.4 \times 10^8 \text{ sec}^{-1}$. The spontaneous emission rate A_{21} is known¹⁵ to be $6.2 \times 10^5 \text{ sec}^{-1}$ for $Q_2(6)$ transition. The absorption rate $\gamma B_{12} I_\nu$ (which is also approximately equal to the stimulated emission rate) is approximately $2.4 \times 10^7 \text{ sec}^{-1}$. Here we have taken the Einstein B-coefficient from Ref. 15, and have taken the laser energy to be about 100 μJ in a pulse length of $\sim 1 \mu\text{sec}$, and in a bandwidth of 10 GHz. γ is taken to be 0.66 (see Appendix I). Thus we are clearly justified in assuming that $Q_2 > [A_{21} + \gamma(B_{12} + B_{21})I_\nu]$.

The same conclusion can be drawn for NO_2 molecules using the quenching cross sections given by Donnelly et al.³²

Appendix III

The intensity of the laser radiation I_A absorbed in traversing a length z in the flame (due to absorption by OH or NO₂ molecules) is given by

$$I_A = I_0 (1 - e^{-\bar{\alpha} z}) \quad (\text{AIII.1})$$

where I_0 is the incident laser intensity (watts/m²). We will use AIII.1 as the operating definition of an average absorption coefficient $\bar{\alpha}$, i.e., absorption coefficient averaged over the absorption profile of the molecules and the line profile of the laser. We need to write the absorption coefficient in terms of the number density N_0 of the OH or NO₂ molecules. To this end, we write the absorption coefficient in terms of the Einstein coefficient

$$\alpha(\nu) = h\nu N_1 B_{12} g(\nu) \quad (\text{AIII.2})$$

where $g(\nu)$ is the molecular absorption profile (Appendix I). If we multiply both sides of AIII.2 by the laser intensity per unit frequency I_ν , and integrate, we obtain

$$\bar{\alpha} = h\nu N_1 \gamma B_{12} I_\nu / I_0 \quad (\text{AIII.3})$$

where we have used the results of Appendix I. Implicit in the derivation of AIII.3 is the assumption that the medium is weakly absorbing, i.e., the laser intensity is not significantly modified as it propagates in the medium. Although this assumption is not strictly valid for main branches of OH, we will nevertheless use it in this simplified approach.

When the quenching rate Q_2 is much faster than the radiative rates (see Appendix II), Eq(1) shows that $N_2 \ll N_0$. In that case we may replace N_1 by the total number density of OH or NO₂ molecules N_0 , to obtain

$$\bar{\alpha} = h\nu N_0 \gamma B_{12} I_\nu / I_0 \quad (\text{AIII.4})$$

Appendix IV

DIGITIZER-PET INTERFACE

The data transfer interface is made through the parallel binary interface port (PBIP) on the digitizer and the parallel user port on the PET. In addition to the wiring between these ports, a small amount of digital hardware is required to supply the necessary communications. The ports, the hardware, and the associated communication signals are described in this appendix.

1. Digitizer Parallel Port

The digitizer PBIP is a 25 pin jack. It has eight data lines and grounds, three control lines and one external clock line the control lines are "data request", "data ready" and "clock mode". "Data ready" is a handshake sent by the digitizer following an external request for data transfer. "Clock mode" selects whether the digitizer or an external source will supply the clock pulses which cause the next byte to be put on the data lines. The PET supplies these pulses in our case. Grounding the "clock mode" line sets this condition.

2. PET User Port and Registers

The PET user port is a 24 contact edge connector. Twelve contacts are for trouble shooting equipment and the other twelve are available to the user. Of these, eight are data lines, two are digital grounds and two are the control lines CA1 and CB2. CA1 is used to receive the incoming "data ready" signal and CB2 is used for sending the clock pulse.

The control and data lines are associated with different registers in the PET*. Two other registers must be initialized. Table 1 lists the registers

*Register refers to a memory location with a specific function.

TABLE 1: List of PET Registers Used With Data Transfer Program

<u>Register</u>	<u>Function</u>	<u>Condition</u>	<u>Initializing Command</u>
59459	Data direction register. Tells PET if data register bits are used for input or output.	LO implies that the corresponding bit of the data register is used for input. HI implies output.	POKE 59459, 0 (sets all bits for input)
59457	Data register with handshake. CA1 flag goes LO when this register is read.	_____	_____
59471 (not used here)	Data register without handshake (does not affect CA1 flag).	_____	_____
59469	Interrupt Flag Register (IFR). Bit 1 is handshake signal.	Bit 1 set by transition of CA1 at user port. Cleared when data register 59457 is read.	_____
59468	Peripheral Control register. Bit 0 determines type of CA1 transition required to set Bit 1 of IFR. Bits 5, 6, 7 control CB2 function. 6 and 7 HI implies manual output mode. Bit 5 then controls CB2.	Bit 0 HI implies positive transition required. (LO implies negative transition). Bit 5 LO sets CB2 LO. Bit 5 HI sets CB2 HI.	POKE 59468, (PEEK (59468) AND 31) OR 193. (Sets bits 0, 6, 7 HI and bit 5 LO without affecting other bits)

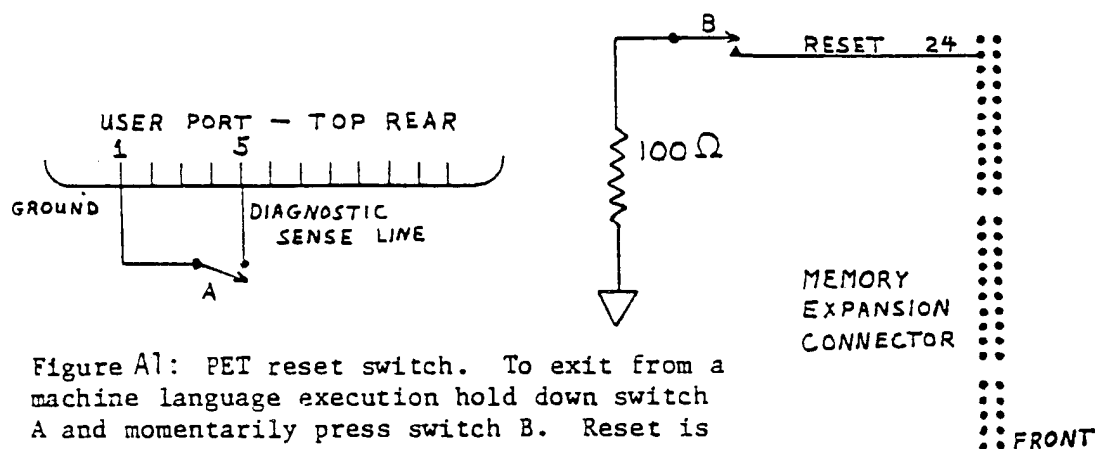


Figure A1: PET reset switch. To exit from a machine language execution hold down switch A and momentarily press switch B. Reset is to TIM control.

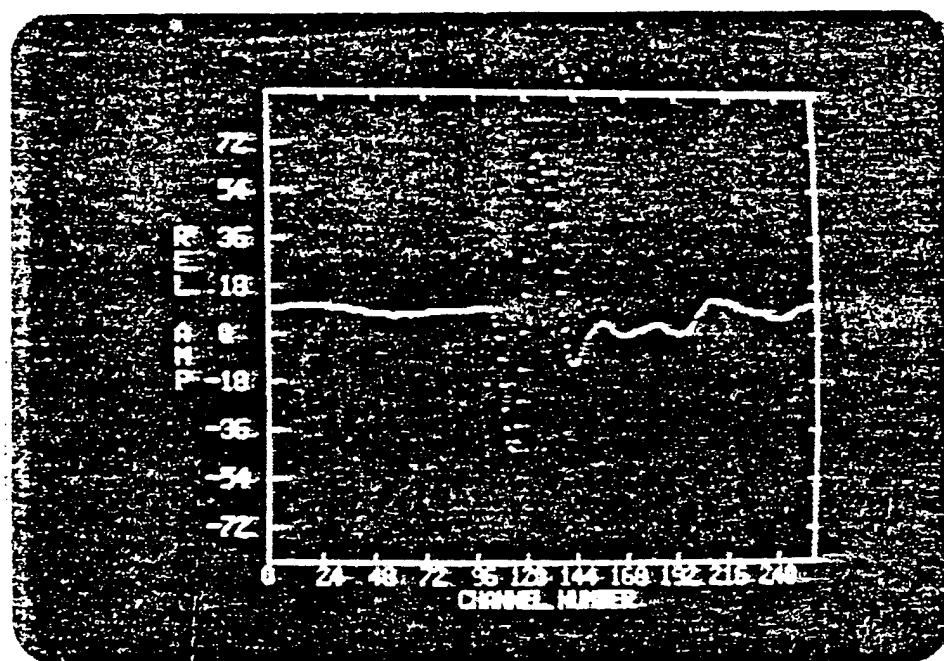


Figure A2: PET screen with High density plot showing a digitized photoacoustic signal. Borders and labels are programmable.

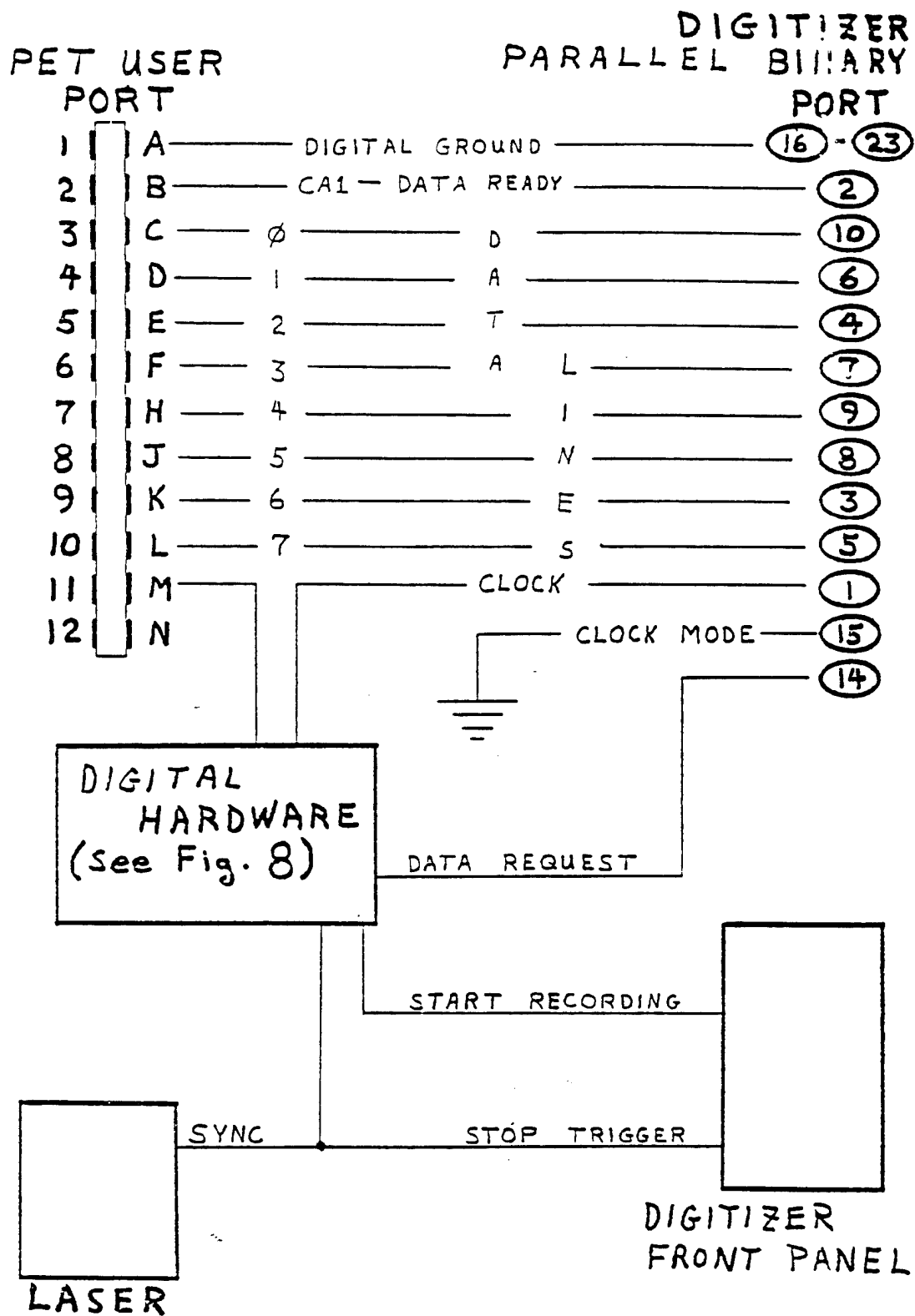


Figure A3: Hardwiring for PET-Digitizer interface

Figure A4: Interface digital hardware

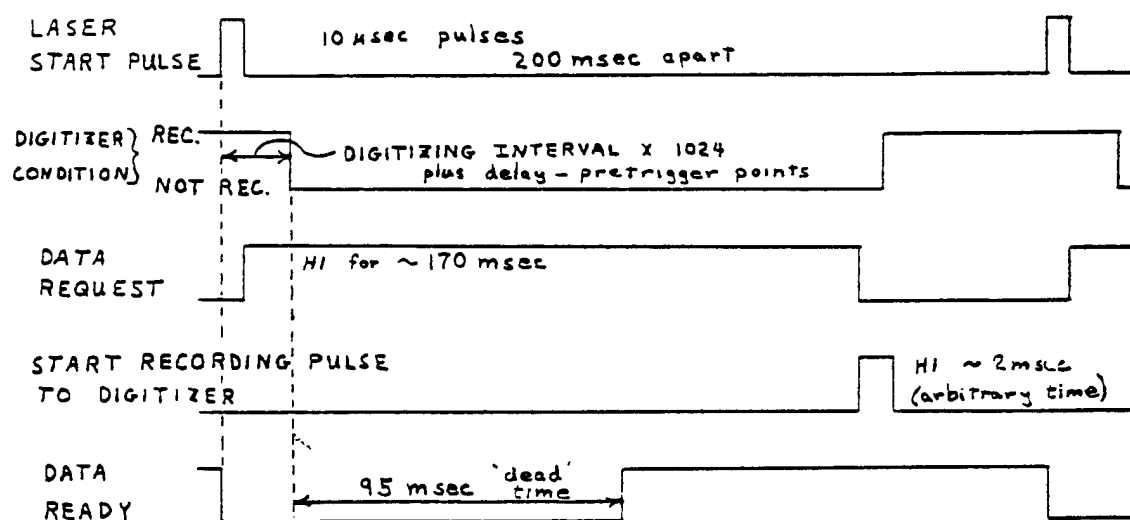
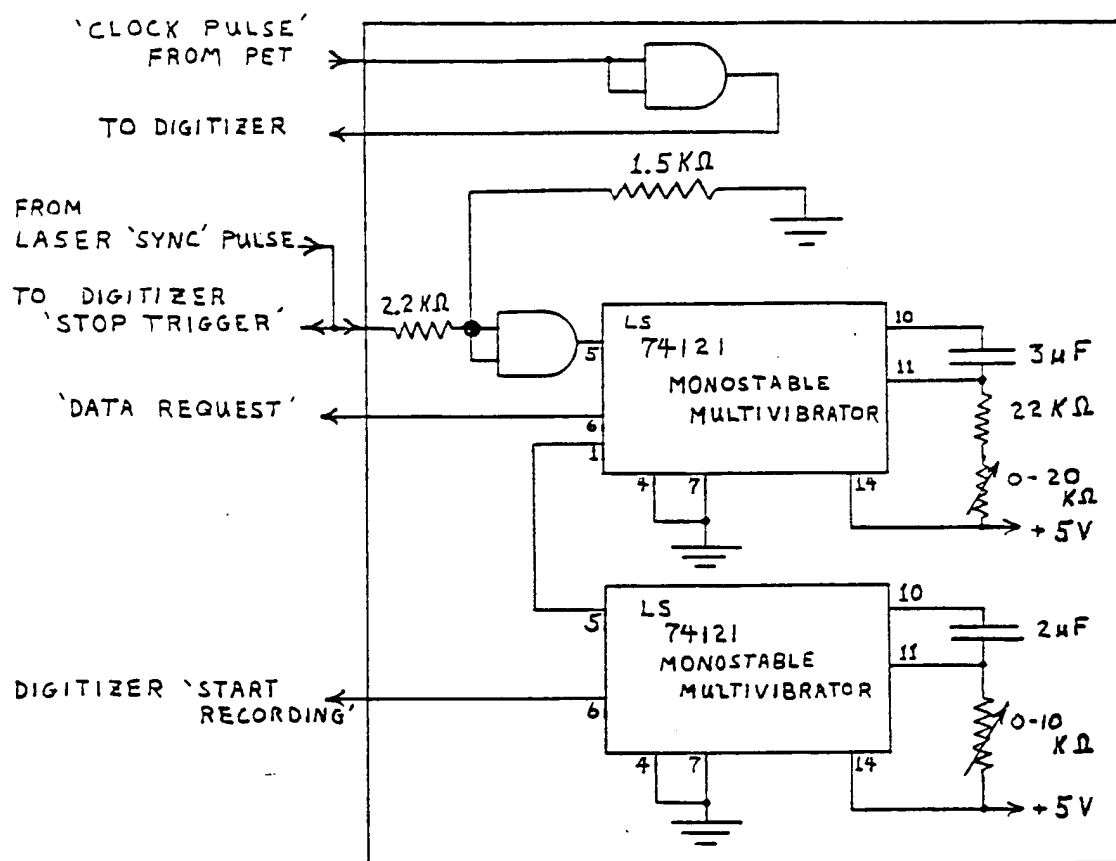


Figure A5: Interface signal timing sequences

used, their functions, and the initialization command where applicable.

3. Wiring and Digital Hardware

Figure A3 shows the wiring between the digitizer and the PET and Figure A4 is a diagram of the digital hardware required for the interface. The hardware consists of two 74121 monostable multivibrators with associated resistors and capacitors for setting signal widths and a 7408 quad AND gate. The output of the first multivibrator is set to about 170 ms. The second is set to about 1 ms. The roles of these signals are discussed in the next paragraph. The AND gate is in the clock pulse circuit because the PET CB2 voltage is loaded down by the low input resistance (100 ohms) of the digitizer.

4. Signal Sequences

Figure A5 shows the timing sequences for the interface communications and for the equipment status. The laser "sync" pulse supplies the "stop trigger" signal at the digitizer front panel. It also causes the first monostable multivibrator to generate the "data request" signal. The digitizer continues recording for a preset number of sampling intervals after the "stop trigger". It then has a 95 ms "dead time" before "data ready" is set high. This is the greatest limiting factor on pulse repetition rate. When the PET receives the "data ready" signal it alternately reads the data register and sends clock pulses until 256 channels have been read and added into memory. The data transfer takes about 17 ms. "Data request" is kept high for about 170 ms. This time allows data with digitizing intervals up to 50 microseconds per channel to be recorded and transferred at the rate of 5 pulses per second. The downward transition of the "data request" signal causes the second multivibrator to send a "start recording" pulse to the front panel of the digitizer.

Recording begins after a delay time of about fourteen milliseconds and then continues until the next laser pulse.

5. Machine Language Program

A data transfer program has been written in the machine language. At the start of a data run, the program zeroes three pages (1 page = 256 bytes) of random access memory, using hexadecimal page numbers \$30-\$32 for the first run and then advancing to the following three pages for each subsequent run. Following a laser pulse the data from each of the first 256 bytes of digitizer memory is added into the corresponding byte of the first of the three PET memory pages assigned to that run. When an addition causes a byte to overflow, ($\text{sum} > 255$), a one is added to the corresponding byte of the next page. The amount of overflow ($\text{sum} - 255$) is kept in the first byte.

6. Basic Program

The Basic control program is set up for easy operator use. One need only type RUN and answer the questions appearing on the PET screen.

Part II
Application of the Photothermal Effect
to Combustion Diagnostics

A. Introduction

As we know by simply placing our hand in sunlight, absorption of light energy will result in thermal energy or the heating of an object. Over the last few years, this physical phenomenon has been the basis of the development of several rather clever schemes for measuring very low optical absorptions. For example, interferometry,¹ thermal lensing,² photoacoustic spectroscopy,³ photothermal radiometry,⁴ and photothermal deflection⁵ are each active fields of study for the measurement of low absorptions via an optical to thermal energy conversion. It is our interest here to report on the success of one of these schemes, photothermal deflection, to detect low optical absorption in a flame environment and hence to measure the concentration of minority species during combustion.

B. Discussion of the Photothermal Deflection Technique

The basic physical idea behind photothermal deflection is similar to the "mirage effect." That is, when viewing an object through warm rising air we notice that our perceived image of the object "wiggles." This is due to the fact that the rising warm air between the object and receiver causes index of refraction variations. These variations result in small deflections of light rays which travel from the object to the receiver.

In the photothermal deflection technique an optical pulse from a laser, called the pump beam, passes through a sample. The optical absorption processes in the sample, at the pump beam, causes some absorption of the beam energy. As a result heat is generated in the sample which causes a corresponding change

in the index of refraction of the optically heated region. Since the pump beam intensity has a transverse profile which peaks at the center of the beam and falls off to zero rapidly, the resulting index of refraction change has a similar profile. This physical situation is pictured in Fig. 1. At this point a second laser beam, called the probe beam, which has a smaller cross sectional diameter, crosses the pump beam. However, the alignment is such that the center of both beams are displaced slightly. As a result the probe beam passes through the sample in a region of space which acts like a lens⁶ and causes a deflection of the probe beam. The magnitude of the deflection is then an indication of the absorption of the pump beam by the sample.

(i) Overlapping Pump and Probe Beams⁷

The magnitude of the photothermal deflection can be calculated using a simple physical model. In this model the index variation caused by the pump beam can be written as

$$n(r,t) = n_0 + \Delta n(r,t) \quad (1a)$$

$$n(r,t) = n_0 + \frac{\partial n}{\partial T} T(r,t) \quad (1b)$$

where T is the temperature profile produced by the pump beam. This expression is of course just a Taylor expansion of the temperature dependence of the index of refraction and is valid for the small variations produced in our work. The propagation of the probe beam through this spatially varying index of refraction can then be estimated using the ray equation⁸

$$\frac{d}{ds} \left(n \frac{d\vec{r}}{ds} \right) = \nabla n \quad (2)$$

where s is the distance along the ray measured from some fixed position on it and \vec{r} is the position vector of the point at s . For paraxial rays we can simplify this equation by replacing

$$\frac{d}{ds} \rightarrow \frac{d}{dz} \quad (3)$$

where z is the propagation direction of the incoming pump laser beam. With this approximation, equation (2) becomes

$$\frac{d}{dz} \left(n \frac{dr}{dz} \right) = \nabla n \quad (4)$$

To simplify this equation further we may also assume that the index of refraction has only a radial dependence. Since the absorption is generally weak in our experiments, the assumption of near linear absorption is in fact a very good one. As a result, equation (4) simplifies to:

$$\frac{d}{dz} \left(n \frac{dr}{dz} \right) = \frac{\partial n}{\partial r} \quad (5)$$

In general, the change in the index of refraction induced by the pump beam will be time dependent due to the diffusion of heat away from the deposition region. However, in our studies the thermal deflection time τ_{th} of the probe beam is much shorter than the thermal diffusion time τ_D across the probe beam. In fact, τ_{th} was of the order of microseconds while τ_D was of the order of milliseconds. Since $\tau_{th} \ll \tau_D$ we may assume thermal diffusion to be negligible during the time that the probe beam is undergoing an induced deflection. Physically, this means that we may take the index of refraction in equation (5) to be time independent. This assumption will allow us to solve equation (5) for the maximum deflection of the probe beam. Of course, in practice the peak deflection

would then decrease as a function of time due to thermal diffusion. Our assumption, then, allows calculation of the maximum deflection expected but will give no information about the time dependence of the deflection signal.

The right hand side of equation (5) asks for the rate of the radial variation of the index of refraction. Physically, this is indirectly caused by the radial variation of the pump beam intensity and more directly by the corresponding radial dependence of the temperature variation across the probe beam. As a result, we may re-express equation (5) as:

$$n \frac{d^2 r}{dz^2} = \frac{\partial n}{\partial T} \cdot \frac{\partial T}{\partial I} \cdot \frac{\partial I}{\partial r} \quad (6)$$

where I is the pump beam intensity. To find the maximum deflection we may integrate equation (6) over z giving

$$\phi = \text{deflection angle} = \frac{dr}{dz} \quad (7a)$$

$$= \frac{1}{n} \int_0^{\ell} \frac{\partial n}{\partial T} \cdot \frac{\partial T}{\partial I} \cdot \frac{\partial I}{\partial r} dz \quad (7b)$$

where ℓ is the absorption path of the pump beam in the sample. Since we have assumed no z -dependence of I , T , or n , we get after integration of the right hand side of equation (7):

$$\phi = \frac{\ell}{n} \frac{\partial n}{\partial T} \cdot \frac{\partial T}{\partial I} \cdot \frac{\partial I}{\partial r} \quad (8)$$

In order to calculate ϕ we obviously must obtain values of each of the partial derivatives in equation (8).

We can obtain an expression for the $\frac{\partial T}{\partial I}$ by examining the relationship between the heat deposited by absorption and the resulting temperature rise. This is simply given by the specific heat equation:

$$H = m c T \quad (9)$$

where m is the mass of the excited sample, c is the specific heat of the sample material, and H is the heat deposited as a result of absorption of the pump beam by the sample. If we let α be the sample absorption coefficient, A the cross sectional area of the pump laser beam, and τ_p the temporal width of our pulsed pump beam, the heat absorbed by our sample is given by

$$H = \alpha I A \tau_p \quad (10)$$

where we have assumed that all of the optically excited species in our sample decay by non-radiative mechanisms. At the temperatures and pressures of our flame this is a good assumption. Using equation (10) in (9) we get:

$$\alpha I \tau_p = \rho c T \quad (11)$$

where ρ is the sample mass density. Differentiating (11) we get

$$\frac{\partial T}{\partial I} = \frac{\alpha \tau_p}{\rho c} \quad (12)$$

In order to obtain an expression for $\frac{\partial I}{\partial r}$ we must know the radial dependence of the pump beam intensity $I(r)$. As is most commonly done, we will assume a Gaussian profile for the pump beam. This approximation is one of the weakest in our analysis but is expected to give results valid to a factor of 2. Taking $I(r)$ to be Gaussian we have:

$$I(r) = I_0 e^{-2r^2/\omega^2} \quad (13a)$$

$$\frac{\partial I}{\partial r} = \frac{-4r}{\omega^2} e^{-2r^2/\omega^2} I_0 \quad (13b)$$

where ω is the pump beam waist. Using equations (12) and (13) we can now rewrite equation (8) as:

$$\phi = \frac{i}{n} \frac{\partial n}{\partial T} \left(\frac{\alpha \tau_p}{\rho c} \right) \left(\frac{4r}{\omega} e^{-2r^2/\omega^2} I_0 \right) \quad (14)$$

Each of the values in equation (14) are now known and an estimate of ϕ can then be made for a sample of 554 ppm NO₂. This results in a value of $\phi_m = 6.7 \times 10^{-5}$ radians, with $r = \omega$ for maximum deflection.

This is a number which can be directly compared with our experimental measurement. In particular, we have measured a value of 30 Volts using a position sensitive detector. In order to convert this signal value to a value for ϕ we have calibrated our detector response using a known value of ϕ . This has resulted in a calibration value of the sensitivity $S = 5 \times 10^5$ Volts/radian. Therefore, 30 Volts corresponds to a value of 6×10^{-5} radians which is in excellent agreement with our result of 6.7×10^{-5} radians predicted using our simple physical model. In fact, this agreement is much better than could be expected using the approximations we have made for the overlapping laser beam geometry in our experiment. However, it should be noted that we have employed our simple model only to point out the physical mechanisms giving rise to the photothermal deflection. Actually, the difficulties we have encountered in making an accurate estimate using a simple model in no way limit the applicability of the photothermal technique. For example, the geometry problems can be zeroed-out using a known absorption to either determine the geometry factor or simply calibrate the deflection ϕ_m as a function of absorption α .

(ii) Spatially Separated Pump and Probe Beam

Although we have found good agreement between theory and experiment for the case of a NO_2 sample cell, the application of this technique to a combustion environment produces complications because of the possible existence of concentration gradients of the absorbing molecules. In this case, deflection of the probe beam can be due to the concentration gradients as well as the laser intensity gradient. In order to eliminate this ambiguity we have investigated the photothermal deflection as a function of the spatial separation between the pump and probe beams. The physical situation is depicted in Fig. 2. The top part of the figure shows how the two beams look when viewed from above. The bottom part shows cross sections of the two beams in vertical planes at three different positions. In other words, the two beams are in two different horizontal planes.

In the case of non-overlapping probe and pump beams a totally different physical mechanism is expected to result in a thermal deflection of the probe beam. In particular, the pump beam produces a thermal gradient in the flame. This in turn results in an acoustical wave⁹ which propagates outward. The propagating acoustic wave leaves behind a trail of heat proportional to its intensity. It is this "secondary heat" delivered to the flame medium which results in heat at the probe beam when spatially separated from the pump beam. Of course heat alone does not cause a deflection. Rather, a thermal gradient is required as in the case of the overlapping beams where the thermal gradient was provided by the Gaussian laser beam profile. In the non-overlapping case a thermal gradient results due to the geometric spreading of the acoustical pulse as it propagates outward as a cylindrical pressure wave.¹⁰ That is, the acoustical wave is decreasing in amplitude as we move away from the pump beam

due to geometric spreading. As a result, the "trail of heat" left behind is a function of the separation between the pump and probe beams.

The magnitude of the thermal deflection expected in this case can be obtained from an equation similar in form to our previous equation (8).

$$\phi = \frac{\lambda}{n} \frac{\partial n}{\partial T} \cdot \frac{\partial T}{\partial I_A} \cdot \frac{\partial I_A}{\partial r} \quad (15)$$

In this case we have replaced the laser pulse intensity I by the acoustic pulse intensity I_A since it is the acoustic pulse which heats the medium causing T and n to change. Likewise the analog to equation (12) is:

$$\frac{\partial T}{\partial I_A} = \frac{\alpha_A \tau_p}{\rho c} \quad (16)$$

where α_A is now the acoustic absorption coefficient and τ_p the temporal width of the acoustic pulse.

We can also write an expression for $\frac{\partial I_A}{\partial r}$. The cylindrical acoustic wave falls off as $1/\sqrt{r}$ and therefore the acoustical intensity as $1/r$ or:

$$I_A = \frac{I_{A0} r_A}{r} \quad (17)$$

where r_A is the radius of the acoustical wave at the time of its origin. Therefore, we have

$$\frac{\partial I_A}{\partial r} = -\frac{I_{A0}}{r^2} r_A \quad (18)$$

Using equations (16) and (18) we can now rewrite equation (15) as

$$\phi = -\frac{\lambda}{n} \frac{\partial n}{\partial T} \frac{I_{A0}}{r^2} r_A \frac{\alpha A^{\tau} P}{\rho c} \quad (19)$$

Using $C_1 \alpha$ as the conversion efficiency from optical energy into acoustical energy⁹ we can write (19) as

$$\phi = -\frac{\lambda}{n} \frac{\partial n}{\partial T} \frac{\alpha C_1 I_0}{r^2} r_A \frac{\alpha A^{\tau} P}{\rho c} \quad (20)$$

where I_0 is now once again the laser intensity and α the optical absorption coefficient. Each of the values in equation (20) are now known to us so we can calculate ϕ , the expected thermal peak deflection, at $r = 1$ mm and compare with our observations. This calculation yields

$$\phi_{\max} = .52 \times 10^{-8} \text{ radians.} \quad (21)$$

Therefore,

$$V_{\max} = S \phi_{\max} = .26 \times 10^{-3} \text{ Volts} \quad (22)$$

Our detection limitation due to background noise is about 4×10^{-2} Volts so that it becomes difficult to detect a deflection resulting from this phenomenon. However, we do observe a thermal deflection signal at $r = 1$ mm of the order of .1 Volts! This is much higher than expected. We believe at this time that the deflection is caused by the wings of the diffraction pattern of a near Gaussian beam diffracted by a circular aperture.¹¹ In fact, the signal

intensity would then fall off very rapidly with the beam separation in this case, in agreement with our observations as seen in 554 ppm NO_2 (Figure 3). Fig. 4 shows three typical thermal deflection signals as a function of beam separation. Notice that there appears to be a fast signal superimposed on a signal of longer characteristic time. In particular, the longer fall time is of the order of milliseconds while the fast signal is of the order of microseconds.

(iii) Photoacoustic Deflection Technique

In our simple model for thermal deflection of spatially separated beams we indicated that an acoustical pulse propagates outward from the pump beam and "passes by" the probe beam. The microsecond deflection indicated in Fig. 4 is in fact a deflection of the probe beam caused by this acoustical pulse. Fig. 5 shows the acoustical pulse for three different beam separations. The time delay between these curves corresponds to the increased acoustic travel time between the pump and probe beams in support of our interpretation. Fig. 6 shows the magnitude of the deflection as a function of beam separation. The data is consistent with an inverse distance fall-off in the intensity of the acoustic wave when the probe and the pump beams are spatially separated (> 2 mm).

The magnitude of the photoacoustic deflection expected can be obtained once again using an equation similar to equation (3).

$$\phi_{\max} = \frac{l}{n} \frac{\partial n}{\partial P} \frac{\partial P}{\partial r} \quad (23)$$

where P is the pressure in the acoustic pulse.

In this case we have replaced the $\frac{\partial n}{\partial T}$ by $\frac{\partial n}{\partial P}$ since the index of refraction is undergoing a change due to a corresponding pressure change as opposed to a

temperature change considered earlier. Likewise the $\frac{\partial I}{\partial r}$ has been replaced by the $\frac{\partial P}{\partial r}$ since it is the pressure gradient which is now causing an index gradient as opposed to the optical intensity gradient examined earlier. Not knowing what to assume as the shape of our acoustical pulse we have chosen a Gaussian profile as a reasonable guess. In this case

$$P = P_0 e^{-2r^2/\omega^2} \quad (24)$$

Taking the value at $r = \omega$ as the maximum deflection point we get

$$\left(\frac{\partial P}{\partial r}\right)_{\max} = -P_0 \frac{4}{\omega} e^{-2} \quad (25)$$

which at $\omega = 1 \text{ mm}$ gives

$$\left(\frac{\partial P}{\partial r}\right)_{\max} \approx -5P_0 \quad (26)$$

We have estimated $\frac{\partial n}{\partial P}$ at constant volume as

$$\frac{\partial n}{\partial P} \approx 3 \times 10^{-9} \frac{M^2}{N} \quad (27)$$

Therefore, using equations (26) and (27) we can write equation (23) as:

$$\phi_m = \frac{\ell}{n} \frac{\partial n}{\partial P} \left(\frac{\partial P}{\partial r}\right)_{\max} \quad (28a)$$

$$= 6(3 \times 10^{-9})(5P_0) \quad (28b)$$

We can estimate P_o by using the relationship¹²

$$P_o^2(t=0) = \frac{2E_A \rho v_s^2}{\pi r_o^2} \quad (29)$$

and the fact that

$$E_A = E_L \alpha C_1 \quad (30)$$

where E_L is the laser pulse energy and αC_1 is as before the conversion factor of optical to acoustical energy. Using equation (30) in (29) we get

$$P_o = 39.7 \frac{N}{M^2} \quad (31)$$

This value can now be used to find the pressure at 5 mm from the pump beam using

$$P_o(5 \text{ mm}) = P_o \frac{r_A}{r_{5\text{mm}}} \quad (32a)$$

$$= 39.7 \sqrt{1/5} = 17.75 \frac{N}{M^2} \quad (32b)$$

which using equation (28) becomes

$$\phi_{\max} = 6(3 \times 10^{-9})(5 \times 17.75) \quad (33a)$$

$$= 1.6 \times 10^{-6} \text{ radians} \quad (33b)$$

which using our sensitivity of $S = 5 \times 10^5$ becomes:

$$V_{\max} = .8 \text{ Volts} \quad (34)$$

This is to be compared with the observed value of .5 volts. Again our agreement can be considered as quite good considering the approximations made. From our results it would appear that the photoacoustic deflection technique will have high sensitivity, good temporal resolution, and good spatial resolution and hence be an excellent candidate for a combustion diagnostic tool.

C. Experimental Apparatus

A schematic of the photothermal deflection apparatus used in our experiments is shown in Figure 7. The only change in the apparatus over the experimental arrangement used in the previously described photoacoustic work in Part I is the use of a probe HeNe laser, dichroic filter, and a position sensitive detector in place of the microphone. Moreover, the resulting electrical signal from the position sensitive detector is handled in exactly the way as our photoacoustic microphone signals.

D. Results and Conclusions

Figures 8 and 9 show typical photothermal deflection and acoustical deflection signals taken in the flame environment, described in Part I, for a beam separation of a few millimeters. By observing both signals as a function of the pump beam wavelength we have identified the optical absorber to be the OH radical. In particular, our measurements were taken while tuned to the $Q_2(6)$ transition at $3092.2 \text{ }^{\circ}\text{A}$. As we indicated earlier we have not been able to unambiguously observe a photothermal signal with separated pump and probe beams and this was again true in our flame study. However, the acoustical deflections signal indicated a sensitivity of $4 \times 10^{-8} \text{ J}$ of energy absorbed per cm path length with averaging over 1000 pulses. This corresponds to a

detection sensitivity of about 2×10^{12} OH molecules/cm³. For comparison, this is a factor of 20 below our capability using a microphone detection scheme. However, the acoustical deflection technique has the added potential of spatial resolution.

In conclusion we have demonstrated for the first time the capability of a photoacoustic deflection technique to detect minority species in a flame environment. In addition, our investigation on the photothermal deflection technique has indicated that it is a technique with a sensitivity at least as good as our photoacoustic technique. However, under flame conditions potential density gradients presently prevent successful application of the technique as a diagnostic tool. Both techniques have the added potential, over our photoacoustic technique, of having spatial resolution. Much more work needs to be done, however, before this potential is realized.

E. References

1. J. Stone, J. Opt. Soc. Am. 62, 327 (1972) and Appl. Opt. 12, 1828 (1973).
2. J. R. Whinnery, Acc. Chem. Res. 7, 225 (1974) and R. L. Swofford and J. A. Morrell, J. Appl. Phys. 49, 3667 (1978).
3. For an overview see Y. H. Pao, Ed., Optoacoustic Spectroscopy and Detection (Academic, New York, 1977).
4. S. O. Kanstad and P. E. Nordal, Second International Topical Meeting on "Photoacoustic Spectroscopy," June 22-25, 1981, University of California, Berkeley, California.
5. A. C. Boccara, D. Fournier, and J. Badoz, Appl. Phys. Lett. 36, 130 (1980).
6. A. Yariv, Introduction to Optical Electronics (Holt, Rinehart and Winston, 1976).
7. A. C. Boccara, D. Fournier, W. Jackson, and N. M. Amer, Opt. Lett. 5, 377 (1980); D. Fournier, A. C. Boccara, N. M. Amer, and R. Gerlach, Appl. Phys. Lett. 37, 519 (1980); W. B. Jackson, N. M. Amer, A. C. Boccara, and D. Fournier, Appl. Opt. 20, 1333 (1981).
8. M. Born and E. Wolf, Principles in Optics, 3rd Ed. (Pergamon, New York, 1965) p. 121.
9. An estimate of the conversion efficiency can be obtained from: P. J. Westervelt and R. S. Larsen, J. Acoust. Soc. Am. 54, 121 (1973).
10. L. E. Kinsler, A. R. Frey, A. B. Coppens, and J. V. Sanders, Fundamentals of Acoustics, Third Edition (Wiley, 1982). See page 154. The acoustic absorption coefficient is much too small to produce a significant intensity gradient.
11. K. S. Aga, K. Tanaka, and O. Fukumitsu, Appl. Opt. 16, 2827 (1981).
12. S. Temkin, Elements of Acoustics (John Wiley and Sons, 1981) p. 73.

F. Figure Captions and Figures

1. Pump and probe beam profile. The left figure shows the beam cross section as seen along the propagation direction while the right side shows the resulting variation in index of refraction as seen by the probe beam.
2. Photothermal Deflection with spatially separated pump and probe beams. The top part of the figure shows how the two beams look when viewed from above. The bottom part shows the beam cross section as seen along the beam propagation direction.
3. Thermal deflection signal as a function of the separation between the pump and probe beams.
4. Three typical thermal deflection signals each taken at a different pump-probe beam separation. The top curve has a separation of .99 mm, the middle curve .96 mm, and the bottom curve .83 mm.
5. Photoacoustic deflection as seen at three different pump-probe beam separations. The time delay between the three curves corresponds to the increase in acoustic travel time between the pump and probe beams.
6. The photoacoustic peak deflection signal versus the pump-probe beam separation.
7. Photothermal Experimental Apparatus. The only change over the photoacoustic apparatus is the replacement of the microphone with the HeNe laser, dichroic filter, and position sensitive detector. The electrical signal from the position sensitive detector is digitized and averaged in exactly the same manner as the previously described signal from the microphone.
8. Typical photothermal deflection signal observed in OH.
9. Typical photoacoustic deflection signal observed in OH.

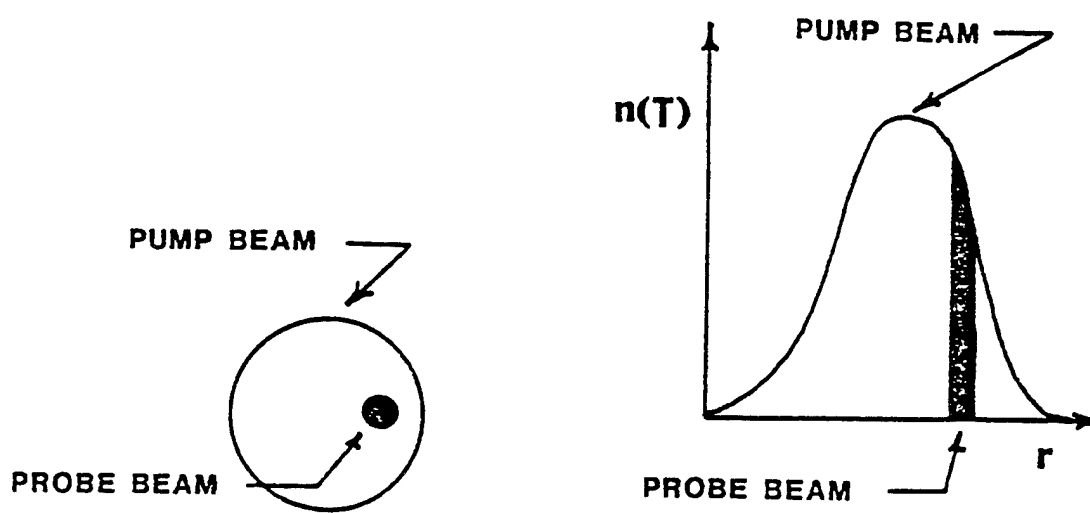


FIG 1

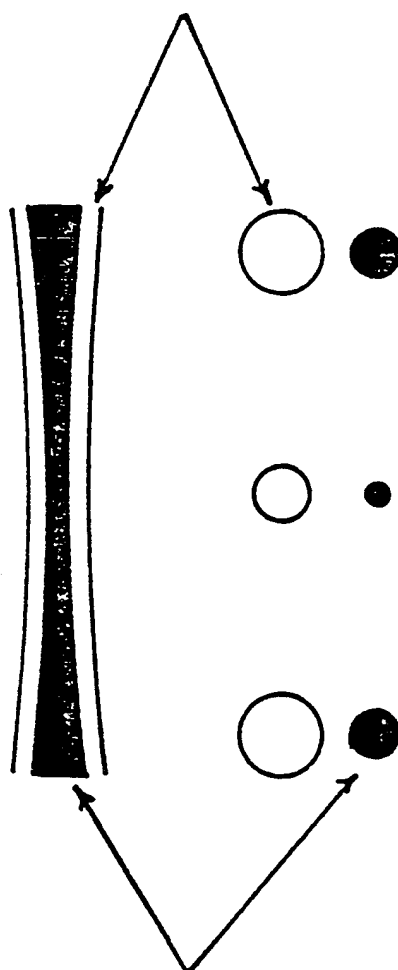


FIG 2

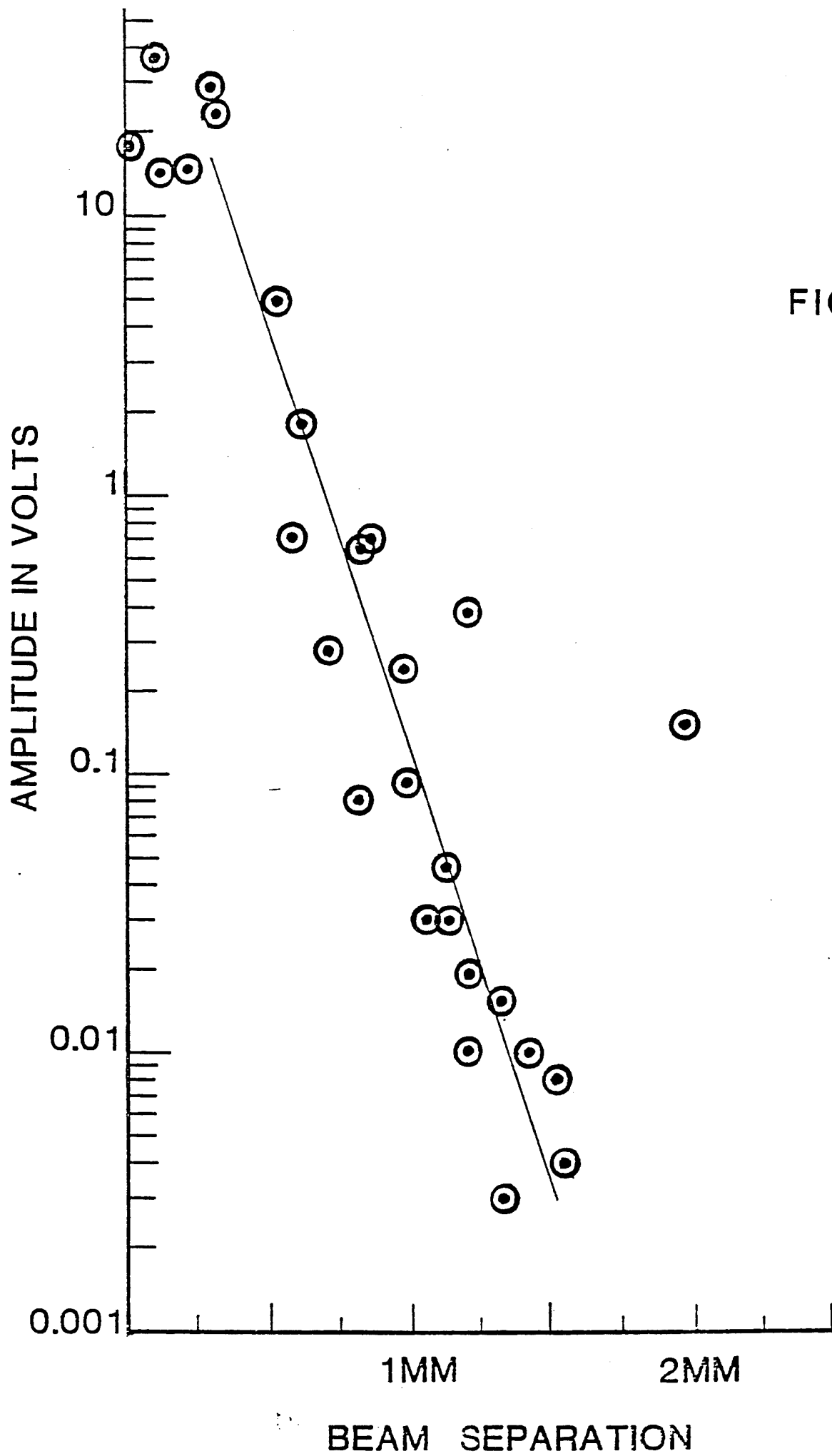


FIG 4

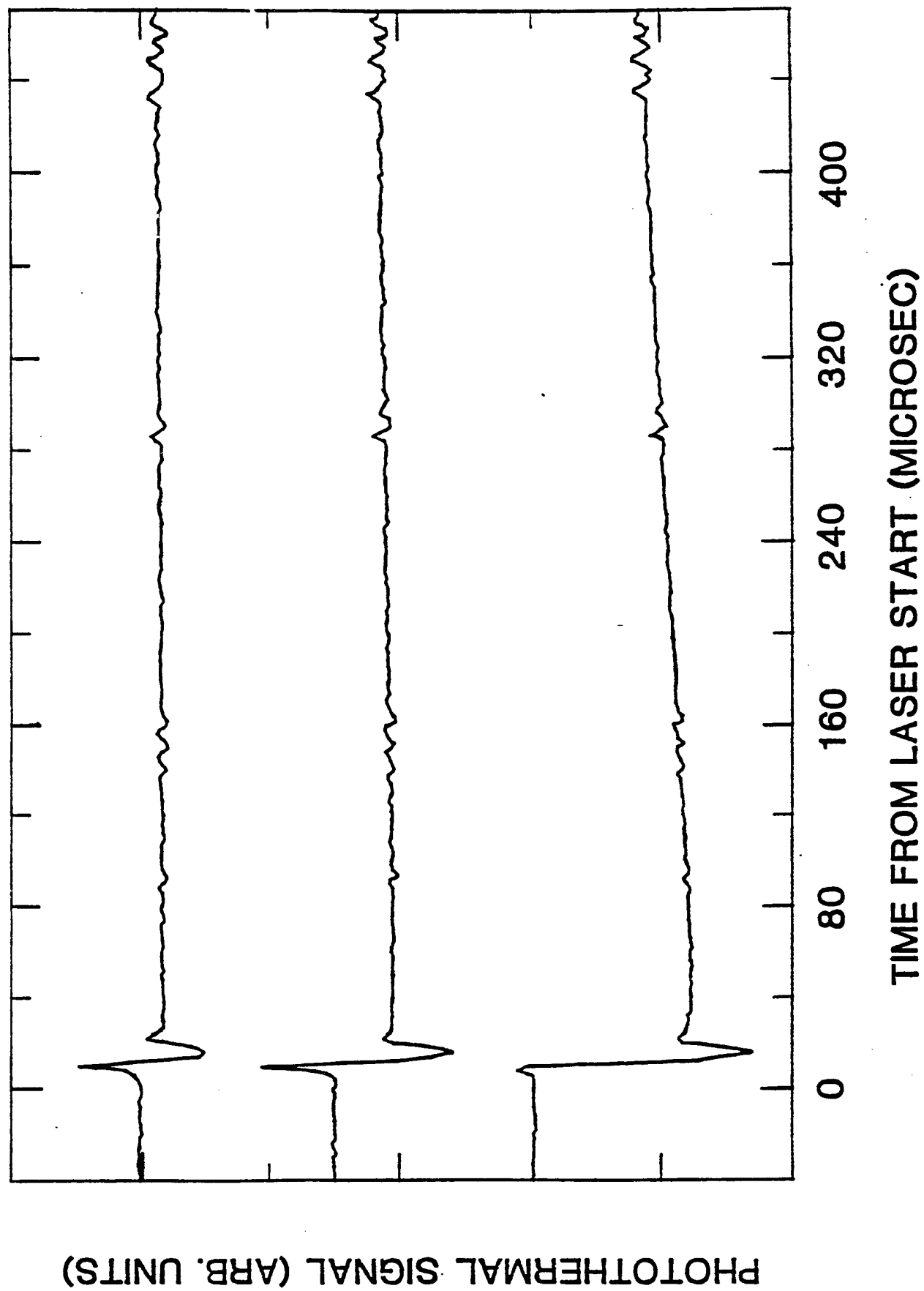
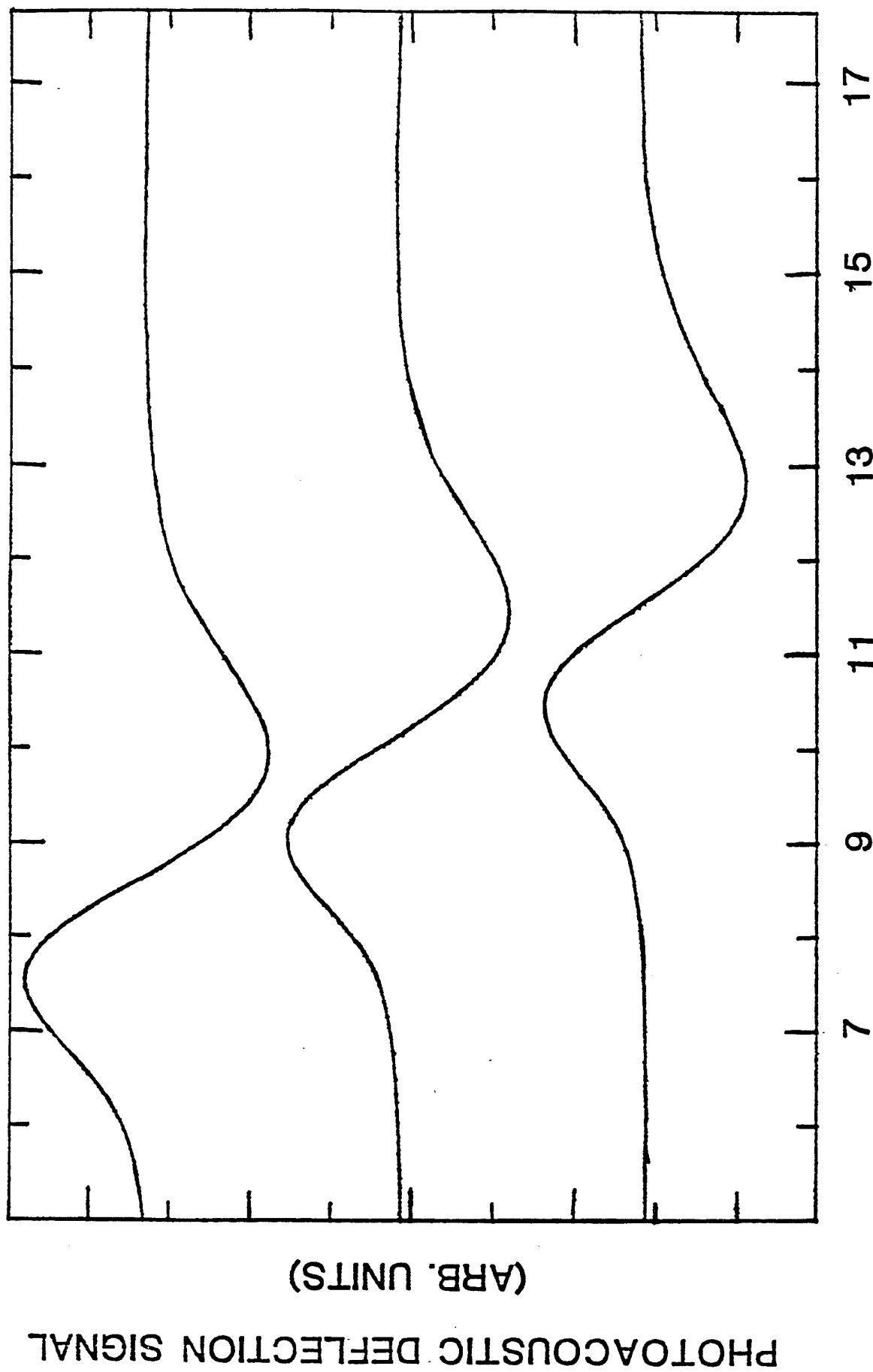


FIG 5



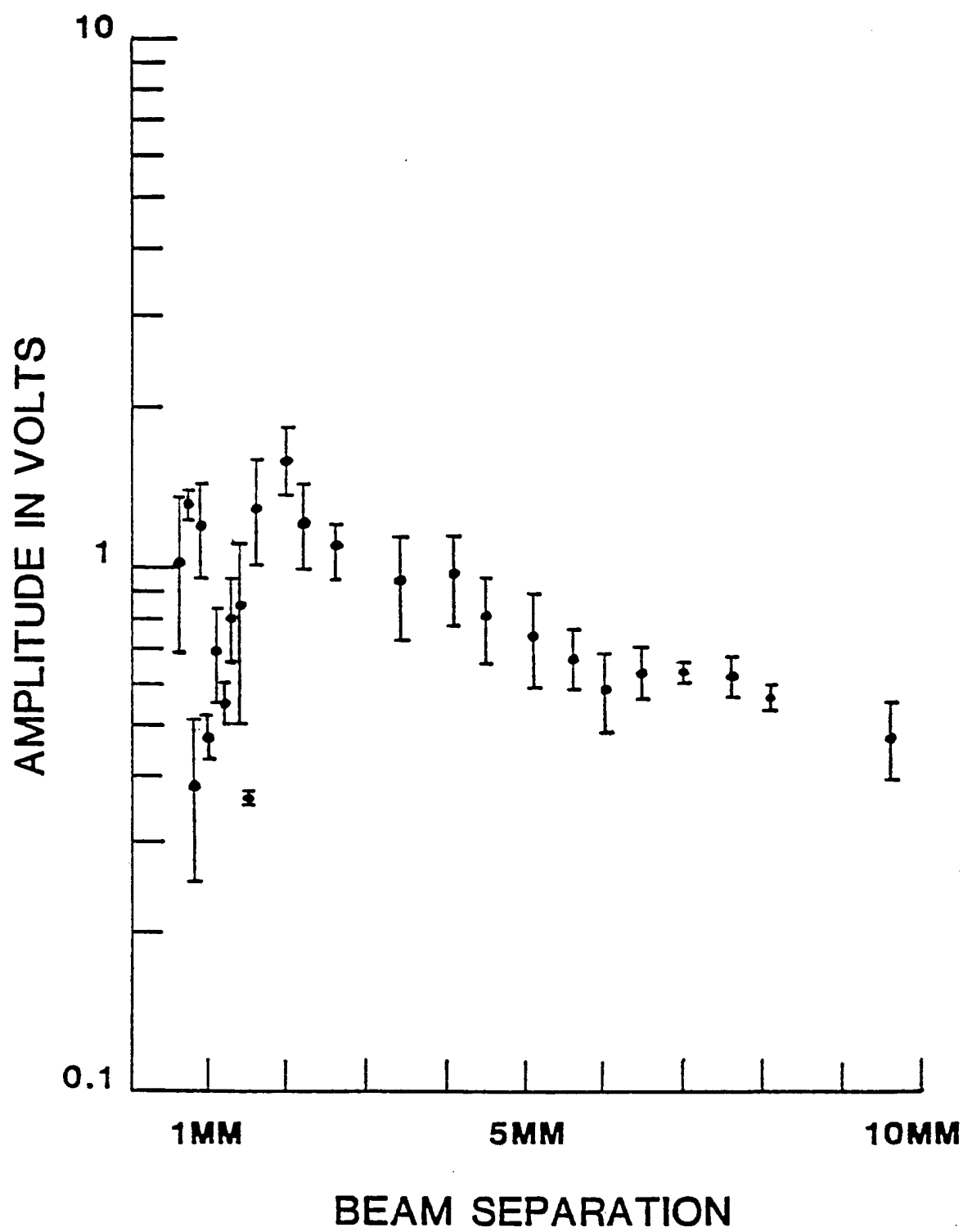


FIG 6

FIG 7

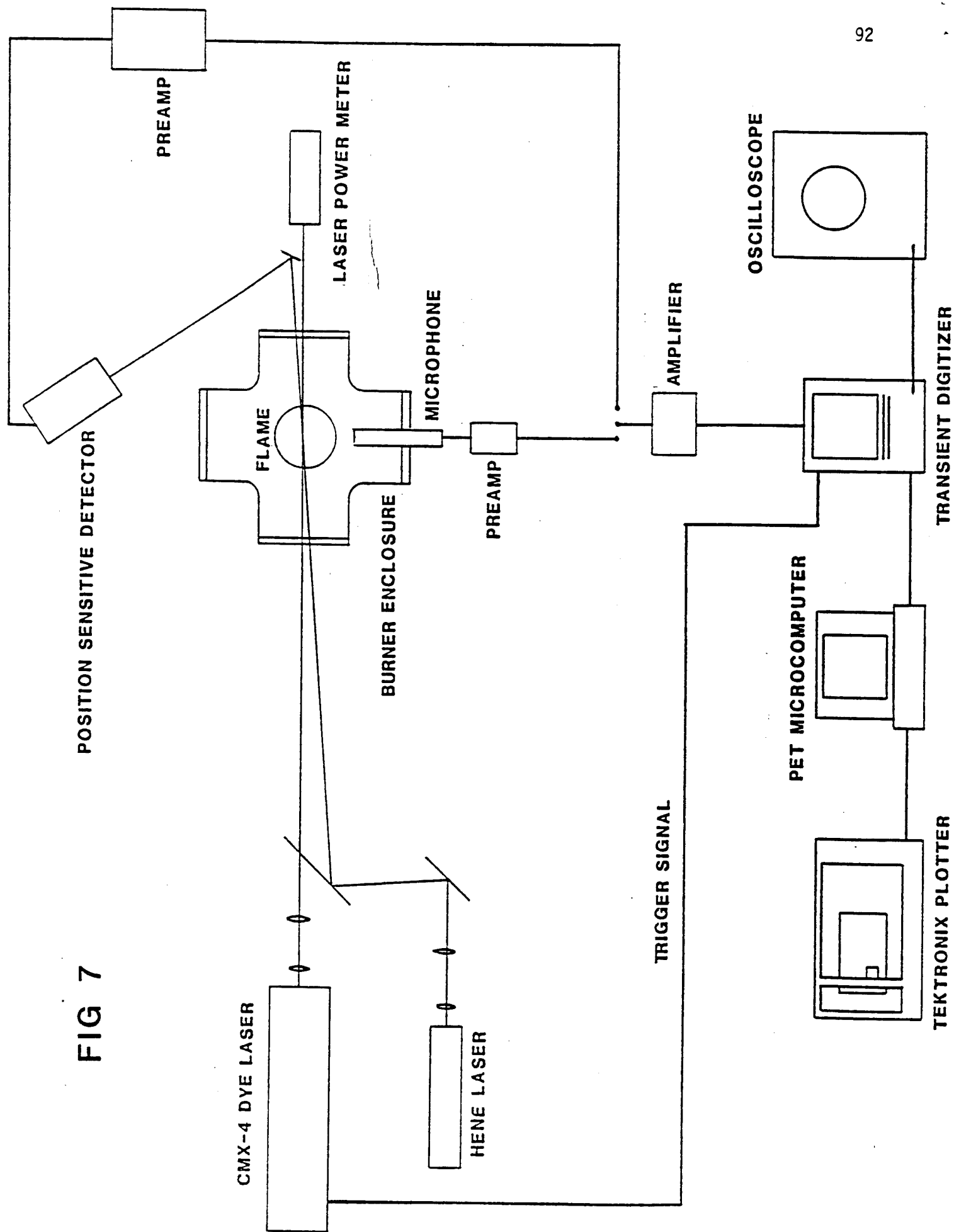


FIG 8

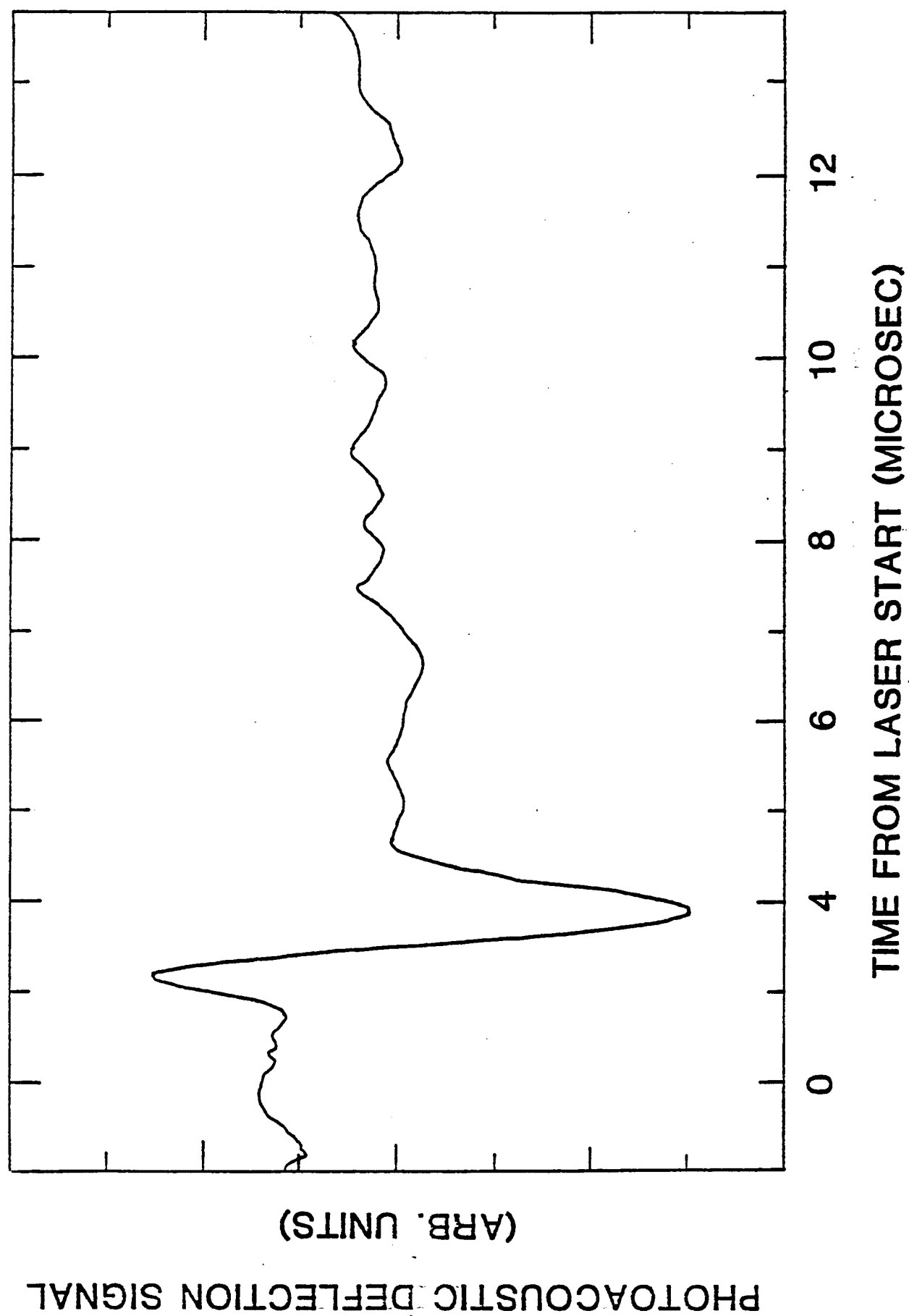


FIG 9

